Calcium isotopes in high-temperature terrestrial processes

Michael Antonelli, Justin Simon

Calcium isotopes in high-temperature terrestrial processes

Authors: Michael A. Antonelli[a,1,*], Justin I. Simon[b]

Affiliations: [a]Institut de Physique du Globe de Paris, University de Paris, 1 rue Jussieu, 75005 Paris, France. [b]Center for Isotope Cosmochemistry and Geochronology, Astromaterials Research & Exploration Science, NASA Johnson Space Center, Houston, USA. [1]Corresponding author. E-mail address: mantonelli@berkeley.edu (M.A. Antonelli). [*]Current address: Department of Earth Sciences, Institute of Geochemistry and Petrology, ETH Zurich, Clausiusstrasse 25, CH-8092, Zurich, Switzerland.

Keywords: Ca isotopes; igneous petrology; metamorphic petrology; volcanology; hydrothermal systems

Abstract: This chapter explores the growing body of stable and radiogenic Ca isotope measurements in high temperature terrestrial materials and covers the emerging applications for Ca isotope variability in igneous and metamorphic rocks and minerals. Calcium isotope fractionation at high temperature has been found to lead to larger effects than initially theorized, sometimes even exceeding those found in low temperature near-surface environments, yet many of the underlying fractionation mechanisms still remain poorly understood. Igneous whole-rocks span a δ^{44}Ca range of ~2‰ (-0.9 to +0.9‰, relative to bulk-silicate Earth) and their constituent minerals have a range of ~2.5‰ (-1.2 to +1.3‰). Metamorphic whole rocks span a larger δ^{44}Ca range of ~6‰ (-2.5 to +3.3‰), while metamorphic mineral separates span ~8‰ (-2.2 to +5.8‰). Observed Ca isotope variations can stem from a variety of sources including: (i) isolation of isotopically-distinct mineral components, such as during melting or crystallization, (ii) mixing of isotopically-distinct reservoirs into magmatic sources, such as during mantle metasomatism or

assimilation of distinct crustal components, and (iii) isotopic rate differences (kinetic effects) during melting, crystallization, transport, and metamorphism, which are often governed by Ca diffusion. The emerging picture is that Ca isotopes are sensitive to a large number of high-temperature processes and can be used to understand the evolution of crust and mantle reservoirs, along with mechanisms leading to the formation of igneous, metamorphic, and hydrothermal rocks and minerals through geologic time.

Table of Contents

1. Introduction

Over the last two decades it has become increasingly clear that Ca isotopes can be used to trace a wide variety of high-temperature solid Earth processes. Ca isotopes have been used to gain insight into diverse topics relevant to high-temperature geochemistry, including crustal recycling and contamination, rates and mechanisms of metamorphic and igneous processes (such as mantle metasomatism, metamorphic mineral paragenesis, and igneous crystal growth), and Ca transport in otherwise inaccessible regions of the solid Earth. The increasing body of work that has investigated Ca isotope fractionation has also yielded fundamental information on the behavior of redox-insensitive cations in high-temperature systems. In this fashion, understanding Ca isotope fractionation serves as a baseline for understanding the behavior of more complex, redox-sensitive, isotopic systems that undergo changes in oxidation-state (*e.g.* Fe, Cr, S, Ce), but which must also succumb to similar fractionation effects during chemical reaction and diffusive transport.

There are six stable isotopes of calcium with a total relative mass range of ~20%: ^{40}Ca (96.94%), ^{42}Ca (0.65%), ^{43}Ca (0.14%), ^{44}Ca (2.09%), ^{46}Ca (~40 ppm), and ^{48}Ca (0.19%). Due to the higher abundances of ^{40}Ca and ^{44}Ca, stable Ca isotope variations are commonly reported as δ^{44}Ca:

$$\delta^{44}Ca = \frac{\left({}^{44}Ca/{}_{40}Ca\right)_{sample}}{\left({}^{44}Ca/{}_{40}Ca\right)_{standard}} - 1 \quad \text{(Eq. 1)}$$

This formalism results in positive δ^{44}Ca values when a sample is enriched in ^{44}Ca relative to a known standard, and negative values when a sample is depleted in ^{44}Ca. It is important to note, however, that the most abundant isotope, ^{40}Ca, can also be produced by the radioactive decay of

^{40}K (half-life of ~1.25 Ga). Stable Ca isotope variations (δ^{44}Ca) must therefore be corrected for the potential radiogenic ingrowth of ^{40}Ca in analyzed samples. This is commonly accomplished by either measuring ^{44}Ca/^{42}Ca and then converting to ^{44}Ca/^{40}Ca by multiplying by 2.05 (Fantle and Tipper, 2014), which is the canonical mass-law for kinetic Ca isotope fractionation (the equilibrium mass law is ~2.10), or by measuring ^{44}Ca/^{40}Ca directly and then correcting for radiogenic ^{40}Ca ingrowth using additional (unspiked) measurements. Reporting Ca isotope data as $\delta^{44/42}$Ca instead of δ^{44}Ca would serve to separate stable from radiogenic isotope variations, but double-spike techniques used to correct for instrumental mass fractionation (IMF) during thermal ionization mass spectrometry (TIMS) often include ^{42}Ca and ^{48}Ca (or ^{43}Ca) spikes. Although ^{43}Ca-^{46}Ca double spikes would be the most useful to explore variations in ^{40}Ca, ^{42}Ca, ^{44}Ca, and ^{48}Ca simultaneously, the rarity of these isotopes greatly increases the cost of analysis, rendering this combination much less common.

The application of δ^{44}Ca measurements to high-temperature systems began to flourish starting with the observation that large δ^{44}Ca fractionations (up to ~10‰) were possible during chemical diffusion in silicate liquids (Richter et al., 2003, 1999). For the next decade, research focused mainly on exploring the various mechanisms responsible for diffusive Ca isotope fractionations in silicate liquids, which were shown to depend on: (i) the magnitude of Ca concentration gradients, (ii) the direction and magnitude of chemical gradients for other species, relative to those of Ca, (iii) the strength of imposed temperature gradients, and (iv) the degree of melt polymerization (F. Huang et al., 2010; Richter et al., 2009, 2003, 1999; Watkins et al., 2017, 2014, 2011, 2009).

The first δ^{44}Ca measurements in natural igneous rocks served as a baseline for ecological studies [where food-chain δ^{44}Ca variations were found to depend on trophic levels (Skulan et al., 1997)],

99 and were not further explored until the late 2000's (Amini et al., 2009; Jochum et al., 2006;
100 Simon and DePaolo, 2010; Wombacher et al., 2009). In the last ten years, however, there have
101 been an increasing number of Ca isotope studies in natural high-temperature rocks and minerals,
102 partially motivated by the initial observation that coexisting orthopyroxene and clinopyroxene in
103 mantle xenoliths have significant δ^{44}Ca variations (up to ~1 ‰) and that δ^{44}Ca variations in
104 Hawaiian basalts could be related to subduction of carbonates with low δ^{44}Ca (Huang et al.,
105 2011; S. Huang et al., 2010). Subsequent studies have mainly focused on understanding δ^{44}Ca
106 variations in mantle whole-rock samples (and rock standards) but have also explored δ^{44}Ca
107 variations in whole-rocks and mineral separates from mafic, silicic, metamorphic, and
108 hydrothermal samples. These studies highlight the potential for Ca isotopes to be used as proxies
109 for mantle metasomatism, carbonate recycling, crustal contamination, Ca diffusion
110 rates/mechanisms in the continental crust, partial melting, equilibration temperature,
111 metamorphic mineral paragenesis, K-loss during anatexis and high-temperature metamorphism,
112 mineral precipitation rates in hydrothermal systems, and crystal growth rates in magmatic
113 systems. Here, we present an overview of available Ca isotope data in high-temperature samples
114 and explore the potential strengths and limitations of their use as constraints for natural high-
115 temperature processes.

116 **1.1. Ca isotope nomenclature**

117 Similar to many other stable isotope systems, Ca isotope values are generally reported relative to
118 a known standard in lowercase delta-notation (δ^{44}Ca, Eq. 1) and followed by a per mil symbol
119 (‰), which indicates that the value has been multiplied by 1,000. Although it is redundant (and
120 technically incorrect) to include both a per mil symbol after reported values and a factor of 1,000
121 in the definition of δ^{44}Ca, many authors and peer-reviewers still push for both, which

unfortunately renders isotope nomenclature more complex than it needs to be, especially for students and scientists outside of our community. IUPAC has suggested to either (i) remove the factor of 1,000 from the definition (as we have done in Equation 1) if using a per mil symbol after reported values, or (ii) to omit the per mil symbol after values, if including a factor of 1,000 in the definition of $\delta^{44}Ca$ (Coplen, 2011). Other than common delta-notation, formalisms typically used in the isotope community include (i) epsilon (ε) notation, which reports deviations from the standard in parts per ten-thousand (commonly used for radiogenic ^{40}Ca variations), and (ii) mu (μ) notation, which reports values as parts per million (often used for particularly small variations).

In this review, we have chosen to include either per mil symbols (‰, for delta-notation) or indicate parts-per-million (ppm, for μ-notation) after reported values, in order to omit the factors of 1,000 and 1,000,000 from our definitions. For epsilon notation, we could potentially omit the factor of 10,000 from our definition of ε_{Ca} by reporting values with a per myriad (‱) or parts-per-ten-thousand (pptt) symbol, but to our knowledge, neither have been previously used. We therefore include the multiplicative factor in our definition of ε_{Ca} (in Section 7) and do not use any symbols after reporting ε-values. When comparing two related samples, isotopic differences are generally reported using capital delta notation (*e.g.* $\Delta^{44}Ca_{a\text{-}b}$, = $\delta^{44}Ca_a - \delta^{44}Ca_b$, for samples a and b), which can also be used to report deviations from an expected value [*e.g.* $\Delta^{48}Ca' = \mu^{48}Ca_{measured} - \mu^{48}Ca_{equilibrium}$]. All these notations, however, are further introduced and discussed in the most pertinent sections of this review.

2. Observations of mass-dependent Ca isotope variations in igneous and metamorphic rocks

144 Since the first measurements of stable Ca isotope distributions in volcanic rocks, there have been
145 over 60 studies measuring $\delta^{44}Ca$ in natural high-temperature samples. One of the common goals
146 for many of these studies is the definition of $\delta^{44}Ca$ for the bulk silicate Earth (BSE). Although
147 analytical uncertainties and potential sample-biases initially hindered the precise definition of
148 BSE $\delta^{44}Ca$, a growing number of studies based on mantle rocks and meteorites are converging
149 towards a relatively well-constrained $\delta^{44}Ca$ value of +0.95‰ relative to carbonate standard
150 SRM915a, which is approximately the same as initially estimated from early studies. The use of
151 BSE as a reference value for Ca isotope measurements [which comes from the first exploration
152 of stable Ca isotope variations in terrestrial/biological materials (Skulan et al., 1997)], however,
153 predates the use of SRM915a. Nevertheless, the analyzed igneous rocks and minerals in this
154 early study gave the same values (within uncertainty, ~3-4 times larger than today) as the most
155 up-to-date high-precision estimates *e.g.* (Kang et al., 2019). In order to best illustrate potential
156 differences and complementarity between Earth reservoirs, therefore, $\delta^{44}Ca$ data from UC-
157 Berkeley have since been reported relative to an estimated BSE value (which has corresponded
158 to +0.95‰ relative to SRM915a for the last decade, but was slightly higher in earlier studies).
159 More than four different reference materials, however, are commonly used to define $\delta^{44}Ca$
160 (including SRM915a, SRM915b, BSE, and modern seawater) and they must be converted to a
161 common scale in order to allow for comparison between studies. Although SRM915a is no
162 longer commercially available and seawater $\delta^{44}Ca$ is, on average, controlled by the extent of
163 carbonate precipitation in the oceans (which may have changed over geologic time) and can also
164 vary based on collection depth and location (Chakrabarti et al., 2018), it is hard to argue for the
165 use of one standard over another. In Table 1, we present inter-conversion factors for commonly
166 used Ca isotope standards. To use these factors and report Ca isotope data to different reference

materials, it is sufficient to add the listed value from Table 1 to the measured delta value [*e.g.* $\delta^{44}Ca_{BSE} = \delta^{44}Ca_{915a} + (-0.95)$]. Note that for very large values, it is more accurate to recast the delta values into isotopic ratios and then re-calculate new delta values using the $^{44}Ca/^{40}Ca$ of desired reference materials, but terrestrial Ca isotope fractionations are not generally large enough to warrant this additional step. To convert $\delta^{44/42}Ca$ values to $\delta^{44}Ca$, one can simply multiply by 2.05 (or divide $\delta^{44}Ca$ by 2.05 to arrive at $\delta^{44/42}Ca$). In this study, we chose to report $\delta^{44}Ca$ data relative to BSE in order to more clearly represent potential complementarity between various solid-Earth reservoirs and have converted published data using the values listed in Table 1.

Table 1. Values for inter-conversion of $\delta^{44}Ca$ results using common standard materials.

Measured Ca reference

Desired Ca reference	BSE	SRM915A	SRM915B	Seawater	BSE 44/42	SRM915A 44/42	SRM915B 44/42	Seawater 44/42
BSE		-0.95	-0.23	0.90	x2.05			
SRM915A	0.95		0.72	1.85		x2.05		
SRM915B	0.23	-0.72		1.13			x2.05	
Seawater	-0.90	-1.85	-1.13					x2.05
BSE 44/42	÷2.05							
SRM915A 44/42		÷2.05						
SRM915B 44/42			÷2.05					
Seawater 44/42				÷2.05				

The conversion factors listed above are additive (columns/rows 1-4), while conversions between 42/44 and 44/40 are multiplicative.

The delta values can be related to isotopic ratios by the accepted 42/44= 0.31221 and 40/44 BSE = 47.162.

Additional complications result from small radiogenic ^{40}Ca enrichments in standard SRM915a [and in modern carbonates/seawater (Antonelli et al., 2018)] relative to basaltic igneous rocks (Antonelli et al., 2019a; He et al., 2017; Mills et al., 2018; Simon et al., 2009; Zhao et al., 2017), meteorites (Simon et al., 2009; Yokoyama et al., 2017), and modern hydrothermal fluids

(Antonelli et al., 2019a). These radiogenic enrichments can lead to small discrepancies in reported $\delta^{44}Ca$ values depending on the analytical technique. TIMS measurements are sensitive to radiogenic ^{40}Ca variations, whereas multi-collector inductively-coupled plasma mass spectrometry (MC-ICP-MS) analyses (which do not commonly measure ^{40}Ca due to isobaric interferences from ^{40}Ar) are not affected by radiogenic Ca variations. The difficulty of achieving a stable signal for ^{42}Ca using MC-ICP-MS (which requires high-resolution slits in order to separate ^{42}Ca from a large isobaric interference at mass 42), however, stifles the potential dominance of this method over TIMS. The radiogenic ^{40}Ca enrichments in SRM915a and seawater ($^{40}Ca/^{44}Ca$ of 47.162 *vs.* ~47.156 for BSE, at a normalizing $^{42}Ca/^{44}Ca$ ratio of 0.31221) are just barely resolvable with current analytical precisions (~0.1‰) and still await further confirmation before renormalization of all TIMS data (Antonelli et al., 2019a, 2018; Mills et al., 2018). The apparent radiogenic enrichments in SRM915a and seawater, however, would require a negative shift of ~0.1‰ for TIMS $\delta^{44}Ca$ data from samples with lesser amounts of radiogenic ^{40}Ca than the normalizing standards.

2.1. Bulk silicate Earth composition: measurements and models

Early literature data for oceanic basalts suggest relatively large (>0.5‰) variations in $\delta^{44}Ca$ (DePaolo, 2004; Skulan et al., 1997; Zhu and Macdougall, 1998). Likewise, measurement of igneous minerals, especially the principal Ca-bearing minerals found in mantle peridotites (clinopyroxene, orthopyroxene), exhibit significant isotopic heterogeneity (*e.g.* S. Huang et al., 2010). Based on these observations and the upper mantle mineral assemblage, Huang et al. (2010) estimated that the upper mantle and thus Bulk Silicate Earth (BSE) $\delta^{44}Ca$ is 1.05±0.04‰, relative to Ca isotope standard SRM915a. This mantle estimate is slightly higher (by ~0.1) than the average $\delta^{44}Ca$ of the basalt samples measured by Huang et al. (2010), and the average value

reported by Amini et al. (2009) and more recent studies. Using the published data on igneous rocks from Skulan et al. (1997) and DePaolo (2004) the approach of Huang et al. (2010) would indicate that $\delta^{44}Ca$ of BSE should be close to ~1.00±0.15‰, relative to standard SRM915a. The work of Simon and DePaolo (2010) found that the average $\delta^{44}Ca$ value representing a large diversity of differentiated materials and ordinary chondritic meteorites (n=12), including samples from the Moon and Mars, is indistinguishable from terrestrial basalts and mantle peridotites (n=5) and used this value to define both the Ca isotopic composition of BSE as well as the terrestrial planets and planetary bodies that formed within the inner Solar System (their value for BSE is 0.97±0.07‰ after re-normalization to the $\delta^{44}Ca$ of SRM915a). More recently, Kang et al. (2017) reported that a subset of 28 peridotites xenoliths, those which experienced little or no melting and metasomatism (n=14) exhibited limited $\delta^{44}Ca$ variation from 0.90 to 0.99‰ yielding an average value of 0.94±0.05‰ (relative to SRM915a). Following a similar approach to Simon and DePaolo (2010), Kang et al. (2017) used their new data and a compilation of available Ca isotope literature data to define the Ca isotopic composition of BSE ($\delta^{44}Ca$ = +0.95 ± 0.05‰, relative to SRM915a). Given the precision and accuracy of Ca isotope measurements in the published literature it appears that both approaches, those that compute BSE values from mineral compositions and those who define BSE from representative whole rock samples (from Earth and other planetary bodies) yield similar values. As more studies of carefully selected mantle-derived samples are analyzed, the Ca isotopic composition of the upper mantle will be more fully characterized.

2.2. Observations from igneous rocks

Since the first observation of systematic $\delta^{44}Ca$ variations in Hawaiian basalts (Huang et al., 2011) there have been well over 40 studies focused on exploring Ca isotope variations in

igneous rocks. A dominant proportion of these studies have measured $\delta^{44}Ca$ in different types of mantle (ultramafic) whole rocks, while a more limited number of studies explore $\delta^{44}Ca$ in intermediate to felsic igneous rocks. Ultramafic samples are generally defined by their modal mineralogies, falling into two main categories, pyroxenites (orthopyroxenites, websterites, and clinopyroxenites, with or without olivine) and peridotites (lherzolites, harzburgites, wehrlites, and dunites). In a general sense, starting from fertile mantle and extracting basaltic melt, one is left with residual lherzolite (> 5% Cpx), and with greater melt extraction, residual harzburgite (< 5% Cpx). Reactions between percolating pyroxene-undersaturated basaltic melts and lherzolites can then lead to formation of replacive dunites (> 90% olivine), while simultaneous melt-percolation and crystallization can lead to formation of websterites (< 5% olivine), clinopyroxenites (> 90% Cpx), orthopyroxenites (> 90% Opx), and wehrlites (<5% Opx), depending on the saturation state of the percolating melt with respect to the various minerals (*e.g.* Chen et al., 2019b). Further classification of major ultramafic rock types depends on the presence of either spinel or garnet as an aluminous phase, with garnet-bearing rocks indicative of higher pressures. Mafic to felsic rocks are also distinguished through modal mineralogy but are more commonly classified by their SiO_2 and associated alkali element concentrations (Na_2O and K_2O).

In Fig. 1, we have compiled >650 igneous whole rock $\delta^{44}Ca$ measurements and have grouped them by major rock type, increasing from ultramafic (bottom) to felsic compositions (top). Within each major group the categories are further broken down by whether they are intrusive or extrusive, and then by their dominant mineralogies (if originally described).

Although there is scatter in the data, the first observation is that there is a rough inverse relationship between SiO_2 content and $\delta^{44}Ca$, where increasingly felsic rocks have decreasing

250 $\delta^{44}Ca$ (Fig. 1). This observation is in agreement with recent work regarding the average $\delta^{44}Ca_{BSE}$
251 compositions of mid-ocean ridge basalts (MORB, ~ -0.1‰) (Chen et al., 2019a) and estimated
252 average continental crust (~ -0.2‰) (Wang et al., 2019) relative to non-metasomatized peridotite
253 samples, *e.g.* (Chen et al., 2019b). By combining data from different labs, figure 1 compensates
254 for potential inter-lab biases (*e.g.* ~0.2‰ variation in published values for BHVO and BCR-2
255 standards), but additional work is necessary in order to reach agreement between labs and move
256 forward with higher precision Ca isotope measurements as a community.

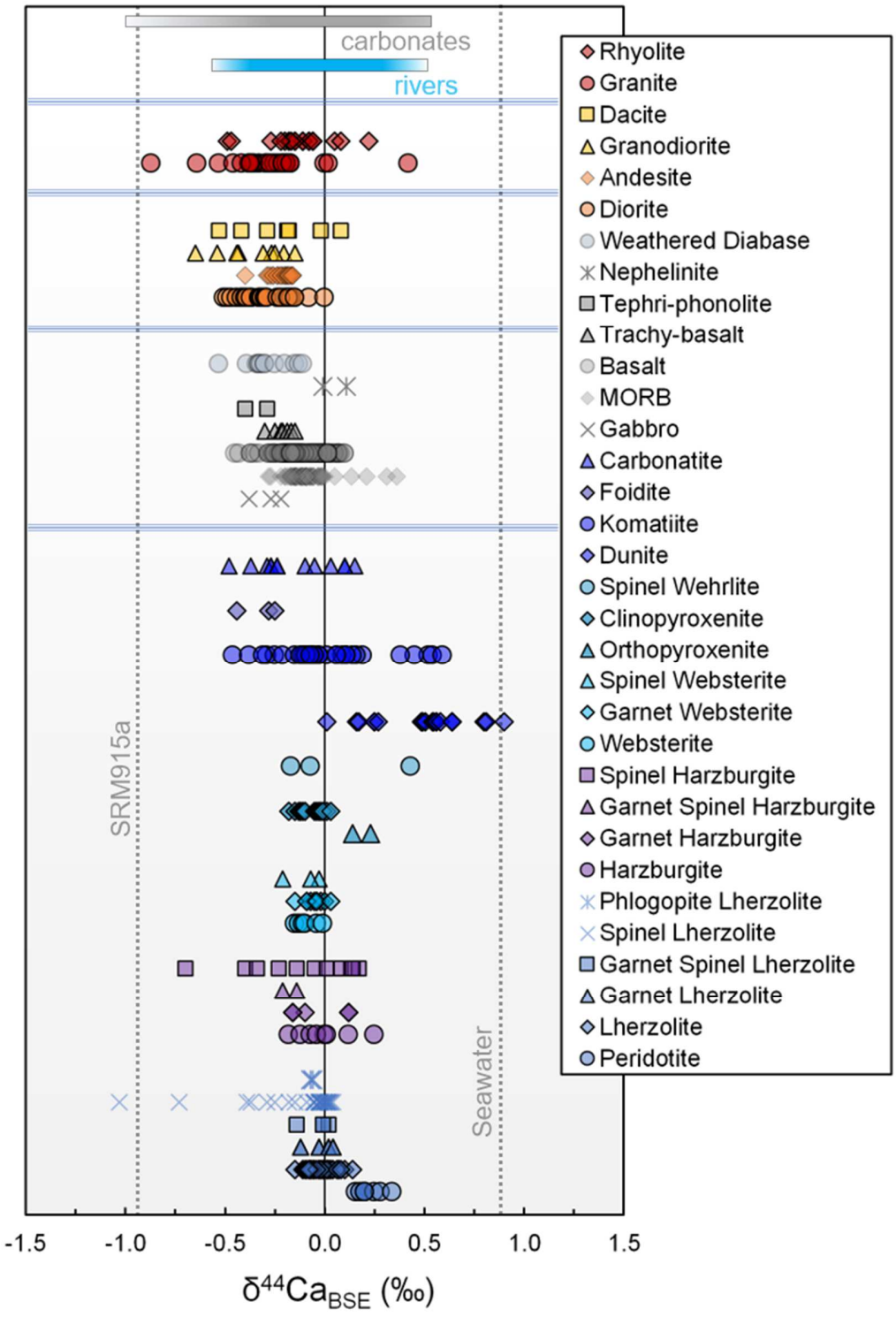

257

258 **Fig. 1.** Compilation of $\delta^{44}Ca_{BSE}$ in igneous whole rocks (n = 655) grouped by major sample type. All TIMS data

259 have been corrected for radiogenic ^{40}Ca variations, when applicable, and all data are normalized to Bulk-silicate

Earth (BSE). $\delta^{44}Ca_{BSE}$ is +0.95‰ relative to standard SRM915a, +0.23‰ relative to SRM915b, and -0.90‰ relative to seawater (see Table 1). Igneous rock data are from (Amini et al., 2009; Amsellem et al., 2019, 2017; Antonelli et al., 2019b; Banerjee and Chakrabarti, 2019, 2018; Chen et al., 2019a, 2019b, 2018; Colla et al., 2013; Dai et al., 2020; DePaolo, 2004; Feng et al., 2018, 2016; He et al., 2017; Holmden and Bélanger, 2010; Huang et al., 2011; S. Huang et al., 2010; Ionov et al., 2019; Jacobson et al., 2015; Jochum et al., 2006; John et al., 2012; Kang et al., 2017; Lehn and Jacobson, 2015; Liu et al., 2017b, 2017a; Lu et al., 2019; Magna et al., 2015; Peterson, 2013; Richter et al., 2003; Ryu et al., 2011; Schiller et al., 2012; Simon et al., 2017; Simon and DePaolo, 2010; Skulan et al., 1997; Valdes et al., 2014; Wang et al., 2017b, 2019; Wombacher et al., 2009; Zhang et al., 2018; Zhao et al., 2017; Zhu et al., 2020, 2018; Zhu and Macdougall, 1998). The approximate ranges for 95% of carbonates and rivers come from (Fantle and Tipper, 2014).

Ultramafic samples have the highest $\delta^{44}Ca$ variability of all analyzed igneous rocks, though this may be partially due to the greater number of analyzed samples (Fig. 1). The ultramafic samples with the highest $\delta^{44}Ca$ are dunites, which is likely due to their high percentages of olivine (which is predicted to favor heavy isotopes at equilibrium, discussed in Section 3). The lightest ultramafic $\delta^{44}Ca$ values are found in komatiites, foidites, carbonatites, and spinel lherzolites and harzburgites. The spinel-facies sub-types of lherzolites, harzburgites, and websterites tend to have more negative $\delta^{44}Ca$ than their garnet-facies counterparts. This observation may be explained by the presence of garnet as an isotopically heavy residual phase (discussed in Section 3) but requires further exploration. Heavy $\delta^{44}Ca$ compositions in certain komatiites have been argued to reflect mantle-heterogeneities inherited from Ca-perovskite crystallization during the early magma ocean period of Earth history, while light $\delta^{44}Ca$ may reflect incorporation of serpentinized oceanic crust into komatiite sources (Amsellem et al., 2019); only one study, however, suggests that subducting slabs preferentially lose fluids enriched in heavy Ca isotopes (John et al., 2012). This conclusion was reached primarily because blueschists adjacent to eclogites in Western Tianshan had slightly heavier Ca isotopic compositions (suggesting the

285 influx of fluids enriched in heavy Ca isotopes), but it is uncertain whether this reflects (i) a
286 primary signature of the fluids lost from the eclogites or (ii) that these fluids were subsequently
287 enriched due to precipitation of isotopically light carbonates (John et al., 2012). A recent study
288 suggests that prograde dehydration metamorphism in subduction zones does not lead to
289 significant Ca isotope fractionation (Lu et al., 2019), which lends weight to the second
290 interpretation. Much more work is needed, however, to understand Ca isotope fractionations in
291 subduction zones. The lowest δ^{44}Ca values in ultramafic rocks are suggested to stem from kinetic
292 effects during metasomatism (Zhao et al., 2017), which is further discussed in Section 6.2. Rarer
293 igneous rocks, such as carbonatites, are rich in carbonate minerals, which may potentially
294 explain their isotopically light compositions, while low δ^{44}Ca in alkali-rich groups (foidites)
295 require further exploration. Trachy-basalts, like foidites, also have slightly lower δ^{44}Ca compared
296 to basalts, which may suggest a role for increasing alkali element concentrations.

297 Although there is significantly less data for intermediate to felsic rocks, the largest variations are
298 observed in granites (Fig. 1). Granites, along with intermediate igneous rocks, have δ^{44}Ca almost
299 exclusively more negative than bulk silicate Earth, but their higher variability (> 1‰) compared
300 to other groups suggests that they are (i) affected by a greater number of (potentially kinetic)
301 processes and/or (ii) that they incorporate a greater variety of isotopically-distinct source
302 materials. A larger number of studies on intermediate to felsic rocks is required to understand
303 this variability.

304 Given the greater number of data for ultramafic samples, partial melting and fractional
305 crystallization processes (as shown in Fig. 2) are better understood in mantle rocks. The general
306 observation is that partial melting of fertile mantle generally leaves behind isotopically heavier
307 mafic minerals (*e.g.* Opx, Ol) and higher Mg#, defined 10^2[Mg/(Mg+Fe)], as isotopically lighter

phases (*e.g.* Cpx) are preferentially lost to the melt. Fractional crystallization of mafic phases leads to decreasing Mg# in the residual liquid, but the isotopic effects are negligible as a probable consequence of their low Ca concentrations (*e.g.* olivine, orthopyroxene). Zhang et al. (2018) modeled melting of spinel facies peridotite (Fig. 2c,d) at pressures between 1 and 2 GPa using the pMELTS program. They found that isotopic variations generated from both primitive and depleted mantle compositions lead to less than ~0.1‰ variation in the melt fractions. Residual material, on the other hand, can show larger variations, as isotopically-heavy orthopyroxene becomes the dominant Ca bearing phase, with potential δ^{44}Ca increases of the order ~0.2 to 0.3‰ [at a corresponding melt-fraction (F) of 0.3] when using a fractional melting model (Zhang et al., 2018). Mantle melting at higher-pressure, amenable to the stabilization of garnet as a residual phase, leads to larger effects (up to ~0.4‰) for the generated melts (Kang et al., 2019), while generation of adakitic melts may succumb to similar processes (Wang et al., 2019). Fractionation factors still remain poorly constrained, however, and the large δ^{44}Ca variations observed in metasomatized mantle samples, along with their relationships to a wide variety of percolating mantle fluids [potentially causing kinetic isotope fractionations (*e.g.* Zhao et al., 2017)], still merit further study.

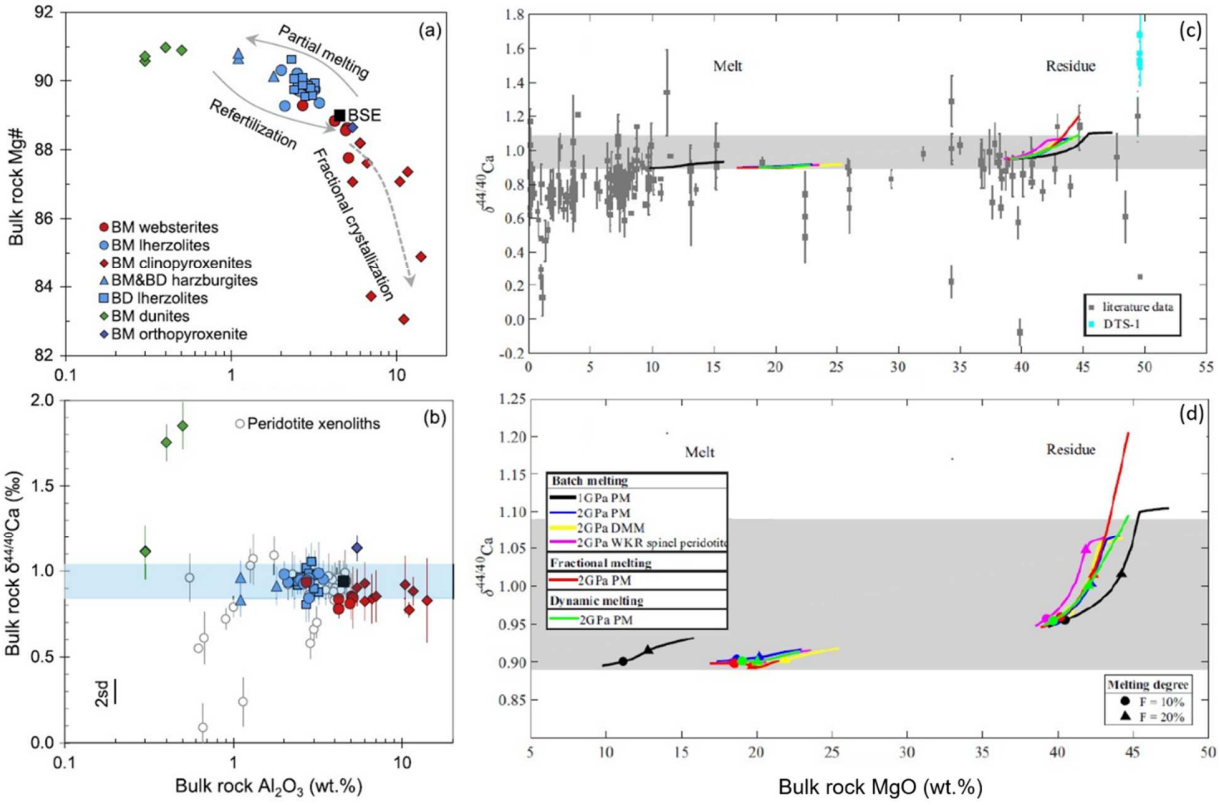

Fig. 2a-d. (a,b) Bulk chemical and $\delta^{44}Ca$ data for ultramafic rocks from the Balmuccia (BM) and Baldissero (BD) orogenic massifs, showing predicted effects of partial melting, crystallization, and mantle refertilization after (Chen et al., 2019b). Fertile lherzolite and harzburgite xenoliths are shown for comparison (hollow symbols) (Kang et al., 2017; Zhao et al., 2017). $\delta^{44}Ca$ data are relative to SRM915a, and the blue horizontal band represents the estimated $\delta^{44}Ca$ of the Earth's upper mantle (0.94 ± 0.10‰). The long-term external precision from Chen et al. (2019b), ~0.14‰ (2sd) is shown at the bottom left. **(c)** Plot of whole rock $\delta^{44}Ca$ versus MgO for igneous rocks with model predictions for partial melting of the mantle at 1 and 2 GPa. Horizontal grey band represents BSE composition estimates with uncertainty, after Zhang et al. (2018). **(d)** same as (c) but with expanded y-axis and without data, to more clearly show predicted effects of partial melting [model details can be found in Zhang et al. (2018)]. Data come from studies published before 2019 (Amini et al., 2009; Colla et al., 2013; DePaolo, 2004; Fantle and Tipper, 2014; Feng et al., 2016; He et al., 2017; Holmden and Bélanger, 2010; S. Huang et al., 2010; Huang et al., 2011; Jacobson et al., 2015; Jochum et al., 2006; John et al., 2012; Kang et al., 2017, 2016; Lehn and Jacobson, 2015; Liu et al., 2017a, 2017b; Magna et al., 2015; Richter et al., 2003; Ryu et al., 2011; Schiller et al., 2012; Simon et al.,

2017; Simon and DePaolo, 2010; Skulan et al., 1997; Valdes et al., 2014; Wombacher et al., 2009; Zhang et al., 2018; Zhao et al., 2017; Zhu et al., 2018; Zhu and Macdougall, 1998).

2.3. Observations from metamorphic rocks

Metamorphic rocks are typically classified based on mineral compositions and modal mineralogy, which are related to the starting materials (either igneous or sedimentary protoliths) and to the temperature and pressure conditions of metamorphism. In a general sense, high temperature metamorphism (*e.g.* granulite-facies, T > ~750°C, ~0.4-1.4 GPa) favors the transformation of hydrous minerals to anhydrous assemblages, whereas high-pressure metamorphism [*e.g.* blueschist-facies (< ~500°C, ~0.5-1.5 GPa) and eclogite-facies (> ~400°C, > ~1.5 GPa)] favors the formation of high-density mineral assemblages, though dehydration can also occur. Metamorphic facies intermediate to the others (*e.g.* greenschist and amphibolite-facies) are also defined by their mineral assemblages and result from the variable influences of metasomatic fluids, temperature (300-700°C), and pressure (~0.2 to ~1 GPa).

Although Ca isotopes in metamorphic rocks are not as extensively studied as in igneous rocks, the limited number of studies (Antonelli et al., 2019c; John et al., 2012; Kang et al., 2019; Liu et al., 2017b; Lu et al., 2019; Peterson, 2013; Valdes et al., 2019; Wang et al., 2019; Wombacher et al., 2009) suggest that large fractionation effects occur during metamorphism. Whole rocks span a $\delta^{44}Ca$ range of ~6‰ (-2.5 to +3.3‰ relative to BSE, Fig. 3). The $\delta^{44}Ca$ variations appear to get larger with increasing metamorphic grade, with the largest fractionations in rocks that have experienced upper amphibolite-facies (Peterson, 2013) and granulite-facies metamorphism (Antonelli et al., 2019c; Valdes et al., 2019).

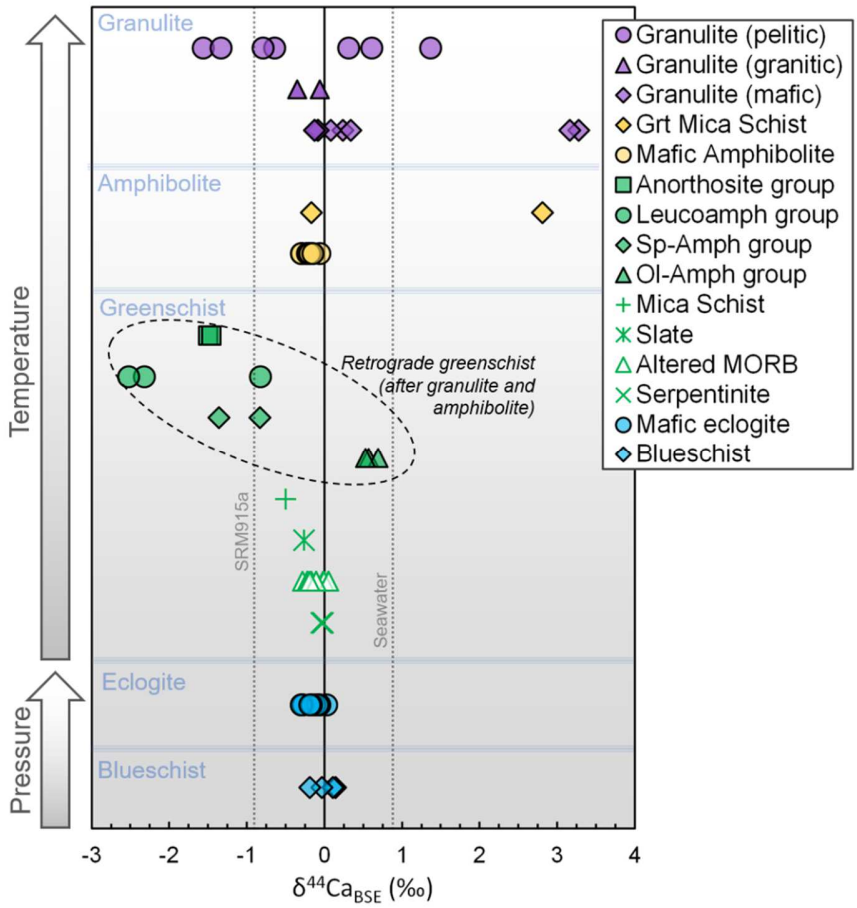

Fig. 3. $\delta^{44}Ca_{BSE}$ for metamorphic whole rocks grouped by principal metamorphic facies and protolith-type (n = 72). Data are from (Antonelli et al., 2019c; John et al., 2012; Kang et al., 2019; Liu et al., 2017b; Lu et al., 2019; Peterson, 2013; Valdes et al., 2019; Wombacher et al., 2009), retrograde greenschist data are from Valdes et al. (2018).

Given that inter-mineral fractionations in a closed system should not result in whole rock $\delta^{44}Ca$ variations, the observed variability indicates that Ca isotope fractionations occur in open systems and require either addition or removal of isotopically distinct components during metamorphism. The larger fractionations at higher temperatures suggest that the $\delta^{44}Ca$ effects are likely to be the result of kinetic fractionation effects during Ca diffusion, melting, and/or dehydration reactions, which are further discussed in Section 6.

3. Equilibrium Ca isotope fractionation

As with many isotopic systems, the initial goal for inter-mineral Ca isotope analyses was to use them as constraints on equilibration temperature ('Ca isotope geothermometry'). Using Ca isotopes as a proxy for temperature in natural samples, however, requires (i) knowledge of equilibrium isotope fractionations between minerals at different temperatures, and (ii) that isotopic equilibrium was reached between minerals. The following sections evaluate the potential use of Ca isotopes for geothermometry and describe current constraints on equilibrium $\Delta^{44}Ca_{a\text{-}b}$, defined:

$$\Delta^{44}Ca_{a-b} = \delta^{44}Ca_a - \delta^{44}Ca_b \quad \text{(Eq. 2)}$$

Where subscripts 'a' and 'b' denote two minerals 'a' and 'b'.

3.1. General background principles

Isotope partitioning between mineral phases at equilibrium depends mainly on vibrational frequency differences for heavy *vs.* light isotopes in mineral structures. Tighter bonds (with higher vibrational frequencies) are preferentially stabilized by substitution of a heavy isotope. This effect is a consequence of quantum mechanical factors, where tighter bonds have greater relative decreases in zero-point energy (ZPE, the quantized vibrational energy of a chemical bond at absolute zero), which stems from the Heisenberg uncertainty principle, and in higher-level vibrational frequencies upon substitution of a heavier isotope (Bigeleisen and Mayer, 1947; Chacko et al., 2001; Urey, 1947; Young et al., 2002). Consequently, heavier isotopes are preferentially placed into mineral sites with stronger bonds in order to decrease the Gibbs free energy (ΔG) of a system. For Ca isotopes, this leads to higher $\delta^{44}Ca$ in minerals with stronger/shorter Ca-O bonds. When bond lengths are unknown, a general rule is that sites with

higher coordination numbers have longer bonds and therefore have less preference for heavy isotopes than sites with lower coordination numbers [*e.g.* Ca-perovskite has 12-fold coordination and is thus predicted to have low reduced-partition function ratios (RPFR, discussed in Section 3.2) and concentrate lighter Ca isotopes (Amsellem et al., 2019)]. At a given Ca-O bond-length, however, it is important to note that sites with higher coordination numbers have stronger overall bonding environments and therefore favor heavier isotopes.

Equilibrium constants for isotopic substitution reactions (denoted α, as opposed to K for chemical equilibrium constants) are highly dependent on temperature due to the increasing population of higher quantum vibrational states with increasing temperatures (Chacko et al., 2001). As a result, isotopic differences between mineral pairs are often used as constraints on equilibration temperature ('isotope geothermometry'), where higher temperatures are expected to decrease inter-mineral fractionations.

Equilibrium fractionation factors (α), which must be constrained in order to derive temperatures from isotopic data, can be obtained through various methods. These generally include (i) direct measurements from experiments, such as mineral-mineral or mineral-carbonate exchange experiments (Chacko et al., 2001; Shahar et al., 2008), and/or determination of vibrational frequencies through (ii) advanced spectroscopic techniques [*e.g.* nuclear resonant inelastic x-ray scattering (Dauphas et al., 2012)], or (iii) ab-initio simulations (*e.g.* Widanagamage et al., 2014). The determination of vibrational frequencies using spectroscopic methods is not currently possible for Ca because there are no Mossbauer-sensitive isotopes. Common experimental approaches (*e.g.* Kueter et al., 2019; Shahar et al., 2008) would technically allow for the determination of equilibrium Ca isotope fractionation factors, but at present we are not aware of any reliable experimental constraints. Thus, our current understanding of equilibrium Ca isotope

fractionation between various minerals relies principally on ab-initio estimates, which are discussed in the following section.

3.2. Ab-initio Predictions

The first Ca isotope measurements in mineral separates revealed large $\delta^{44}Ca$ differences (~1 ‰) in orthopyroxene and clinopyroxene from mantle xenoliths (S. Huang et al., 2010), suggesting that Ca isotope fractionations could potentially be used for geothermometry. The first ab-initio estimates for equilibrium Ca isotope fractionation between minerals, published four years later, confirmed the initial observation that orthopyroxene concentrates heavy isotopes of Ca over clinopyroxene at equilibrium. Ab-initio techniques generally rely on advanced computational methods that serve to predict vibrational frequency shifts for different isotopes in a given molecule or crystal lattice, which can then be used to predict equilibrium isotope effects. Predicted equilibrium $\Delta^{44}Ca_{opx\text{-}cpx}$ values were found to range from ~0.3‰ at 1200°C to ~1‰ at 500°C (Feng et al., 2014), which has also been corroborated by more recent ab-initio studies (Antonelli et al., 2019c; Wang et al., 2017b). Equilibrium predictions for minerals other than pyroxenes have only recently been investigated (Antonelli et al., 2019c; Huang et al., 2019; Song et al., 2019), but find that olivine is expected to have the heaviest Ca isotope compositions, followed by garnet, orthopyroxene, clinopyroxene, apatite, anorthite, labradorite (An_{50}), and oldhamite (CaS).

In Fig. 4 we show the reduced partition function ratios (formalized as 1000lnβ, which quantifies the preference for heavy *vs.* light isotopes within a single phase) for various minerals *vs.* temperature (Huang et al., 2019; Song et al., 2019; Wang et al., 2017a). Fractionation factors (1000lnα), which represent the prediction for $\Delta^{44}Ca_{a\text{-}b}$ between two minerals, can be

approximated visually from these kinds of figures using $1000\ln\beta_a - 1000\ln\beta_b$, but should be calculated using $\alpha_{a\text{-}b} = \beta_a/\beta_b$ (note: $\Delta^{44}Ca_{a\text{-}b} \approx 1000\ln\alpha_{a\text{-}b} = 1000\ln\beta_a - 1000\ln\beta_b$).

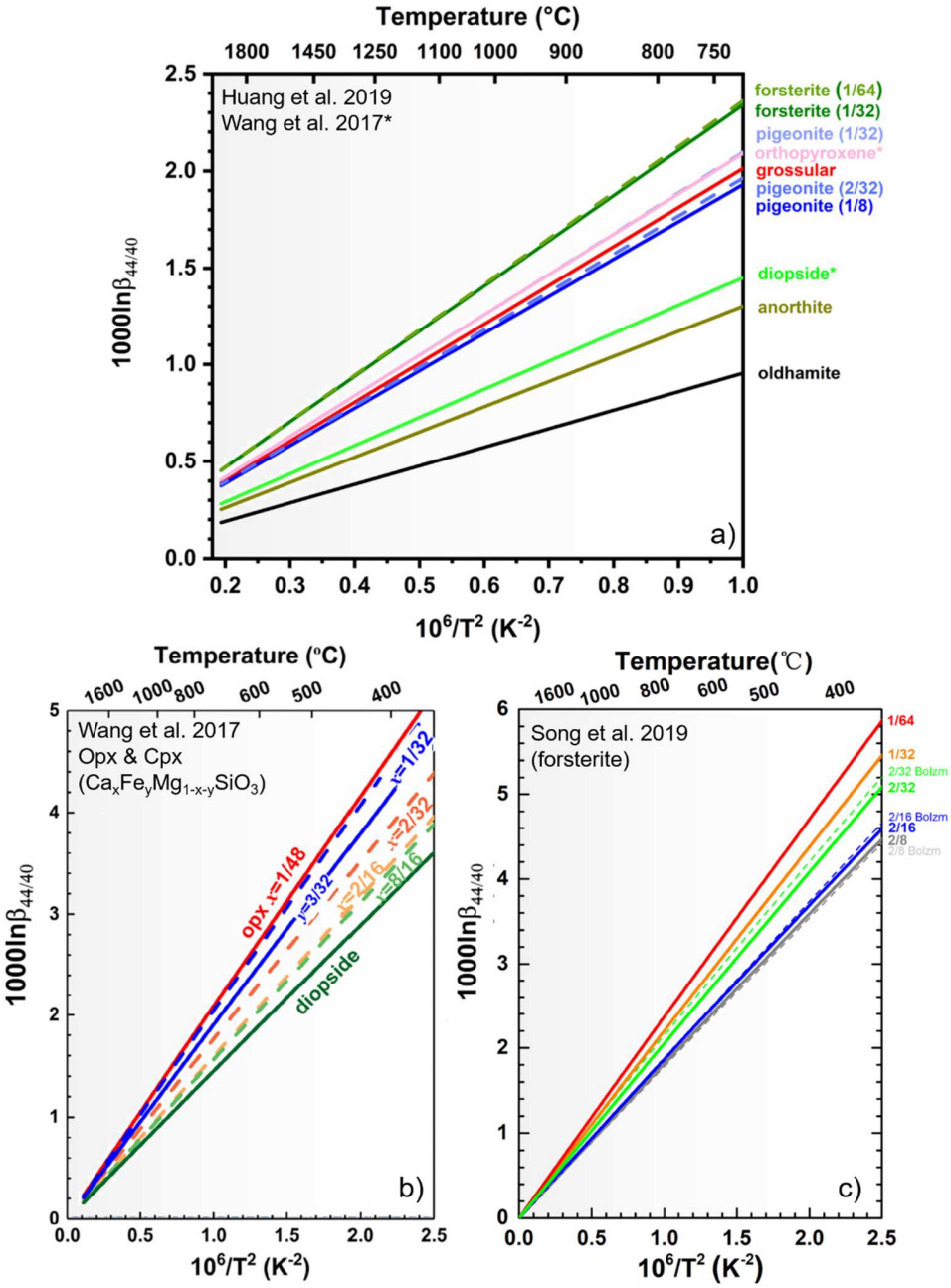

Fig. 4a-c. Equilibrium estimates for reduced partition function ratios (1000lnβ) *vs.* temperature in various minerals, based on DFT models using local-density approximation (LDA) functionals. **(a)** Modified from Huang et al. (2019), orthopyroxene and diopside estimates (*) are from Wang et al. (2017b). **(b)** Orthopyroxene with various solid-

443 solution compositions, modified from Wang et al. (2017b). **(c)** Forsterite with various Ca/(Ca+Mg), modified from
444 Song et al. (2019).

445 The major-cation compositions of solid-solution minerals are also expected to affect Ca isotope
446 fractionation (Antonelli et al., 2019c; Feng et al., 2014; Huang et al., 2019; Song et al., 2019;
447 Wang et al., 2017b). For example, the preference for heavy Ca isotopes in orthopyroxene
448 decreases with increasing Ca/Mg (Antonelli et al., 2019c; Feng et al., 2014; Huang et al., 2019;
449 Wang et al., 2017b), as depicted in Figs. 4b and 5. This effect is a general manifestation of
450 increasing distortions in the mineral lattice with increasing Ca abundances (due to the relatively
451 large size of Ca compared to Mg). The distortions lead to increased average Ca-O bond lengths
452 and thus decrease the overall affinity for heavy Ca isotopes (Antonelli et al., 2019c; Feng et al.,
453 2014; Wang et al., 2017b). This dilution effect, however, becomes negligible below a
454 Ca/(Ca+Mg) of ~1/32 in orthopyroxene, and larger $\Delta^{44}Ca_{Opx\text{-}Cpx}$ are not predicted at lower values
455 (Antonelli et al., 2019c; Wang et al., 2017b). Small dilution effects are also predicted for
456 increasing orthopyroxene Fe/Mg, where increasing Ca-O bond lengths with increasing Fe lead to
457 slightly decreased affinities for heavy Ca isotopes (Wang et al., 2017b). For pigeonite (a high-
458 temperature pyroxene phase that commonly separates into orthopyroxene and clinopyroxene
459 lamellae upon slow-cooling), RPFRs are generally found to be intermediate to clinopyroxene and
460 orthopyroxene and also decrease with increasing pigeonite Ca/Mg (Huang et al., 2019), shown in
461 Fig. 4a.

462 Ca dilution effects (also known as "Ca concentration effects", depending on the author) have
463 also been investigated in olivine, but have contradictory results. One study suggests that
464 decreasing Ca/Mg in olivine leads to increased RPFRs, Fig. 4c [~0.3‰ difference between 1/16
465 and 1/64 at 1000 K (Song et al., 2019)], while another study suggests that Ca concentrations in

466 olivine have no significant effect on its affinity for heavy Ca isotopes [(only ~0.1‰ difference
467 between 1/16 and 1/64 at 1000 K (Antonelli et al., 2019c)]. Future experiments are required to
468 confirm the veracity of dilution effects in olivine.

469 Garnet solid-solution end-members have decreasing RPFRs when the major cation is changed
470 from Mg to Fe, Mn, and Ca [1000lnβ of pyrope > almandine ≈ spessartine > grossular (Antonelli
471 et al., 2019c)], as shown in Fig. 5. Ca dilution effects in garnet have only been investigated in
472 pyrope, but no significant difference was found between estimates with Ca/(Ca+Mg) of 1/12 and
473 1/24 (Antonelli et al., 2019c).

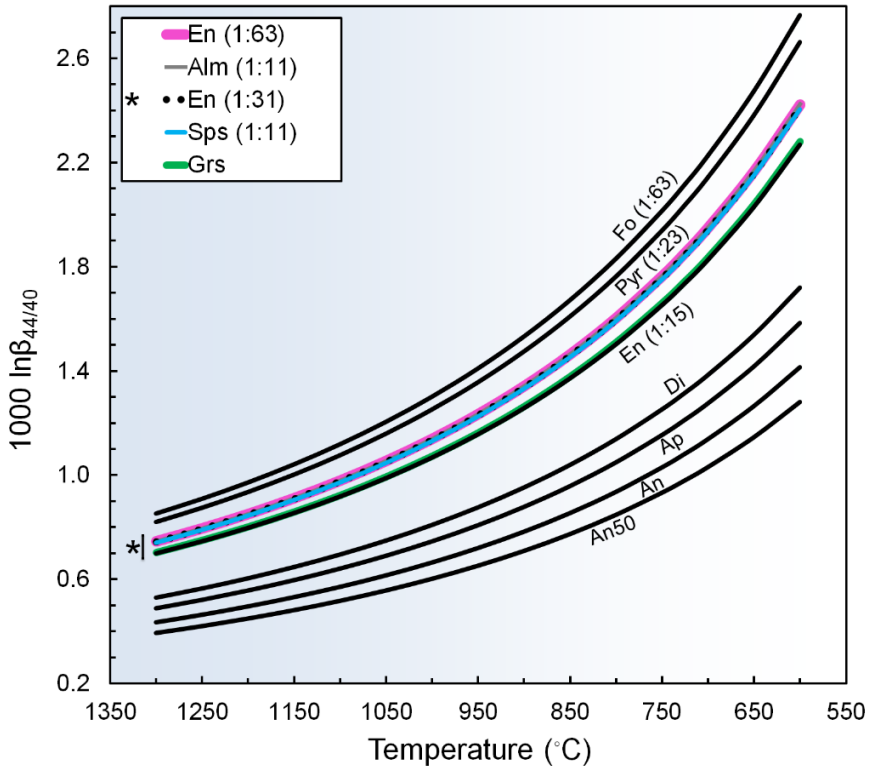

474

475 **Fig. 5.** Equilibrium estimates for reduced partition function ratios (1000lnβ) for $^{44}Ca/^{40}Ca$ *vs.* temperature for
476 minerals based on DFT models using generalized gradient approximation (GGA) PBE functionals (Perdew, Burke,
477 Ernzerhof), modified from (Antonelli et al., 2019c). As opposed to Fig. 4, the lines are curved due to use of a linear
478 temperature scale.

479 The disagreement between predicted differences for Ca dilution effects in various minerals may
480 be explained by methodological differences between the various studies, which use different
481 approximations for defining the relevant electronic structures. Greater dilution effects due to
482 decreasing Ca concentrations in both orthopyroxene and olivine are generally predicted when
483 using local-density approximation (LDA) functionals (Feng et al., 2014; Huang et al., 2019;
484 Song et al., 2019; Wang et al., 2017b), while smaller effects are predicted when using
485 generalized gradient approximations (GGA) such as PBE (Perdew, Burke, Ernzerhof) functionals
486 (Antonelli et al., 2019c). LDA functionals are the simplest type of density functional, where the
487 exchange-correlation energy density is assumed to be that of a uniform electron gas at a single
488 point; GGA functionals (such as PBE) are formulas that use both the energy density and its
489 gradient at each point, which gives more accurate estimates of bond dissociation energies and
490 transition-state barriers (Rappoport et al., 2011). The slightly smaller 1000lnβ values and Ca
491 dilution effects in Antonelli et al. (2019c) may thus be due the use of GGA *vs.* LDA exchange-
492 correlation functionals. However, this becomes less important when calculating equilibrium
493 fractionation factors (α) because they depend only on the RPFR *differences* between phases.
494 Nevertheless, some of the differences between predicted equilibrium fractionation factors
495 (1000lnα) are greater than average analytical uncertainties for $\delta^{44}Ca$ (~0.1‰), even at high
496 temperatures, and are worthy of further investigation.

497 Despite the different approaches used in the DFT estimates and small discrepancies between
498 predicted 1000lnα for certain mineral pairs, first-order agreement is reached between the various
499 studies regarding the general effects of mineral Ca concentration and average Ca-O bond length
500 on predicted fractionation factors. In Figure 6, we show a summary of $^{44}Ca/^{40}Ca$ RPFRs from all
501 published ab-initio studies versus (i) Ca concentrations, defined as Ca/(Ca+Mg+Fe+Mn+Na), in

various minerals (Fig. 6a) and (ii) average Ca-O bond lengths (Fig. 6b). This figure demonstrates that minerals with less Ca (*e.g.* olivine, orthopyroxene, pyrope) generally have higher affinities for ^{44}Ca, while minerals with higher Ca concentrations (*e.g.* clinopyroxene & plagioclase) have lower affinities for ^{44}Ca. It also illustrates the dependence of 1000lnβ values on average Ca-O bond lengths and coordination numbers, where longer Ca-O bonds lead to lower affinities for ^{44}Ca and greater coordination numbers at a given bond-length lead to increased affinities for ^{44}Ca (Fig. 6b).

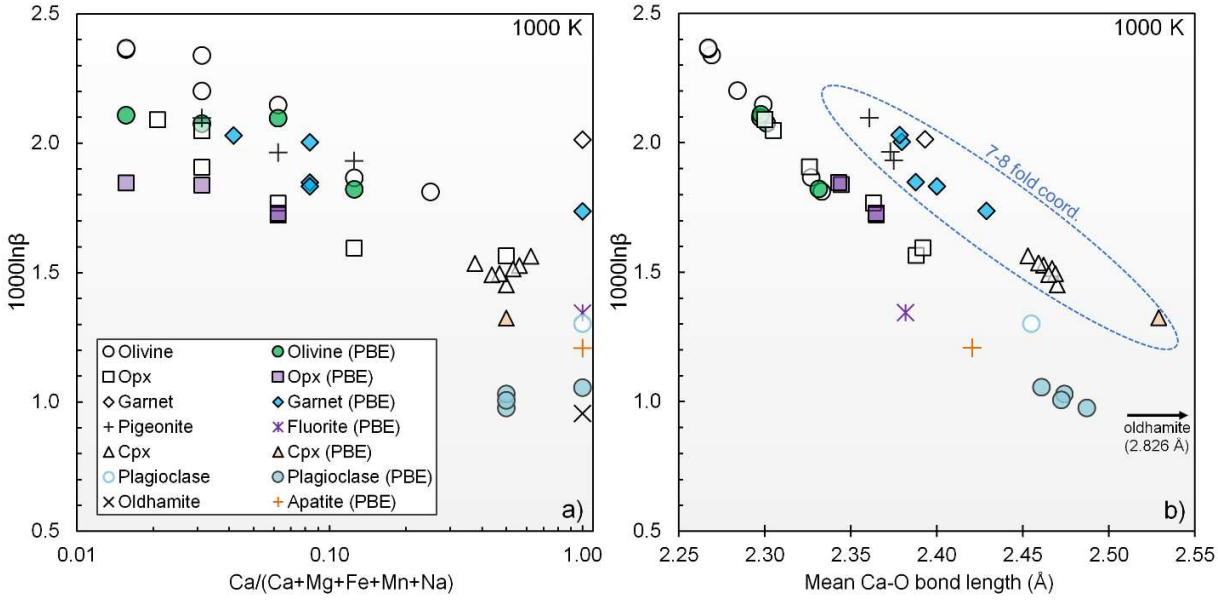

Fig. 6a,b. Summary of available equilibrium estimates for ^{44}Ca/^{40}Ca reduced partition function ratios (1000lnβ) *vs.* **(a)** Ca concentrations relative to other major cations, Ca/(Ca+Mg+Fe+Mn+Na), and **(b)** average Ca-O bond lengths in various minerals. PBE-based estimates (colored symbols) are generally lower than LDA-based estimates. Data are from (Antonelli et al., 2019c; Feng et al., 2014; Huang et al., 2019; Song et al., 2019; Wang et al., 2017b).

Despite the general agreement for inter-mineral fractionation factors between studies, absolute values for 1000lnβ in single minerals can be dramatically different based on the approach [*e.g.* ~2.5 (Song et al., 2019) *vs.* ~1.8 (Antonelli et al., 2019c) for forsterite with Ca/(Ca+Mg) of 1/64 at 800°C], so it is important to use RPFR values that were derived from the same method when

calculating equilibrium fractionation factors ($\alpha_{a\text{-}b} = \beta_a/\beta_b$) to arrive at internally-consistent predictions for inter-mineral Δ^{44}Ca. We also provide a compilation of RPFRs and fitting parameters for inter-mineral fractionations (Antonelli et al., 2019c; Feng et al., 2014; Huang et al., 2019; Song et al., 2019; Wang et al., 2017b), to serve as a reference for future studies (Table 2).

Table 2. Compilation of *ab-intio* predictions and fitting-factors for equilibrium RPFRs (1000lnβ).

Reference	Type	Mineral		Ca/Ca+Fe+Mg+Mn+Na	1000lnβ (1000 K)	Coord.	Bond-length (Å)	a	b	c
Huang et al., 2019	LDA	Anorthite	-	1.000	1.30	6.75	2.455	6.21E-05	-5.68E-03	1.307
		Forsterite 1/32	Ca/Mg 1/32	0.031	2.34	6	2.269	1.63E-04	-1.51E-02	2.355
		Forsterite 1/64	Ca/Mg 1/64	0.016	2.36	6	2.267	0.00E+00	0.00E+00	2.362
		Grossular	-	1.000	2.01	8	2.393	1.08E-04	-1.08E-02	2.025
		Oldhamite	-	1.000	0.96	6	2.826	4.89E-06	-1.71E-03	0.957
		Pigeonite 1/8	Ca/Mg 1/8	0.125	1.93	7	2.375	1.15E-04	-1.11E-02	1.942
		Pigeonite 1/16	Ca.Mg 1/16	0.063	1.96	7	2.373	0.00E+00	0.00E+00	1.964
		Pigeonite 1/32	Ca/Mg 1/32	0.031	2.10	7	2.361	0.00E+00	0.00E+00	2.097
Song et al., 2019	LDA	Forsterite 1/64	Ca/Mg 1/64	0.016	2.37	6	2.267	2.36E-04	-1.57E-02	2.383
		Forsterite 1/32	Ca/Mg 1/32	0.031	2.20	6	2.284	2.09E-04	-1.41E-02	2.216
		Forsterite 1/16	Ca/Mg 1/16	0.063	2.01	6	2.299	1.74E-04	-1.21E-02	2.021
		Forsterite 1/16a	Ca/Mg 1/16	0.063	2.15	6	2.299	3.27E-03	-5.64E-02	2.202
		Forsterite 1/8	Ca/Mg 1/8	0.125	1.88	6	2.327	1.28E-04	-9.83E-03	1.888
		Forsterite 1/8a	Ca/Mg 1/8	0.125	1.87	6	2.327	1.25E-03	-2.46E-02	1.890
		Forsterite 1/4	Ca/Mg 1/4	0.250	1.78	6	2.333	1.27E-04	-9.12E-03	1.789
		Forsterite 1/4a	Ca/Mg 1/4	0.250	1.81	6	2.333	8.88E-04	-1.95E-02	1.831
Feng et al., 2014	LDA	Opx 1/32	Ca/Mg 1/32	0.031	2.05	6	2.305	1.88E-04	-1.27E-02	2.061
		Opx 1/16	Ca/Mg 1/16	0.063	1.77	6	2.363	1.51E-04	-9.71E-03	1.778
		Opx 1/8	Ca/Mg 1/8	0.125	1.59	6	2.392	1.31E-04	-8.27E-03	1.603
		Opx 1/2	Ca/Mg 1/2	0.500	1.57	6	2.388	1.20E-04	-7.70E-03	1.573
		Cpx 1/2	Ca/Mg 1/2	0.500	1.45	8	2.47	1.18E-04	-6.89E-03	1.458
Wang et al., 2017b	LDA	Opx 1/32 Fe 3/32	Ca/Mg 1/32 Fe 3/32	0.031	1.91	6	2.326	1.59E-04	-1.11E-02	1.918
		Opx 1/48	Ca/Mg 1/48	0.021	2.09	6	2.3	1.94E-04	-1.32E-02	2.104
		Cpx 3/8	Ca/Mg 3/8	0.375	1.54	8	2.459	1.26E-04	-7.61E-03	1.543
		Cpx 7/16	Ca/Mg 7/16	0.438	1.49	8	2.465	1.22E-04	-7.28E-03	1.498
		Cpx 15/32	Ca/Mg 15/32	0.469	1.50	8	2.469	1.23E-04	-7.28E-03	1.503
		Cpx 17/32	Ca/Mg 17/32	0.531	1.51	8	2.467	1.27E-04	-7.59E-03	1.521
		Cpx 9/16	Ca/Mg 9/16	0.563	1.53	8	2.462	1.28E-04	-7.83E-03	1.535
		Cpx 5/8	Ca/Mg 5/8	0.625	1.56	8	2.453	1.26E-04	-8.01E-03	1.571
		Diopside	-	0.500	1.45	8	2.47	1.18E-04	-6.89E-03	1.458
Antonelli et al., 2019c	PBE	Diopside	-	0.500	1.32	8	2.529	-	-	-
		Opx 1/16	Ca/Mg = 1/16	0.063	1.72	6	2.3649	Note: 7th Ca-O bond at 2.66Å		
		Opx 1/16	Ca/Mg = 1/16, 2c	0.063	1.73	6	2.3649	Note: 7th Ca-O bond at 2.66Å		
		Opx 1/32	Ca/Mg = 1/32, 2c	0.031	1.84	6	2.3445	Note: 7th Ca-O bond at 2.67Å		
		Opx 1/64	Ca/Mg = 1/64, 2c	0.016	1.85	6	2.343	Note: 7th Ca-O bond at 2.68Å		
		Forsterite 1/8	Ca/Mg = 1/8, M2	0.125	1.82	6	2.3314	-	-	-
		Forsterite 1/16	Ca/Mg = 1/16, 2a	0.063	2.10	6	2.2975	-	-	-
		Forsterite 1/32	Ca/Mg=1/32, 2ac	0.031	2.08	6	2.3010	-	-	-
		Forsterite 1/64	Ca/Mg=1/64, 4a2c	0.016	2.11	6	2.2977	-	-	-
		Grossular	-	1.000	1.74	8	2.4288	-	-	-
		Pyrope 1/12	Ca/Mg = 1/12	0.083	2.00	8	2.3797	-	-	-
		Pyrope 1/24	Ca/Mg = 1/24 fcc	0.042	2.03	8	2.3784	-	-	-
		Almandine 1/12	Ca/Fe = 1/12 fm	0.083	1.85	8	2.3876	-	-	-
		Spessartine 1/12	Ca/Mn = 1/12 fm	0.083	1.83	8	2.3999	-	-	-
		Anorthite	-	1.000	1.06	6	2.4608	Note: 7th Ca-O bond at ~2.9-3.0Å		
		Labradorite	An50-Ab50 v1	0.500	0.98	6	2.4871	Note: 7th Ca-O bond at 2.97-3.00Å for all Ca sites		
		Labradorite	An50-Ab50 v2	0.500	1.03	6	2.4740	Note: 7th Ca-O bond at 2.84Å for half of Ca sites		
		Labradorite	An50-Ab50 v3	0.500	1.01	6	2.4723	Note: 7th Ca-O bond at 2.92Å for half of Ca sites		
		Apatite	Fluorapatite	1.000	1.21	6	2.4205	Note: Ca1, *7-10th Ca-O neighbors at		

						2.84Å; Ca2, 5O+1F, and *7th Ca-O bond at 2.80Å		
Lime (CaO)	-	1.000	1.51	6	2.4158	-	-	-
Fluorite (CaF_2)	-	1.000	1.34	8	2.3818	-	-	-

Fitting equation: $1000 \ln\beta = ax^3 + bx^2 + cx$, where $x = 10^6/T^2$, The various labradorite structures (v1-v3) used in Antonelli et al. (2019c) are from (Kaercher et al., 2014).

4. Observed inter-mineral Ca isotope fractionations

Unlike whole-rock analyses, $\delta^{44}Ca$ in mineral separates from individual rock samples have only been reported in a limited number of studies (Antonelli et al., 2019c, 2019b; Bessey, 2018; Chen et al., 2019b, 2018; Dai et al., 2020; S. Huang et al., 2010; Kang et al., 2019, 2016; Ryu et al., 2011; Simon and DePaolo, 2010; Skulan et al., 1997; Wang et al., 2019; Zhao et al., 2017) several of which analyze only one or two samples. In the following sections, we compare inter-mineral $\Delta^{44}Ca$ measurements from igneous and metamorphic rocks to those predicted by ab-initio estimates at relevant temperatures.

We generally find that predictions and measurements are often in disagreement. This observation suggests that inter-mineral Ca isotope fractionations are not likely to be reliable for geothermometry. Although experimental confirmation of the *ab-initio* predictions is still required, a recently published triple-isotope approach, which quantifies deviations from an equilibrium mass-law in $^{48}Ca/^{44}Ca$ *vs.* $^{42}Ca/^{44}Ca$ space (discussed in Section 5.2), suggests that they are approximately correct (Antonelli et al., 2019c). Thus, observed deviations from expected Ca isotope equilibrium are likely to be the result of kinetic effects in natural samples.

4.1. Igneous minerals

Mineral separates from ultramafic to felsic igneous rocks have a measured $\delta^{44}Ca_{BSE}$ range of -1.2 to +1.3‰ (Fig. 7a) (Antonelli et al., 2019b; Chen et al., 2019b, 2018; S. Huang et al., 2010; Kang et al., 2016; Ryu et al., 2011; Simon and DePaolo, 2010; Skulan et al., 1997; Zhao et al., 2017) . Orthopyroxene separates from ultramafic rocks tend to have the highest $\delta^{44}Ca$, but are highly variable and span the entire range observed in igneous minerals (~2.5‰). In mafic to

547 felsic rocks there is a smaller $\delta^{44}Ca$ range (~1‰), where plagioclase has the lowest $\delta^{44}Ca$ (but is
548 found to vary by ~0.5‰) and where ferromagnesian minerals (*e.g.* clinopyroxene, hornblende,
549 chlorite, epidote, biotite) are generally heavier than non-ferromagnesian minerals (*e.g.*
550 plagioclase, K-feldspar, melilite, apatite, titanite). Biotite has the most positive measured $\delta^{44}Ca$
551 out of these minerals, but has only been analyzed in one sample (Ryu et al., 2011).

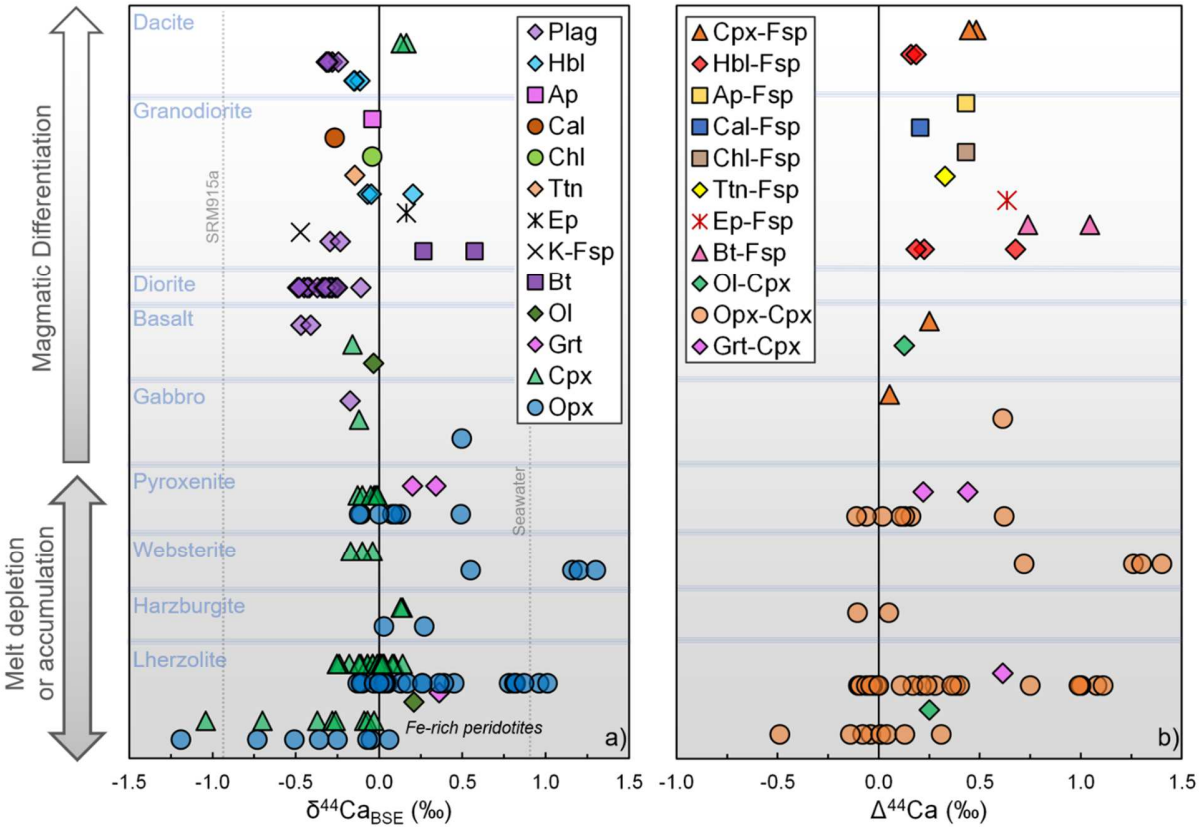

552

553 **Fig. 7a,b.** Ca isotope compositions in igneous minerals (n = 146), grouped by rock type. **(a)** measured $\delta^{44}Ca$ in
554 mineral separates, and **(b)** measured inter-mineral $\Delta^{44}Ca$ (n = 69). Data are from (Antonelli et al., 2019b; Chen et al.,
555 2019b, 2018; Dai et al., 2020; S. Huang et al., 2010; Kang et al., 2016; Ryu et al., 2011; Simon and DePaolo, 2010;
556 Skulan et al., 1997; Wang et al., 2019; Zhao et al., 2017), Fe-rich peridotite data, which are especially low in $\delta^{44}Ca$,
557 are from Zhao et al. (2017).

558 Inter-mineral $\Delta^{44}Ca$ values in igneous rocks span a range of ~2‰ (Fig. 7b). In mafic to felsic
559 rocks, all ferromagnesian minerals have higher $\delta^{44}Ca$ than coexisting feldspars ($\Delta^{44}Ca_{min\text{-}fsp}$ up to

560 +1‰). The largest inter-mineral fractionations ($\Delta^{44}Ca_{opx\text{-}cpx}$ up to +1.5‰) are observed between
561 orthopyroxene and clinopyroxene. In most rocks $\Delta^{44}Ca_{opx\text{-}cpx}$ is positive, but a growing number of
562 samples have negative $\Delta^{44}Ca_{opx\text{-}cpx}$ (down to -0.5‰). To date, all analyzed clinopyroxene-
563 orthopyroxene pairs in websterites are out of Ca isotopic equilibrium, with orthopyroxene too
564 heavy, and all analyzed harzburgites, Fe-rich lherzolites, and a significant number of
565 pyroxenites, are out of isotopic equilibrium with orthopyroxene too light (Fig. 8a). Due to the
566 much higher concentration of Ca in clinopyroxene, however, imperfect mineral separations may
567 push orthopyroxene $\delta^{44}Ca$ towards the 1:1 line, and great care should be taken in future studies,
568 including verification of Ca concentrations in mineral separates [which can then be used for
569 eventual unmixing calculations *e.g.* (Antonelli et al., 2019c)].

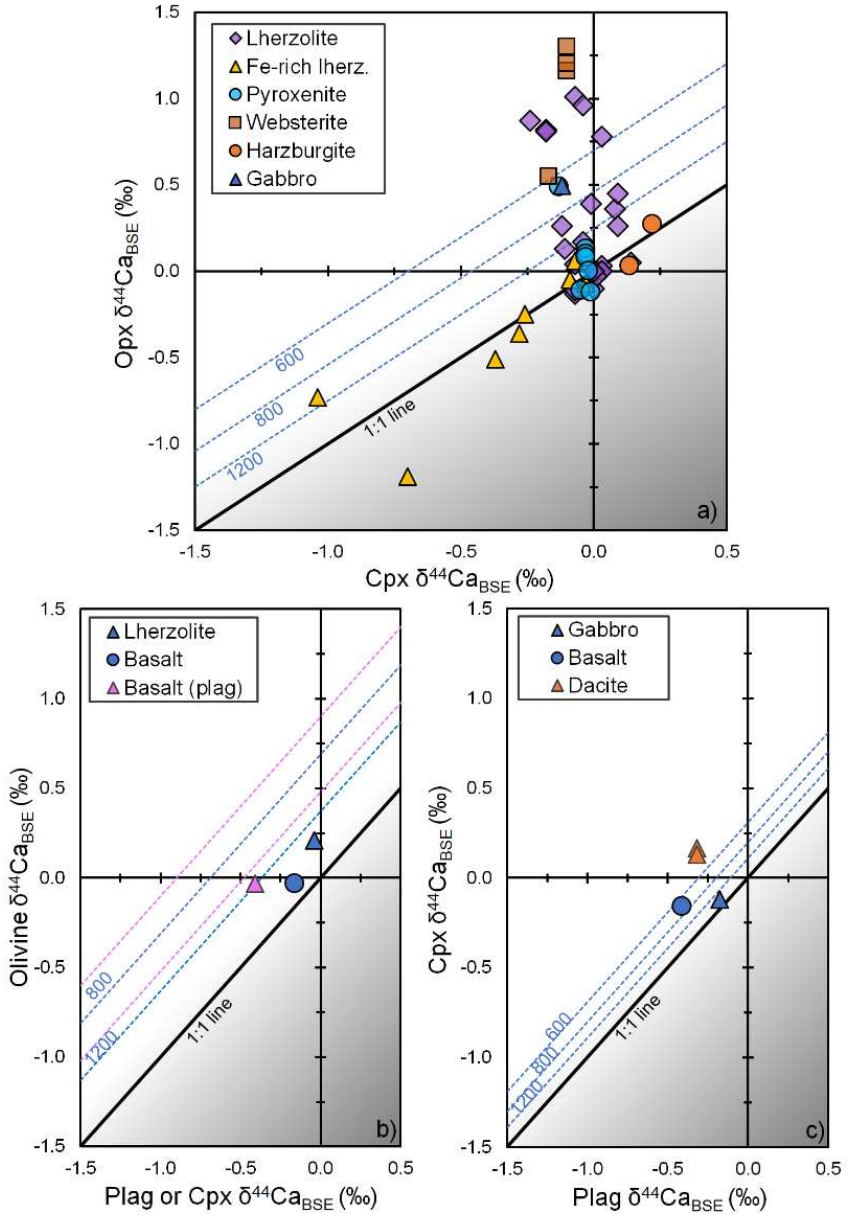

570

571 **Fig. 8a-c.** Mineral-specific $\delta^{44}Ca$ measurements in igneous rocks (grouped by rock-type) compared with equilibrium
572 ab-inito predictions at various temperatures (in degrees Celsius). **(a)** $\delta^{44}Ca_{opx}$ *vs.* $\delta^{44}Ca_{cpx}$ (n = 47), **(b)** $\delta^{44}Ca_{ol}$ *vs.*
573 $\delta^{44}Ca_{cpx}$ (or $\delta^{44}Ca_{plag}$) (n = 3), and **(c)** $\delta^{44}Ca_{cpx}$ *vs.* $\delta^{44}Ca_{plag}$ (n = 4). Data are from (Antonelli et al., 2019b; Chen et
574 al., 2019b, 2018; Dai et al., 2020; S. Huang et al., 2010; Kang et al., 2016; Ryu et al., 2011; Simon and DePaolo,
575 2010; Skulan et al., 1997; Zhao et al., 2017). Ab-initio estimates for diopside, anorthite, orthopyroxene, and olivine
576 are based on DFT estimates using PBE functionals (Antonelli et al., 2019c) and the lowest-Ca end-members for
577 orthopyroxene and olivine.

578 Comparing the inter-mineral $\Delta^{44}Ca$ data to *ab-initio* predictions, we find that a significant
579 number of analyses do not agree with predictions at relevant temperatures. Additionally, a
580 significant number of samples have negative $\Delta^{44}Ca_{opx\text{-}cpx}$ (below the 1:1 line, Fig. 8a) that are not
581 predicted at any temperature. The few analyzed $\Delta^{44}Ca_{ol\text{-}plag}$ and $\Delta^{44}Ca_{ol\text{-}cpx}$ fractionations are
582 much smaller than expected for relevant temperatures in peridotites and gabbros (Fig. 8b). A
583 small number of $\Delta^{44}Ca_{cpx\text{-}plag}$ in basalts and gabbros, however, are in approximate agreement
584 with predictions, but have much larger relative uncertainties (Fig. 8c), while the clinopyroxene-
585 plagioclase fractionation in a dacitic volcanic rock is found to be significantly larger than
586 expected (as a likely consequence of rapid plagioclase growth, discussed in Section 6.3).

587 Although a negative correlation is observed between Ca concentrations in orthopyroxene and
588 $\Delta^{44}Ca_{opx\text{-}cpx}$ in igneous rocks (which is in the same direction as expected from dilution effects),
589 the observed effects are greater than equilibrium predictions at relevant temperatures, and Ca
590 dilution effects are negligible for the analyzed range of orthopyroxene Ca/(Ca+Mg).

591 The Ca concentration in orthopyroxene, however, is known to increase with increasing
592 temperature (Brey and Kohler, 1990), and is commonly used as a geothermometer ('Ca-in-Opx
593 thermometry'). Thus, increased Ca contents in orthopyroxene should lead to smaller
594 fractionations not only due to (i) increasing average Ca-O bond lengths with increasing Ca, but
595 also due to (ii) decreasing equilibrium isotope fractionations with increasing temperatures.
596 Neither of these effects, however, can explain the range of observed data, which suggests that
597 orthopyroxene-clinopyroxene mineral pairs are often out of isotopic equilibrium and that the
598 rough inverse correlation between Ca in orthopyroxene and $\Delta^{44}Ca_{opx\text{-}cpx}$ (Chen et al., 2019b) is
599 likely due to disequilibrium effects (discussed in Section 6.2).

600 **4.2. Metamorphic minerals**

601 Ca isotope variability in metamorphic minerals is even larger than observed in igneous minerals,
602 with a $\delta^{44}Ca_{BSE}$ range of ~8‰ (-2.2 to +5.8‰, Fig. 9a), but minerals from only three
603 metamorphic-facies (amphibolite, eclogite, and granulite-facies), have been analyzed in a total of
604 only four studies (Antonelli et al., 2019c; Bessey, 2018; Kang et al., 2019; Wang et al., 2019).
605 Mineral $\delta^{44}Ca$ compositions in granulites are the most variable, with a $\delta^{44}Ca$ range of ~3‰ in
606 garnet, ~6‰ in orthopyroxene, ~5‰ in plagioclase, and ~2.5‰ in perthitic K-feldspar. The only
607 mineral with a relatively limited $\delta^{44}Ca$ range (< 0.5‰) is clinopyroxene, which appears to always
608 have Ca isotope compositions close to BSE. In lower temperature metamorphic facies (eclogite
609 and amphibolite), $\delta^{44}Ca$ variability is more limited in all minerals, observed to be within ~1‰ of
610 BSE (Fig. 9a).

611 Inter-mineral $\Delta^{44}Ca$ values are the largest in granulite-facies rocks, ranging from -2 to +2.5‰
612 (Fig.9b), but can be highly variable for a given mineral pair (*e.g.* $\Delta^{44}Ca_{grt\text{-}fsp}$ ranges from -1.5 to
613 +1.5 and $\Delta^{44}Ca_{opx\text{-}fsp}$ ranges from 0.0 to +2.5‰). In amphibolite- and eclogite-facies rocks, inter-
614 mineral $\Delta^{44}Ca$ values range from -0.5 to +1‰. The most negative $\Delta^{44}Ca$ fractionation in these
615 rocks is for an apatite-clinopyroxene pair from an eclogite sample, while the most positive values
616 are for garnet-apatite, garnet-calcite, and garnet-clinopyroxene. Note that these statements are
617 somewhat definitional, such that the most positive $\Delta^{44}Ca$ values would be the most negative if
618 defined in the opposite sense (*i.e.* $\Delta^{44}Ca_{ap\text{-}grt}$ instead of $\Delta^{44}Ca_{grt\text{-}ap}$).

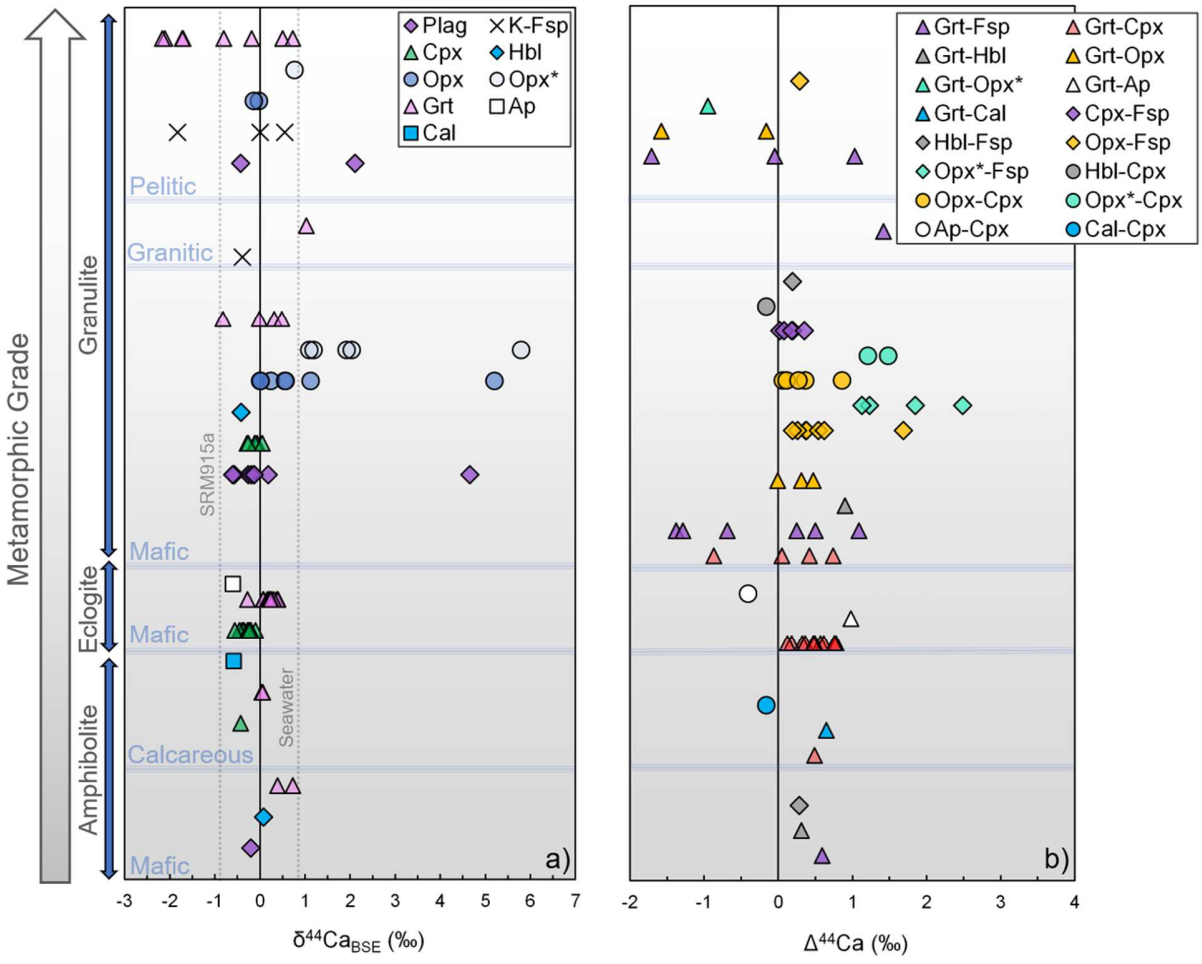

619

620 **Fig. 9a,b.** Ca isotope variations in metamorphic minerals, grouped by metamorphic-facies and protolith
621 composition. **(a)** $\delta^{44}Ca_{BSE}$ of metamorphic mineral separates (n = 81) and **(b)** inter-mineral Ca isotope differences
622 ($\Delta^{44}Ca$) in metamorphic rocks (n = 66). Triangles correspond to $\Delta^{44}Ca_{grt\text{-}min}$, diamonds correspond to $\Delta^{44}Ca_{min\text{-}fsp}$,
623 and circles correspond to $\Delta^{44}Ca_{min\text{-}cpx}$. Approximate 2sd uncertainties for $\delta^{44}Ca$ are ±0.1‰. Opx* corresponds to
624 pure orthopyroxene estimates from unmixing calculations which can have variable uncertainties based on the
625 unmixing parameters [average 2sd of ~0.5‰ (Antonelli et al., 2019c)]. Data are from (Antonelli et al., 2019c;
626 Bessey, 2018; Kang et al., 2019; Wang et al., 2019).

627 Comparing the measured inter-mineral $\Delta^{44}Ca$ values to ab-initio predictions at relevant
628 temperatures (Fig. 10), we find — similar to the igneous mineral pairs— that many represent
629 isotopic disequilibrium. Garnet-mineral pairs in granulite-facies rocks are found to deviate

630 furthest from ab-inito equilibrium predictions, with minerals from pelitic granulites having the
631 greatest apparent disequilibrium effects, while lower-grade metamorphic garnet-mineral
632 fractionations are closer to equilibrium predictions. Orthopyroxene-mineral fractionations in
633 granulite-facies rocks also tend to suggest isotopic disequilibrium, with orthopyroxene $\delta^{44}Ca$
634 compositions either too negative or too positive compared to predictions at relevant temperatures
635 (Fig. 10c-e). Clinopyroxene-plagioclase fractionations, however, are in approximate agreement
636 with equilibrium predictions, similar to observations from igneous mineral pairs. Indeed, the
637 largest inter-mineral disequilibrium effects observed in granulite-facies rocks appear to be
638 limited to rocks with less than ~15% modal clinopyroxene (Antonelli et al., 2019c). When
639 clinopyroxene is present, the observed inter-mineral fractionations tend to better agree with
640 equilibrium predictions, and thus, mafic (*vs.* pelitic) granulites tend to have fractionations closer
641 to equilibrium. This could be a potential manifestation of (i) protolith-based differences in
642 diffusive transport/paragenetic processes or may suggest that (ii) isotopic heterogeneities in
643 pelitic precursor minerals are somehow carried over (discussed in Section 6.2).

644 It appears that the magnitude of disequilibrium effects increases with increasing temperatures in
645 granulite-facies rocks, potentially due to the activation of otherwise subordinate diffusion
646 pathways/mechanisms (Antonelli et al., 2019c). Garnet-mineral and garnet-whole-rock (WR)
647 fractionations deviate further from equilibrium predictions with increasing WR and garnet Mg#
648 (Fig. 11), and orthopyroxene-mineral fractionations increasingly deviate from equilibrium
649 predictions with WR Mg#, feldspar anorthite component, modal orthopyroxene, and
650 orthopyroxene Ca/Mg, all of which tend to increase with temperature (Antonelli et al., 2019c).
651 The trend of increasing $\Delta^{44}Ca_{opx\text{-}min}$ with increasing orthopyroxene Ca/Mg, however, is the

opposite of that observed in mantle mineral separates, suggesting a different underlying mechanism for the disequilibrium fractionations.

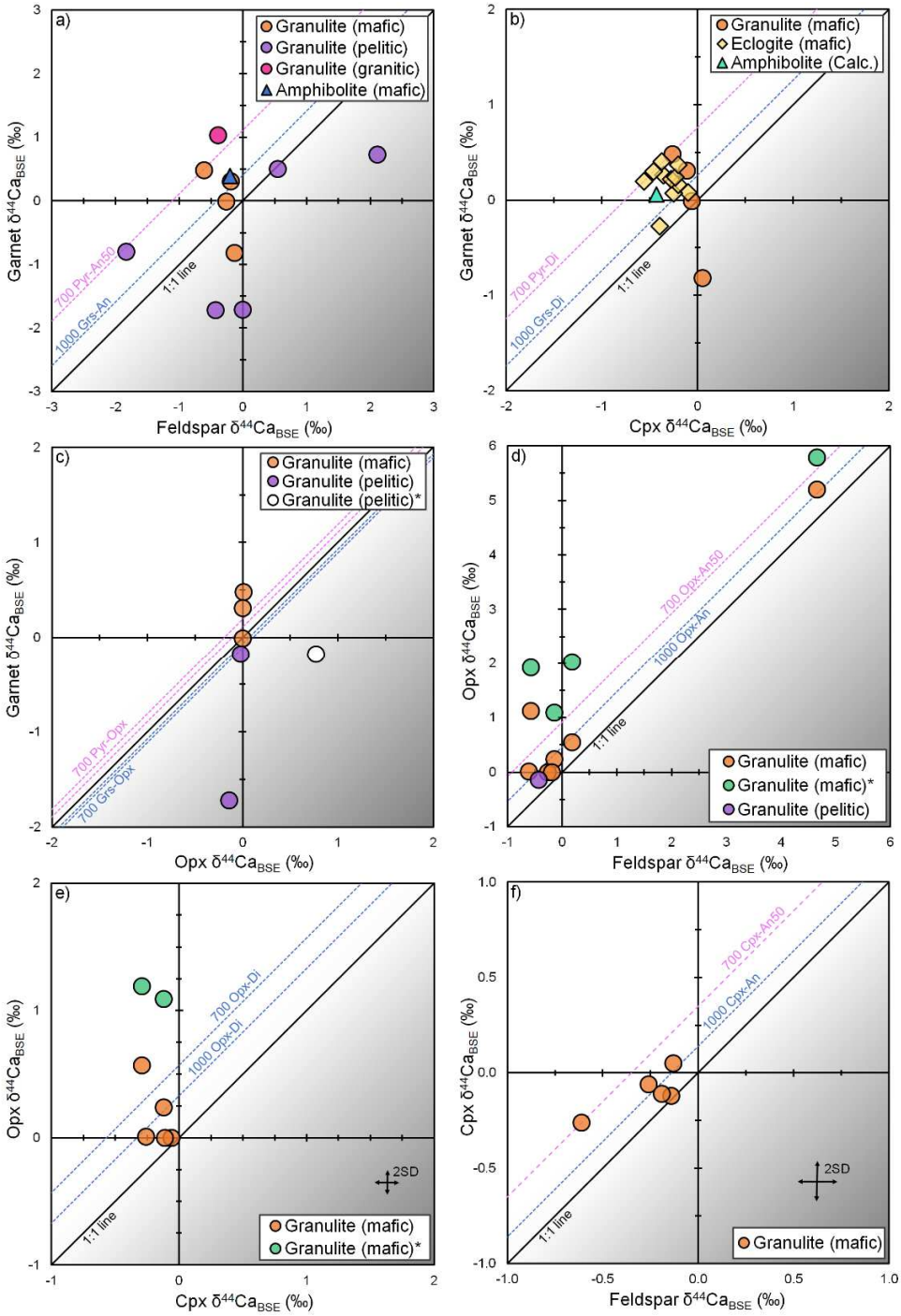

Fig. 10a-f. Ca isotope cross-plots for minerals from metamorphic rocks, grouped by rock-type, with temperature contours representing ab-initio equilibrium predictions from DFT estimates. Garnet-mineral predictions depend on the garnet end-member chosen, with pyrope having the highest predicted 1000lnβ and grossular having the lowest 1000lnβ. In order to represent the full range of fractionations expected at equilibrium, we report grossular-mineral predictions at high temperatures (1000°C) and pyrope-mineral predictions at lower temperatures (700°C). We also chose a similar approach for feldspar predictions, where mineral-anorthite is reported at high temperatures and mineral-labradorite (An50) are reported at lower temperatures. **(a)** $\delta^{44}Ca_{grt}$ *vs.* $\delta^{44}Ca_{fsp}$ (n = 11), **(b)** $\delta^{44}Ca_{grt}$ *vs.* $\delta^{44}Ca_{cpx}$ (n = 16), **(c)** $\delta^{44}Ca_{grt}$ *vs.* $\delta^{44}Ca_{opx}$ (n = 6), **(d)** $\delta^{44}Ca_{opx}$ *vs.* $\delta^{44}Ca_{fsp}$ (n = 12), **(e)** $\delta^{44}Ca_{opx}$ *vs.* $\delta^{44}Ca_{cpx}$ (n = 7), **(f)** $\delta^{44}Ca_{cpx}$ *vs.* $\delta^{44}Ca_{fsp}$ (n = 5). Asterisk (*) denotes unmixed orthopyroxene $\delta^{44}Ca$ estimates. DFT predictions are based on PBE functionals (Antonelli et al., 2019c). Data are from (Antonelli et al., 2019c; Bessey, 2018; Kang et al., 2019; Wang et al., 2019). Average 2sd uncertainties for $\delta^{44}Ca$ (~ ±0.1‰) are smaller than the symbols except for in panels (e) and (f) where they are depicted in the lower right-hand corner.

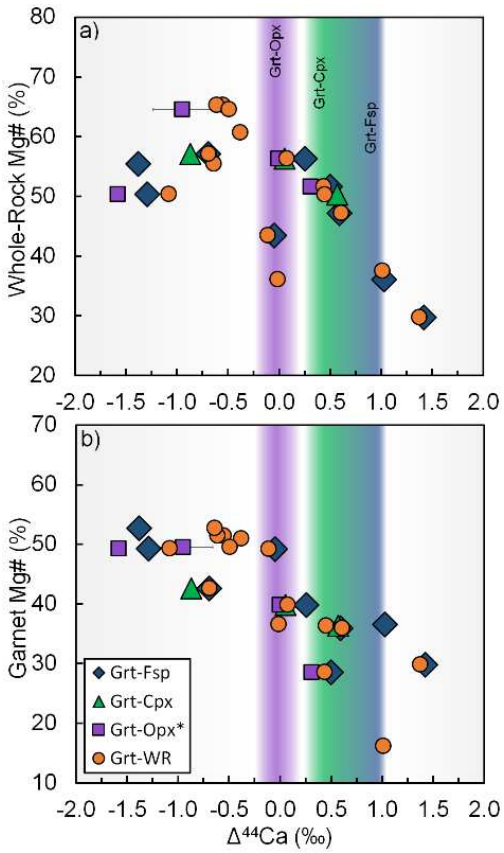

668 **Fig. 11a,b.** Whole-rock and mineral composition controls on $\Delta^{44}Ca$ in eclogite, amphibolite, and granulite-facies
669 rocks after Antonelli et al. (2019c). Garnet-mineral and garnet-whole rock $\Delta^{44}Ca$ versus **(a)** whole rock Mg# and **(b)**
670 garnet Mg#. Error bars are generally smaller than the symbols. Colored bands indicate predicted equilibrium at 800-
671 900 °C from ab-initio estimates (Antonelli et al., 2019c): Grt-Opx (purple), Grt-Cpx (green), Grt-Fsp (blue).
672 Orthopyroxene predictions are based on Ca:Mg of 1:63.

673 In sum, inter-mineral $\Delta^{44}Ca$ variability in igneous and metamorphic rocks suggests that kinetic
674 effects occur (and are subsequently preserved) at high-temperatures, however, the quantification
675 of these effects relies mainly on the accuracy of *ab-initio* predictions for equilibrium
676 fractionation and may be limited by various model assumptions. Although no experimental
677 constraints are yet available for equilibrium Ca isotope fractionation (and represent important
678 targets for future work), equilibrium and kinetic effects can potentially be distinguished using a
679 triple-isotope approach (Antonelli et al., 2019c).

680 **5. Distinguishing kinetic from equilibrium fractionations**

681 The accurate quantification of equilibrium *vs.* kinetic effects and their applicability in different
682 high-temperature systems is of paramount importance to Ca isotope geochemistry. This is
683 because isotope fractionation factors are necessary inputs for most models (*e.g.* partial melting,
684 crystallization, & diffusion models) that attempt to quantify high-temperature phenomena using
685 $\delta^{44}Ca$ and $\Delta^{44}Ca$ data. Extents of melting and fractional crystallization based on Ca isotopes, for
686 example, are often calibrated by either (i) assuming isotopic equilibrium (*i.e.* fractionation
687 factors based on DFT models), or (ii) measuring inter-mineral $\Delta^{44}Ca$ in coexisting minerals and
688 assuming that these correspond to all of the fractionations occurring in a system. Both of these
689 approaches have their own limitations, with the first approach assuming that DFT models are
690 accurate for natural systems and that the various processes are happening at isotopic equilibrium,

691 and the second approach assuming that, whether or not the fractionations are at equilibrium, that
692 $\Delta^{44}Ca$ is invariable in the system.

693 **5.1. Chemical *vs.* isotopic equilibrium**

694 Various lines of reasoning are often used in order to defend the applicability of equilibrium
695 fractionation factors derived from DFT and/or to suggest that measured $\delta^{44}Ca$ values are
696 representative of isotopic equilibrium. These include observations of: (i) textural equilibrium
697 and/or grain homogeneity, (ii) chemical equilibrium between minerals, paired with assumptions
698 about the relative rates for isotopic *vs.* chemical equilibration, and/or (iii) assumptions regarding
699 short length-scales for Ca diffusion (*e.g.* closed-system for Ca at the hand-sample scale). There
700 are several issues with these approaches, however, with the most significant being that, for a
701 given element – *chemical-equilibrium is not a sufficient condition for isotopic equilibrium*.

702 Potential confusion surrounding the relationship between isotopic and chemical equilibrium
703 comes from the high-temperature experimental community, where the word *equilibrate* is used
704 in the sense of *isotopic homogenization* across experimental diffusion couples (Baker, 1989;
705 Laan et al., 1994; Lesher, 1994, 1990; Watkins et al., 2011), and not in the sense of free-energy
706 minimization. In these diffusion experiments, it is observed that the initial pulse of isotopic
707 fractionation (where ^{40}Ca diffuses faster than ^{44}Ca, discussed in Section 6) levels out faster than
708 the chemical concentration gradient between the two starting materials (F. Huang et al., 2010;
709 Richter et al., 2009, 2003, 1999; Watkins et al., 2017, 2014, 2011, 2009). Thus, a not uncommon
710 statement from these types of studies is that isotopic equilibration occurs faster than chemical
711 equilibration, which has been taken at face value and used in several Ca isotope studies claiming
712 isotopic equilibrium.

713 The thermodynamic drive for chemical reactions is several orders of magnitude larger than for
714 isotopic substitution reactions (*e.g.* Chacko et al., 2001). In order to minimize free energy in a
715 system, therefore, isotopic equilibration is largely subordinate to chemical equilibration.
716 Maintaining isotopic equilibrium during an ongoing chemical reaction depends mainly on the
717 forward and backward exchange rates greatly exceeding the overall net reaction rate (DePaolo,
718 2011). Although one can envision a case where the net chemical reaction rate is so slow that the
719 forward and backward exchange rates at the crystal surface are much larger (*e.g.* extremely slow
720 carbonate precipitation), and could thus potentially maintain near isotopic equilibrium
721 throughout the reaction, this is unlikely to apply in a majority of cases (DePaolo, 2011). As noted
722 by many early experimental studies (*e.g.* Clayton, 1959; Matsuhisa et al., 1978; Matthews, 1976;
723 O'Neil and Taylor, 1969, 1967), mineral-synthesis, phase-change, and ion-exchange reactions
724 are susceptible to kinetic isotope effects that are not likely to reach subsequent isotopic
725 equilibrium, even over extended time-scales.

726 Ca isotope measurements in natural samples also suggest that chemical equilibrium generally
727 precedes isotopic equilibrium, even at high temperatures. For Ca isotopes in granulite-facies
728 metamorphic rocks, it has been shown that significant inter-mineral Δ^{44}Ca disequilibrium can
729 still exist, even when held at high-temperatures (~900°C) over extended time periods (10^7-10^8
730 years) and when Fe-Mg exchange and Ca-in-Opx thermometry indicate approximate chemical
731 equilibrium (Antonelli et al., 2019c). These authors also observe chemical homogeneity across
732 mineral grains (*e.g.* garnet) and equilibrium (granoblastic) textures in many samples, indicating
733 that neither of these conditions are sufficient for Ca isotopic equilibrium.

734 Ca isotope distributions were also explored in samples from the Guelb el Azib Complex (a mafic
735 intrusion metamorphosed to granulite-facies and subsequently retrograded through amphibolite

and greenschist-facies), where mineral-specific $\delta^{44}Ca$ values were estimated based on Monte Carlo simulations [combining whole-rock and mineral chemical compositions, whole-rock $\delta^{44}Ca$, and modal mineralogy estimates (Valdes et al., 2019)]. Although not explicitly discussed by the authors, the development and preservation of disequilibrium isotopic compositions is evidenced by the large $\delta^{44}Ca$ variations (up to ~ 3‰) estimated for the same mineral phases (*e.g.* amphibole, plagioclase) with otherwise similar chemical compositions across different samples.

Finally, the assumption that Ca isotopes behave as a closed-system on the hand-sample scale during high-temperature metamorphism, used in order to look-through potential metamorphic effects and quantify Ca isotope fractionation during fractional crystallization (Valdes et al., 2019), is in disagreement with results from spatially-constrained granulite-facies samples that suggest diffusive Ca isotope fractionation can occur over several meters during metamorphism (Antonelli et al., 2019c). Ca diffusion in high-temperature systems with greater volatile element concentrations (and higher Ca diffusivities) could thus occur over even greater distances, given sufficiently large timescales.

5.2. The triple Ca isotope method ($\Delta^{48}Ca$')

Although no experimental constraints are available, in order to confirm ab-initio predictions, a recent study has exploited the predicted differences between kinetic and equilibrium mass-fractionation laws in order to (i) corroborate DFT estimates and (ii) confirm the kinetic origins of large (>1‰) fractionations in high-temperature whole-rocks and minerals (Antonelli et al., 2019c). In triple isotope space ($^{48}Ca/^{44}Ca$ *vs.* $^{42}Ca/^{44}Ca$) the predicted equilibrium mass law, based on vibrational frequency differences, is -1.751 (*e.g.* Young et al., 2002). This means that measured $^{48}Ca/^{44}Ca$ should be equal to the measured $^{42}Ca/^{44}Ca$ to the exponent of -1.751, if fractionation occurred at equilibrium. The kinetic limit, based on diffusion in an ideal gas

759 (Graham's Law), where the average speed of an isotope is inversely proportional to its mass,
760 leads to a predicted $^{48}Ca/^{44}Ca$ that is related to $^{42}Ca/^{44}Ca$ by the exponent -1.872. Thus, the
761 effects of equilibrium *vs.* kinetic fractionations should be distinguishable by measuring $^{48}Ca/^{44}Ca$
762 and comparing to $^{42}Ca/^{44}Ca$. Although ^{42}Ca-^{44}Ca-^{48}Ca were used in this study due to their large
763 relative mass differences, any combination of three Ca isotopes could theoretically be used in
764 order to quantify deviations from an equilibrium mass law. The authors define a new variable
765 ($\Delta^{48}Ca'$) which quantifies $^{48}Ca/^{44}Ca$ deviations from isotopic equilibrium (in ppm):

766 $$\Delta^{48}Ca' = \mu^{48}Ca - [(\mu^{42}Ca + 1)^{-1.751} - 1] \quad \text{(Eq. 3)}$$

767 Where $\mu^{4x}Ca$ is defined as $[(^{4x}Ca/^{44}Ca)_{sample}/(^{4x}Ca/^{44}Ca)_{standard} - 1]$ and reported in ppm. A
768 similar triple-isotope method has also been used to distinguish kinetic from equilibrium
769 fractionations for Mg and Fe isotopes (McCoy-West et al., 2018; Olsen et al., 2013; Young and
770 Galy, 2004).

771 In order to test this method, two end-member samples were initially analyzed (Antonelli et al.,
772 2019c). The kinetic end-member sample comes from rapid plagioclase crystallization in an
773 experimental tonalite sample [also investigated in (Antonelli et al., 2019b)], where plagioclase
774 and melt have a $\Delta^{44}Ca$ difference greater than 2‰. The equilibrium end-member samples
775 (plagioclase and orthopyroxene mineral separates) were taken from the Stillwater cumulate
776 gabbro, which slowly crystallized over 10-100 Ka (DePaolo and Wasserburg, 1979). In Fig. 12,
777 these end-member samples are demarcated with arrows, and can be seen to closely adhere to the
778 mass-laws predicted by the equilibrium and kinetic limits for isotope fractionation: the Stillwater
779 gabbro sample has no $\Delta^{48}Ca'$ difference between minerals, whereas plagioclase from the
780 experimental tonalite sample has a large $\Delta^{48}Ca'$ depletion relative to glass.

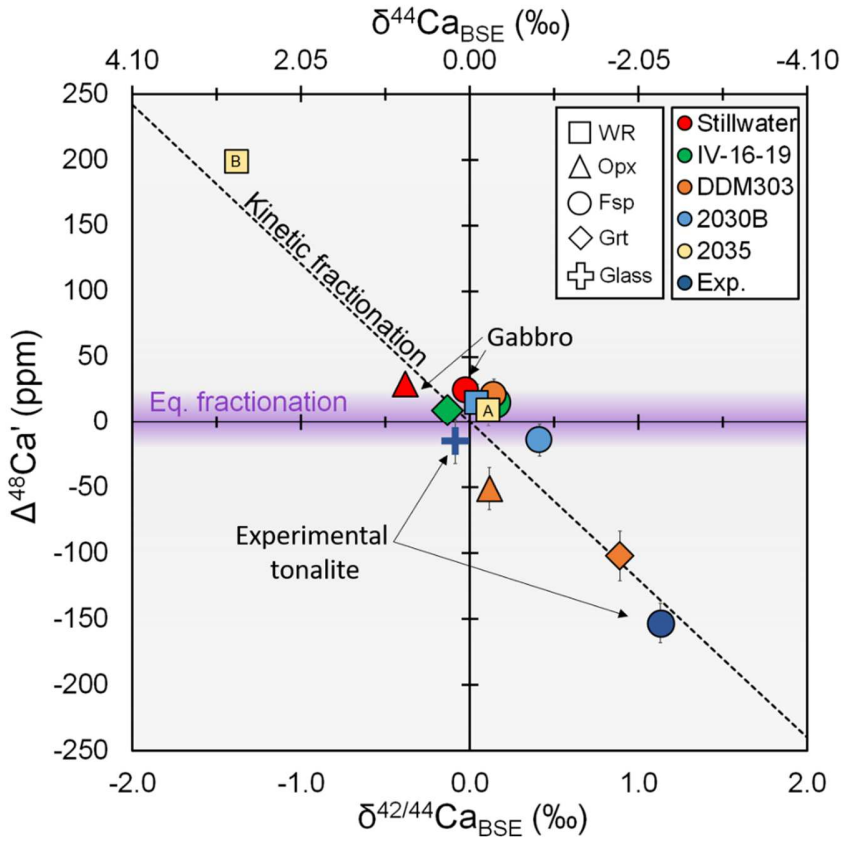

781

782 **Fig. 12.** Triple Ca isotope compositions ($\Delta^{48}Ca$' vs. $\delta^{42/44}Ca_{BSE}$) for granulite-facies whole rocks (and minerals) from
783 Diavik, Ivrea, and the Napier Complex, and for an experimental tonalite and cumulate gabbro sample, modified
784 from (Antonelli et al., 2019c). The shaded purple region demarcates the compositional field that would be expected
785 for a bulk-silicate Earth material that has not undergone any kinetic fractionations (taking into account the average
786 uncertainty of the MC-ICP-MS measurements), but it is the difference in $\Delta^{48}Ca$' between two phases that defines
787 whether or not they are at isotopic equilibrium. Cumulate gabbro from the Stillwater complex exemplifies this
788 relationship between orthopyroxene and plagioclase, whereas samples with large differences (such as plagioclase
789 and glass from the experimental tonalite and adjacent whole-rocks 2035A and 2035B, which represent the center
790 and edge, respectively, of a metamorphosed granulite-facies mafic dike hosted in quartzitic country rock) clearly
791 depict the effects of kinetic fractionation and also serve to reinforce the applicability of the theoretically-predicted
792 kinetic mass-law (dotted line). 2σ error bars correspond to 2SE of repeat analyses on the same sample and are
793 smaller than the symbols for a majority of the samples. $\delta^{44}Ca_{BSE}$ values are provided for reference at the top of the
794 figure.

795 The other data in Fig. 12 correspond to various granulite-facies rocks and minerals. The largest
796 positive $\Delta^{48}Ca'$ fractionation is between the center (2035A) and edge (2035B) of a
797 metamorphosed ultramafic dike sample from the Napier complex (Antonelli et al., 2019c), which
798 also follows the trend predicted by the kinetic limit for isotope fractionation (yellow squares
799 labeled 'A' and 'B'). Inter-mineral separates from granulite-facies samples with large $\Delta^{44}Ca$
800 differences (including Slave-province xenoliths and Napier complex samples) are also in general
801 agreement with the kinetic limit for mass fractionation. This may be surprising at first, because
802 the kinetic-limit is predicted from diffusion in an ideal gas, however, this simply implies that the
803 mass-law [typically referred to as the exponent 'β' (*e.g.* Richter et al., 1999), but not to be
804 confused with reduced partition function ratios (1000lnβ) from *ab-initio* estimates] is essentially
805 the same for $^{48}Ca/^{44}Ca$ and $^{42}Ca/^{44}Ca$. Although only a limited number of samples have been
806 analyzed, the two samples which best agree with equilibrium *ab-initio* predictions
807 [orthopyroxene and plagioclase from the Stillwater gabbro, along with garnet and feldspar from a
808 lower-crustal garnet amphibolite ('IV-16-19')] have equilibrium $\Delta^{48}Ca'$ values (Fig. 12). In the
809 absence of experimental data, this observation lends weight to the applicability of currently
810 available DFT estimates for estimating Ca isotopic equilibria between minerals (*e.g.* Antonelli et
811 al., 2019c; Huang et al., 2019; Wang et al., 2017b).

812 The triple Ca-isotope method may also allow for the separation of equilibrium and kinetic
813 fractionations in the same sample. As can be seen, for example, in the Stillwater gabbro mineral
814 separates (Fig. 12), despite having the same $\Delta^{48}Ca'$ values (equilibrium between the minerals),
815 there is a slight offset between these and bulk silicate earth ($\Delta^{48}Ca' = 0$). This implies that the
816 parent material may have undergone kinetic fractionations, before subsequent isotopic re-
817 equilibration. Given the difficulty of precisely measuring $\Delta^{48}Ca'$, however, the possibility of

distinguishing kinetic fractionations that underwent subsequent equilibrium fractionation (or vice versa) remains to be explored in future work. Although unequivocal confirmation of the kinetic mass-dependence for fractionations between minerals (and adjacent whole-rocks) was accomplished by analyzing samples with large $\delta^{44}Ca$ differences (up to ~3‰) and by targeting multiple Ca isotopes with the largest mass differences (Antonelli et al., 2019c), an earlier study used unspiked TIMS measurements (corrected with an exponential mass-law) on metasomatized peridotite mineral separates and showed that there were no $^{40}Ca/^{44}Ca$ anomalies (Zhao et al., 2017), which, although lacking the necessary precision to confirm a specific mass law, strongly suggested a kinetic control on fractionation in these samples.

6. Kinetic Ca isotope fractionation at high-temperatures

In a general sense, isotopic rate differences for dominantly unidirectional reactions (*e.g.* rapid crystal precipitation) are responsible for the large disequilibrium effects observed in $\delta^{44}Ca$. These kinetic fractionations can occur during transport of Ca isotopes towards a reaction locus, where ^{40}Ca diffuses faster than ^{44}Ca, or from isotopic rate differences during bond formation (*e.g.* at a precipitating crystal surface) or bond breaking (*e.g.* disruption of the hydration sphere around Ca^{2+} ions in water). We refer the reader to DePaolo (2011), Simon (2017), Simon and DePaolo (2010), and Watkins et al. (2017) where these topics are discussed in greater detail.

Of all the kinetic Ca isotope fractionations occurring in high-temperature terrestrial settings, diffusive Ca transport has the largest $\delta^{44}Ca$ effects, which can be an order of magnitude larger than equilibrium effects at similar temperatures (Watkins et al., 2017). Given the potential size of the effects, modeling kinetic Ca isotope fractionation (although slightly more challenging than modeling equilibrium fractionations) is often necessary in order to interpret $\delta^{44}Ca$ data from natural samples.

841 In conjunction with kinetic fractionation models, $\delta^{44}Ca$ data can yield essential information on
842 chemical reaction rates (and durations) and on the nature of Ca transport in various geochemical
843 reservoirs throughout Earth's geologic past. In this section we briefly cover the principles behind
844 kinetic Ca isotope fractionations at high temperatures, and then explore the various models used
845 to gain information from isotopic disequilibria observed in natural samples. These include
846 models constraining: (i) the duration of mantle metasomatism events, (ii) Ca transport
847 mechanisms during high-temperature metamorphism in the lower continental crust, and (iii)
848 crystal growth-rates in volcanic and sub-volcanic systems.

849 **6.1. Ca diffusion in experimental silicate liquids**

850 During diffusion in an ideal gas, kinetic isotope effects can be essentially explained by classical
851 mechanics (based on differences in translational energies) and are due to the greater average
852 speeds of lighter isotopes (at a given kinetic energy). Within more complex diffusion media,
853 such as silicate melts, however, cation diffusion occurs by hopping between interstitial sites
854 (potential energy minima within the silicate framework), and can therefore be modeled using
855 transition-state theory (Dominguez et al., 2011). The difficulty of estimating the various
856 parameters needed to estimate kinetic isotope effects from transition-state theory, however, has
857 motivated a more empirical approach towards quantifying diffusive isotope fractionation in
858 silicate liquids (F. Huang et al., 2010; Richter et al., 2009, 2003, 1999; Watkins et al., 2017,
859 2014, 2011, 2009).

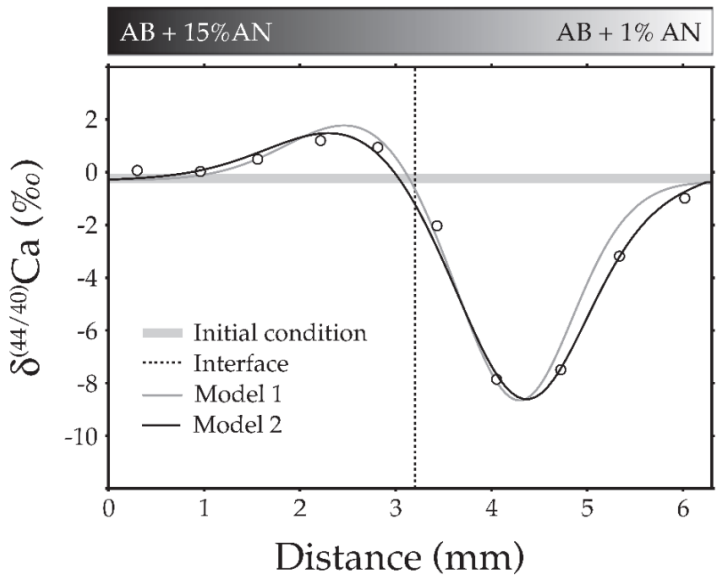

860

861 **Fig. 13.** Example of diffusion experiment results between high-An and low-An plagioclase melts at 1450°C, from
862 (Watkins et al., 2011). The low-Ca side (right) experiences a temporary negative shift in δ^{44}Ca as the ^{40}Ca diffuses
863 into it more quickly, while the high-Ca side (left) experiences a positive shift in δ^{44}Ca as the ^{44}Ca atoms are
864 preferentially left behind. In a closed system, the isotopic deviations level out to zero once ^{44}Ca has had the time to
865 'catch up' with ^{40}Ca, which generally occurs before the Ca concentration gradients reach zero. In this example, the
866 Ca isotopic fractionations are increased due to counter diffusion of Na.

867 Experiments using high-temperature diffusion couples have shown that Ca isotope fractionation
868 in silicate liquids can occur during chemical diffusion, thermal diffusion ('Soret diffusion'), and
869 even in the absence of chemical or thermal gradients ('isotopic self-diffusion') when the
870 reactants differ only in their isotopic compositions. During chemical diffusion experiments, such
871 as that shown in Fig. 13, the fractionation factor (often defined as the diffusivity of ^{44}Ca relative
872 to ^{40}Ca, D_{44}/D_{40}) depends on a variety of parameters including: (i) the degree of melt
873 polymerization (*e.g.* the diffusivity of Ca relative to that of the SiO_2 framework, as shown in Fig.
874 14a), where greater isotopic fractionations are correlated with higher SiO_2 + Al_2O_3 in the melt
875 (Fig. 14b), (ii) the direction and strength of chemical gradients for other chemical species, where

counter-diffusion (*e.g.* of Na, as in Fig. 13) generally increases the Ca isotopic fractionation, and (iii) the direction of thermal gradients imposed on the system, where heavier Ca isotopes are favored at the colder end. A detailed review of the factors influencing isotopic fractionation during diffusion in silicate liquids can be found in Watkins et al. (2017), and the reader is referred there for further information.

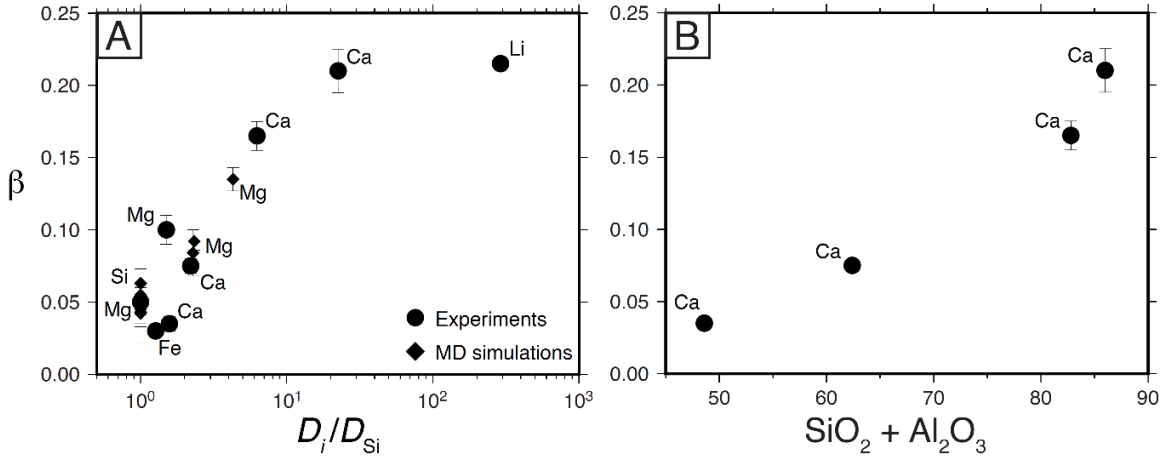

Fig. 14a,b. Experimental and molecular-dynamic simulation beta-factors versus **(a)** cation diffusivity relative to the diffusivity of silicon (D_i/D_{Si}) and **(b)** magma SiO_2 + Al_2O_3 (in wt%) after (Watkins et al., 2017). 'β' is related to D_{44}/D_{40} by $(m_{44}/m_{40})^{\beta}$ [but must not to be confused with the same variable used for reduced partition function ratios (1000lnβ, as in Figs. 4-6) presented earlier in the text], where m_{44} and m_{40} are the atomic masses of ^{44}Ca and ^{40}Ca, respectively. The efficacy of kinetic isotopic fractionation increases with increasing magma viscosity (SiO_2 + Al_2O_3), with the largest effects in high SiO_2 magmas.

6.2. Ca isotope diffusion in nature: whole-rock and inter-mineral fractionation models

Given that large (>1‰) inter-mineral and whole-rock $\delta^{44}Ca$ fractionations closely adhere to the kinetic (diffusion-based) mass law in triple isotope space (see Fig. 12), it appears that Ca diffusion is often responsible for isotopic disequilibrium observed in natural samples. However,

892 only a handful of studies have applied diffusion-based Ca isotope fractionation models to high-
893 temperature samples (Antonelli et al., 2019c, 2019b; Zhao et al., 2017).

894 The first study used disequilibrium $\delta^{44}Ca$ measurements ($\Delta^{44}Ca_{opx\text{-}cpx}$ down to -0.5‰) in
895 metasomatized mantle xenoliths in order to constrain the product of calcium diffusivity and time
896 (Dt) for mantle metasomatism (Zhao et al., 2017). By assuming various Ca diffusivities and
897 D_{44}/D_{40} values for volume diffusion (from high-Ca fluids into solid pyroxene grains), and
898 combining them with estimates for grain-sizes, geometry, and original $\delta^{44}Ca$, the authors were
899 able to constrain the duration of metasomatism by solving analytical diffusion equations (Zhao et
900 al., 2017). All of the minerals in the calculations were treated as spheres and the composition of
901 the percolating melt was assumed to not change over time, in accordance with the assumption of
902 high flow rates and high melt/peridotite ratios. The $^{44}Ca/^{40}Ca$ beta factors used in the successful
903 models varied between 0.05 and 0.10 [which are equivalent to those of an ultramafic and mafic
904 silicate liquid, respectively (see Fig. 14)], however, the models target diffusion *into* mineral
905 grains and not within the liquid phase, thus the isotopic diffusivity ratios assumed in the models
906 correspond to currently unconstrained fractionation factors for diffusion within solid minerals
907 ('volume diffusion'). Although future studies should focus on understanding Ca isotope
908 fractionations during volume diffusion in different minerals, the study (which also incorporates
909 Fe isotopes) is able to reproduce the measured isotopic fractionations with a large variety of
910 model parameter combinations [including variable clinopyroxene/orthopyroxene size ratios (0.33
911 to 0.66), temperatures (1000-1200°C), and olivine solid solution compositions (Fo90-Fo60)] and
912 uses these to constrain the duration of the associated metasomatic event to between 10^0 and 10^4
913 years (Zhao et al., 2017).

914 In a high-grade metamorphic example from the Napier Complex, disequilibrium $\Delta^{44}Ca$ between
915 adjacent whole-rocks (with known spatial constraints) were used in conjunction with numerical
916 diffusion models. Numerical methods, as opposed to analytical methods, are generally necessary
917 to model diffusion in heterogeneous media (where Ca diffusivity and D_{44}/D_{40} may vary between
918 layers). In order to constrain effective Ca diffusivities and D_{44}/D_{40} during granulite-facies
919 metamorphism in the lower crust, the authors used independent estimates for the duration of
920 high-temperature metamorphism in the Napier Complex and found that measured Ca
921 concentrations and $\delta^{44}Ca$ values were best reproduced by effective Ca diffusivity values ranging
922 from 10^{-10} to 10^{-7} m^2/yr (Fig. 15), consistent with previous estimates for Ca diffusion in high-
923 temperature rocks via grain-boundary and volume diffusion (*e.g.* Dohmen and Milke, 2010;
924 Farver and Yund, 1995; Giletti, 1994; Keller et al., 2008; Vielzeuf et al., 2007). The authors also
925 found that isotopic diffusivity ratios (D_{44}/D_{40}) of ~0.99 were necessary in order to reproduce the
926 measured $\delta^{44}Ca$ of the various units.

927 Given the existing experimental constraints for D_{44}/D_{40} in various media, a value of ~0.99
928 suggests that grain-boundary diffusion likely occurred within silicate melts as opposed to within
929 aqueous fluids [where fractionation factors are expected to be much smaller (*e.g.* Watkins et al.,
930 2017)]. As there is an on-going debate regarding the dominant mechanism through which
931 granulite-facies rocks lose their incompatible elements (*e.g.* dehydration *vs.* partial-melting/melt-
932 loss), these results, along with those previously described for mantle xenoliths (Zhao et al.,
933 2017), serve to highlight the potential for pairing diffusion models with disequilibrium Ca
934 isotope variations in order to constrain both the nature and rates of processes important to both
935 igneous and metamorphic petrology.

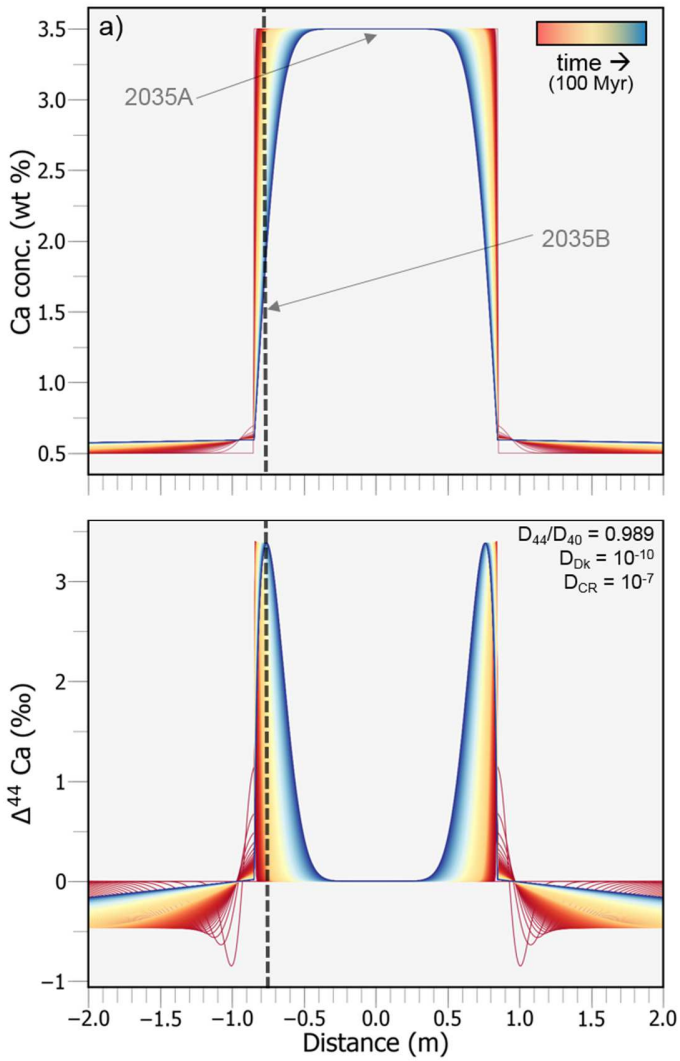

936

937 **Fig. 15.** Results of numerical modeling for Ca isotope diffusion between a high-Ca ultramafic dike and low-Ca
938 pelitic country rock, metamorphosed at granulite-facies conditions for 100 Myr from (Antonelli et al., 2019c). The
939 top panel shows changing Ca concentrations and the bottom panel shows the corresponding $\Delta^{44}Ca$ values over time
940 (where $\Delta^{44}Ca$ corresponds to $\delta^{44}Ca_{initial}$-$\delta^{44}Ca_{final}$). The two analyzed samples (also shown in Fig. 12) come from the
941 center ('2035A') and ~8cm from the edge ('2035B' demarcated by the dashed lines) of a ~1.7m thick dike and have
942 pronounced Ca concentration and $\delta^{44}Ca$ differences, with the edge (~1.5 wt% Ca) being +3.3‰ heavier than the
943 center (~3.5 wt% Ca). The initial conditions assume uniform $\delta^{44}Ca$ (and Ca concentration) across the dike, which
944 slowly increase as Ca diffuses into the country rock. In order to reproduce the measured $\delta^{44}Ca$ and Ca
945 concentrations at the correct locations, Ca diffusivities must equal ~10^{-10} m^2/yr and ~10^{-7} m^2/yr in the dike and

946 country rock, respectively. The required isotopic diffusivity ratio (D_{44}/D_{40}) is ~0.99, similar to that in dacitic liquids
947 (see Fig. 14b). Additional details and diffusion model results for more complicated scenarios and rock-types can be
948 found in the supplementary information of Antonelli et al. (2019c).

949 Another emerging application for disequilibrium inter-mineral $\Delta^{44}Ca$ data is to constrain
950 metamorphic mineral paragenesis. Preliminary results from the previously discussed granulite
951 study (Antonelli et al., 2019c) suggest that $\Delta^{44}Ca_{grt\text{-}mineral}$ fractionations are related to the
952 pressure-temperature-time (PTt) paths for metamorphism, where retrograde garnet formation
953 (*e.g.* during isobaric cooling from ultrahigh-temperatures) leads to negative disequilibrium
954 $\Delta^{44}Ca_{grt\text{-}mineral}$ values, and prograde garnet formation (clockwise PTt paths) appears to generate
955 positive $\Delta^{44}Ca_{grt\text{-}mineral}$ values closer to predicted isotopic equilibrium (schematically depicted in
956 Fig. 16). Combined with the observed kinetic slopes for negative garnet-plagioclase
957 fractionations in triple isotope space (Fig. 12), this observation suggests that Ca sourced from
958 plagioclase may be subjected to kinetic effects during diffusive transport towards growing garnet
959 grains during isobaric cooling (Antonelli et al., 2019c). The large kinetic effects during
960 retrograde garnet formation, that appear to be essentially absent during prograde and magmatic
961 garnet formation, could be due in part to the removal of volatile elements prior to its formation.
962 However, very few samples have been measured and further work is required in order to better
963 understand the origins of disequilibrium Ca isotope signatures observed between various
964 metamorphic minerals.

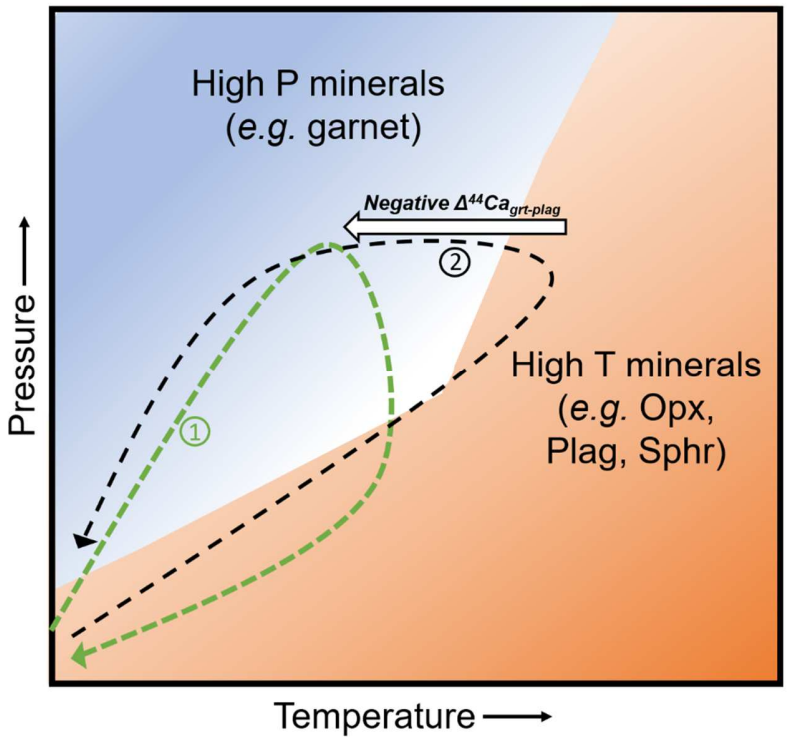

965

966 **Fig. 16.** Simplified conceptual phase diagram depicting the hypothesized effects of pressure-temperature-time (PTt)
967 paths on the Ca isotopic differences observed between garnet and other minerals, as described in (Antonelli et al.,
968 2019c). Path 1 (dashed green line) corresponds to a 'clockwise' heating path resulting in prograde garnet formation
969 closer to isotopic equilibrium, while path 2 (dashed black line) corresponds to a 'counter-clockwise' path in which
970 garnet is formed during isobaric cooling from very high-temperatures ('retrograde garnet growth') and acquires a
971 negative disequilibrium $\Delta^{44}Ca_{grt\text{-}plag}$ signature (likely due to Ca diffusion, as suggested by $\Delta^{48}Ca$' measurements).

972 By constraining Ca isotope compositions in individual grains (through the development of in-situ
973 $\delta^{44}Ca$ analyses or more refined sampling techniques) and the average length-scales for Ca
974 diffusion within a given system (*e.g.* through chemical image analyses), future studies should be
975 able to yield important information on mineral paragenesis and Ca isotope disequilibrium related
976 to metamorphic reactions.

977 Although our current state of knowledge on this topic is in its infancy, the various possibilities
978 regarding isotopic fractionation during high-temperature metamorphic reactions can still be

evaluated. When a new phase is created at the expense of an existing phase ('net-transfer reaction'), for example, the Ca isotopic composition of the precursor mineral(s) may be (i) at equilibrium with the product phase (if the forward and backward exchange rates are much larger than the net reaction rate), (ii) directly passed-on to the product phase (which would then require subsequent isotopic re-equilibration with surrounding minerals), or (iii) subjected to kinetic fractionation effects due to isotopic rate differences during bond breaking, diffusive transport (within minerals or along grain-boundaries), and/or bond formation at the new mineral surface (thereby inheriting an isotopic composition different from the precursor). During exchange reactions, which are often used for geothermometry, pre-existing phases exchange components in order to reach chemical equilibrium (*e.g.* Fe-Mg exchange between ferromagnesian minerals and Ca exchange between clinopyroxene and orthopyroxene). Given that the exchange of components is diffusive in nature, kinetic Ca isotope effects could occur via both volume and grain-boundary diffusion. Upon completion of the chemical exchange, the new mineral may have to isotopically re-equilibrate with surrounding phases in the absence of a chemical potential gradient ('isotopic self-diffusion'), which may be exceedingly slow. Future studies of spatially constrained δ^{44}Ca variations across minerals and grain boundary interfaces should allow us to evaluate the possible mechanisms for inter-mineral Ca isotope disequilibrium in metamorphic samples.

6.3. Crystal growth rates from Ca isotope disequilibrium in volcanic systems

Crystal growth rates in magmatic systems are especially important for understanding the physical processes leading up to volcanic eruptions. Current methods, such as crystal-size distribution (CSD) analyses or trace-element diffusion profile models [see Cooper (2019)], however, must generally assume crystal-growth rates *a priori* in order to arrive at timescale estimates for the

1002 associated volcanic process. Given that crystal growth rates in magmatic systems vary by at least
1003 five orders of magnitude in nature (Cooper, 2019), they constitute a major uncertainty in
1004 estimating the durations of past volcanic eruption and magmatic recharge events. In order to
1005 address this problem, Ca isotope disequilibria have recently been used to independently estimate
1006 crystal-growth rates in volcanic and sub-volcanic samples (Antonelli et al., 2019b).

1007 Ca isotope growth rate estimates are based on the model predictions of Watson and Müller
1008 (2009), where diffusion through a chemically-distinct boundary-layer (BL, formed around
1009 rapidly growing phenocrysts) can lead to kinetic isotope effects during crystal growth. If growth
1010 rates are rapid relative to Ca diffusivity in the melt (R/D), this is predicted to generate
1011 disequilibrium Δ^{44}Ca variations in the crystals. As depicted in Fig. 17, crystallization of minerals
1012 where Ca is compatible (K > 1, *e.g.* plagioclase, clinopyroxene) is expected to lead to formation
1013 of a Ca-depleted BL (through which ^{40}Ca diffuses faster than ^{44}Ca) and negative kinetic Δ^{44}Ca,
1014 whereas the opposite is expected if Ca is strongly incompatible within the mineral (K < 1, *e.g.*
1015 olivine, orthopyroxene) (Fig. 17).

1016 The predicted kinetic fractionations during crystal growth depend on: (i) crystal growth-rates
1017 relative to Ca diffusivity (*R/D*), (ii) isotopic differences in Ca diffusion coefficients (D_{44}/D_{40})
1018 (iii) mineral-melt Ca distribution coefficients, and (iv) boundary-layer (BL) thicknesses around
1019 the growing crystals (Watson and Müller, 2009). Given the development of a steady-state BL
1020 during crystal growth, the kinetic δ^{44}Ca fractionation between crystals and melt (Δ^{44}Ca) is given
1021 by:

1022 $$\Delta^{44}Ca = 10^3 \left(1 - \frac{D_{40}}{D_{44}}\right) \frac{R \times BL}{D_{40}} (1 - K) \qquad \text{(Eq. 4)}$$

where D_{40} and D_{44} are the diffusivities of ^{40}Ca and ^{44}Ca in the melt, respectively, R is the crystal growth rate, BL is the boundary layer thickness, and *K* is the Ca distribution coefficient in the mineral *vs.* the melt (generally $K > 1$ in plagioclase).

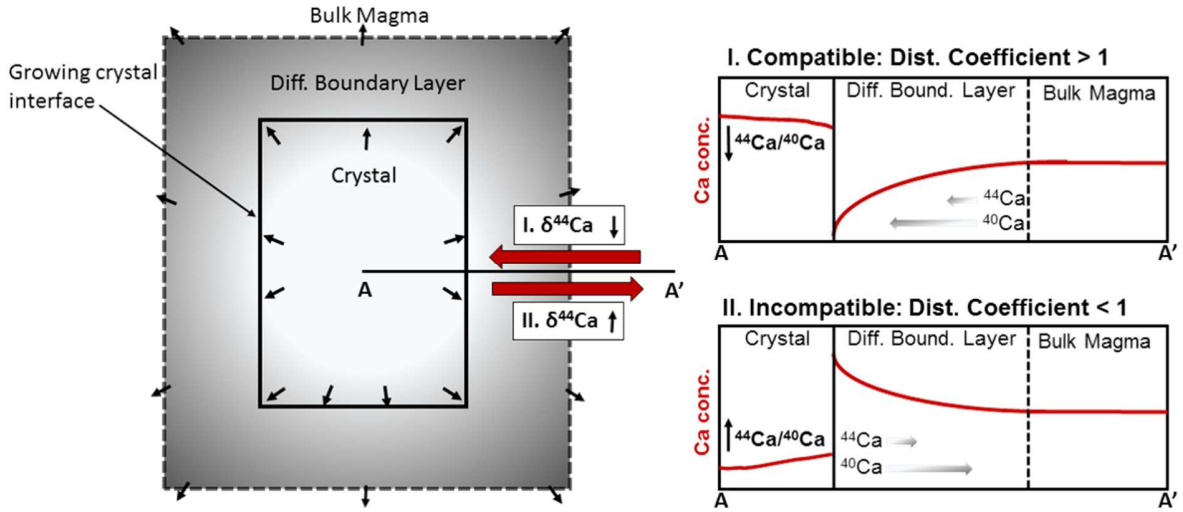

Fig. 17. Schematic diagram showing the effects of Ca diffusion through a chemically-distinct boundary layer (BL) surrounding a growing crystal, based on the model of Watson and Müller (2009), figure from Antonelli et al. (2019b). When Ca is compatible within a mineral, depletion of Ca in the BL leads to an enrichment of ^{40}Ca at the mineral surface due to diffusion through the BL towards the crystal (top right panel); when Ca is incompatible, build-up of Ca in the BL leads to a relative enrichment of ^{44}Ca at the crystal surface as Ca diffuses away from the crystal (lower right panel). For further details see Antonelli et al. (2019b), Watkins et al. (2017), and Watson and Müller (2009).

Analyzing plagioclase separates from rapid tonalite crystallization experiments (Antonelli et al., 2019b), it was found that the driest samples (1 wt% H_2O) have the largest fractionations ($\Delta^{44}Ca_{plag\text{-}matrix}$ = -2.2‰) which gradually become smaller with increasing water contents ($\Delta^{44}Ca_{plag\text{-}matrix}$ of -1.0‰ and -0.3‰, for the 1.5 wt% and 2 wt% H_2O experiments, respectively). Although the limited data cannot rule out changes in isotopic diffusivity ratios (D_{44}/D_{40}) and BL thicknesses due to increasing H_2O (which have not yet been explored), the most simple

1040 explanation is that water leads to increases in Ca diffusivity and decreases in R/D (Antonelli et
1041 al., 2019b). Recent work on Li isotope diffusion suggests that water concentrations do not have a
1042 significant effect on isotopic diffusivity ratios in silicate liquids (Holycross et al., 2018), but this
1043 still remains to be confirmed for Ca isotopes. In natural phenocryst samples, clinopyroxene and
1044 other mafic minerals (amphibole, olivine) have slight positive $\Delta^{44}Ca_{mineral\text{-}matrix}$ (up to +0.3‰)
1045 and plagioclase phenocrysts have slightly negative $\Delta^{44}Ca_{mineral\text{-}matrix}$ (~-0.2‰). $\delta^{44}Ca$ variations of
1046 ~0.5‰ in high-purity plagioclase separates taken from orbicules and comb-layers, however,
1047 suggest especially fast growth rates. Assuming that equilibrium $\Delta^{44}Ca_{plag\text{-}melt} = 0$ [in agreement
1048 with Zhang et al. (2018)], and using conservative estimates for the other various parameters in
1049 Equation 4 [see supplementary text of Antonelli et al. (2019b)], the authors were then able to
1050 constrain minimum crystal growth rates in the volcanic systems (Fig. 18).

1051 Although the estimated growth rates for orbicules, comb-layers, and several natural phenocryst
1052 samples are faster than commonly assumed [typically assumed to be ~0.3 cm/yr in
1053 decompressing magmas (*e.g.* Brugger and Hammer, 2010; Cooper, 2019; Cooper and Kent,
1054 2014; Salisbury et al., 2008)], they agree with previous estimates for orbicule growth [~10 cm/yr,
1055 based on textural constraints from superheated experimental magmas (McCarthy and Müntener,
1056 2016; Shea and Hammer, 2013)], and rates as high as ~30 cm/yr have been described for
1057 crystallization of experimental plagioclase spherulites (Arzilli et al., 2015).

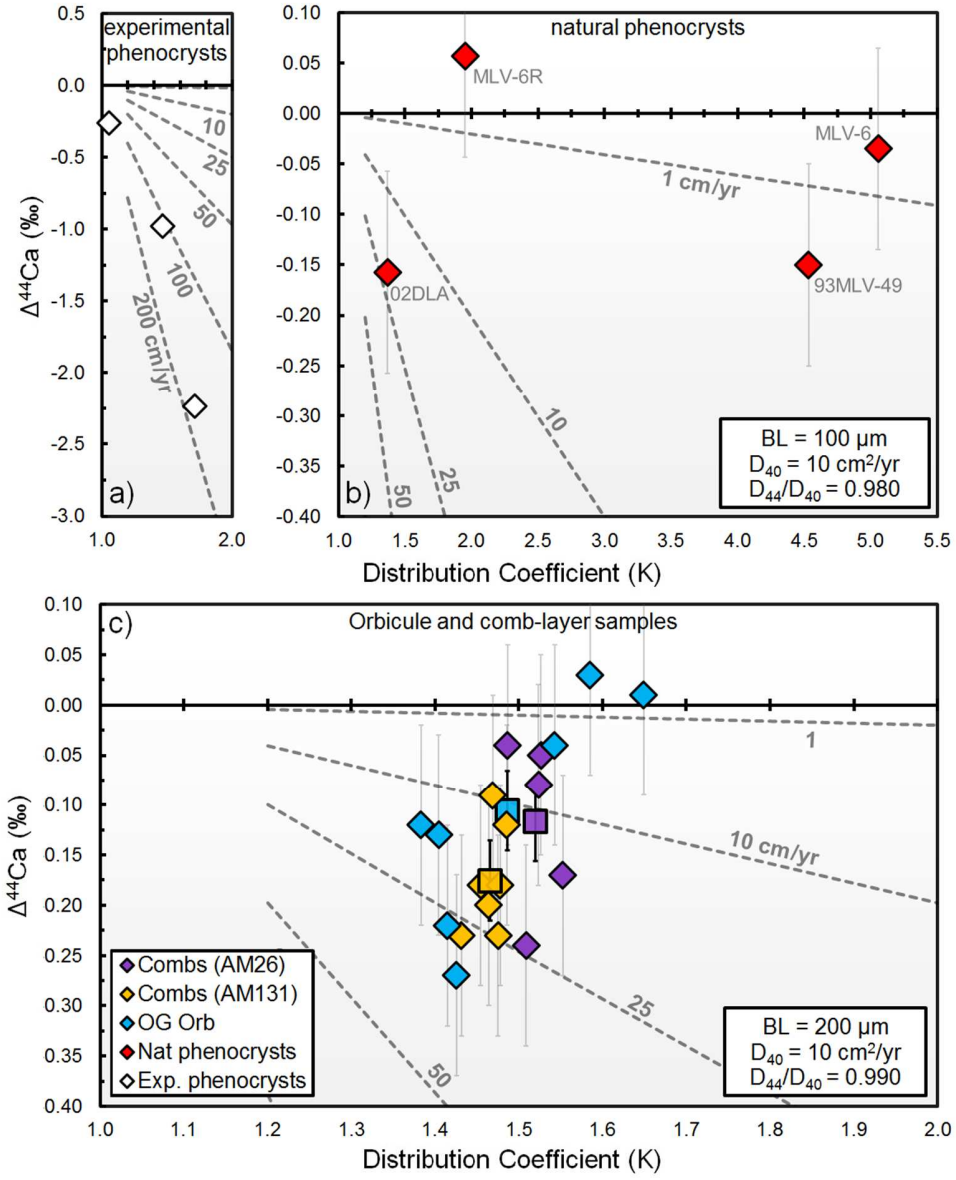

Fig. 18a-c. $\Delta^{44}Ca$ *vs.* Ca distribution coefficients for analyzed plagioclase separates from **(a,b)** experimental (n = 3) and natural phenocryst samples (n = 4) along with **(c)** separates from orbicule and comb-layer samples (Emerald Bay and Fisher Lake, n = 19) with dashed contours representing predictions for different crystal growth rates, after Antonelli et al. (2019b). In **(a,b)**, $\Delta^{44}Ca$ represents $\delta^{44}Ca$ differences between plagioclase and glass/matrix, and D_{44}/D_{40} = 0.980, in accordance with previous work shown in Fig. 14. Boundary-layer (BL) thicknesses are 100 µm, suggested as maximum values in dynamic systems (Lu et al., 1995). In **(c)**, D_{44}/D_{40} = 0.990 and $\Delta^{44}Ca$ represents kinetic effects based on differences for plagioclase $\delta^{44}Ca$ (Fisher Lake) or non-mineralogical $\delta^{44}Ca$ differences

between orbicule layers (Emerald Bay). BL sizes are 200 μm to account for larger crystal sizes in the orbs and comb-layers. Rate estimates are directly proportional to BL thicknesses, such that ½ a given BL thickness leads to double the required growth rate. Average values and 2SE for Fisher Lake samples (AM26, AM131) and kinetic layers in OG sample (Emerald Bay) are represented by colored squares (n = 3) with bold error bars in panel **(c)**.

In conjunction with crystal-size distribution (CSD) analyses and measurements of maximum crystal sizes, the authors were able to estimate the durations of crystal growth in various volcanic systems. For the mafic and silicic systems studied, the results yielded similar timescales (ranging from <1 day to ~2 months), suggesting that the previously observed relationship between magmatic timescales and melt compositions [where timescales appear to generally increase from mafic to silicic systems (*e.g.* Cooper, 2019)] may be due to *a priori* assumptions regarding crystal growth rates.

Although the initial results are promising, much work remains in order to improve $\Delta^{44}Ca$ as a proxy for crystal-growth rates in volcanic systems. This includes, for example, careful separation of different phenocryst populations for a given mineral within a sample, where populations of smaller crystals (*e.g.* plagioclase microlites) are likely to have crystallized the fastest and to contain the largest disequilibrium $\Delta^{44}Ca_{plag\text{-}melt}$ signatures. The samples shown in Fig. 18 represent mixtures of different plagioclase crystal populations (up to 3 per sample in the phenocrystic rocks), so the $\Delta^{44}Ca$ measurements represent minimum values for the rapidly-grown populations within each sample (Antonelli et al., 2019b). Furthermore, most of the parameters in Equation 1 are poorly constrained and could benefit from additional crystallization experiments and detailed observations of natural samples. This would then allow future studies to incorporate, for example, (i) the effects of multi-component diffusion into D_{44}/D_{40} estimates, which could also consider chemical variations in BL compositions, (ii) variations in BL sizes in natural and experimental systems, and (iii) compositional and pressure/temperature dependence

of Ca diffusivity in magmas. Nevertheless, preliminary results suggest that Ca isotopes provide an exciting new opportunity for understanding fundamental aspects of crystallization and magmatic recharge across volcanic systems observed on Earth today and in the geologic past.

6.4. High fluid/rock and hydrothermal systems

The Ca isotope composition of hydrothermal fluids and minerals has not been as extensively studied as low temperature weathering and carbonate mineral formation processes. Despite the relatively few studies of Ca isotopes in hydrothermal systems, high temperature fluid-mineral reactions are important for the global geochemical cycle because ocean hydrothermal systems are the second largest Ca flux to the oceans (Staudigel, 2003). Additionally, fossil hydrothermal systems record information about water rock reactions in a diverse set of geologically important environments such as porphyry deposits, continental hydrothermal systems, and ophiolites.

Shallow heat from mid-ocean ridge magmatism drives fluid circulation with the influx of seawater into the ocean crust and the emergence of high temperature (~400°C) fluids at the ridge axis that are chemically distinct from seawater. Chemical reactions in the hydrothermal flow path remove Mg and SO_4 and exchange seawater Ca (and Sr) for Ca derived from igneous minerals (*e.g.* Staudigel, 2003; von Damm, 2000). Because the Ca isotope cycle in the ocean is possibly a robust record of past climate, the effect of hydrothermal reactions on the Ca isotope composition of seawater is an important research question.

The first measurements of mid-ocean ridge hydrothermal fluids were reported by Schmitt et al. (2003), while subsequent data were reported by Amini et al. (2008), and most recently by Scheuermann et al. (2018). Sampled hydrothermal fluids are often mixed with seawater, and thus require some correction to calculate their hydrothermal endmember compositions. Figure 19 shows a compilation of hydrothermal fluid $\delta^{44}Ca$ values as a function of percent seawater, which

assumes that hydrothermal fluids have [Mg] = 0 and seawater has [Mg] = 53 mM (*e.g.* Lowenstein et al., 2013; Turchyn and DePaolo, 2019). While the data exhibit scatter and are heavily weighted at the near-zero and near-100% seawater endmembers, they suggest that high temperature hydrothermal fluids have Ca isotope compositions similar to MORB ($\delta^{44}Ca_{BSE} \approx 0$, which is approximately -1‰ relative to modern seawater).

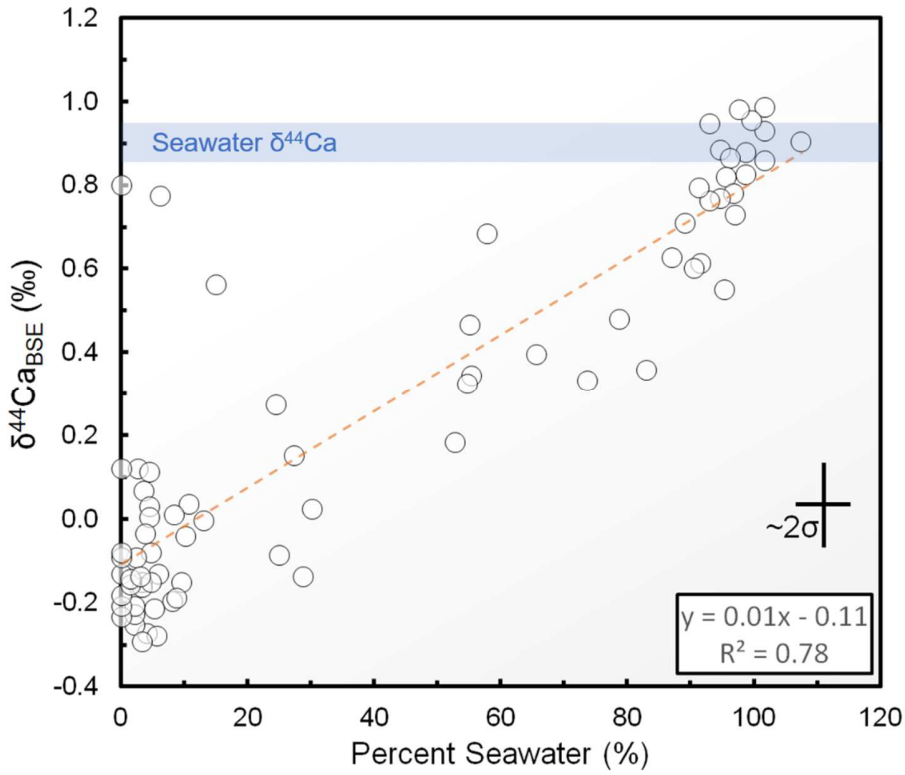

Fig 19. $\delta^{44}Ca$ of hydrothermal fluids as a function of seawater percentage. Seawater percentage is based on Mg concentrations assuming end-member hydrothermal fluids and seawater have [Mg] of 0 and 53.4 mM, respectively. Data are from (Amini et al., 2008; Scheuermann et al., 2018; Schmitt et al., 2003).

The hydrothermal fluid data are consistent with near complete Ca isotopic exchange between infiltrating seawater and basaltic minerals and require little or no net Ca isotopic fractionation in high temperature hydrothermal systems. Radiogenic Ca isotope differences reported between seawater and modern hydrothermal vents (Antonelli et al., 2019a, 2018) also suggest that the Ca

1126 within hydrothermal fluids is sourced almost entirely from oceanic crust. The Ca isotope system
1127 is thus dissimilar to $^{87}Sr/^{86}Sr$, which is incompletely exchanged in modern and some ancient
1128 hydrothermal systems (Amini et al., 2008; Antonelli et al., 2017; Turchyn et al., 2013). The
1129 complete exchange of Ca isotopes and incomplete exchange of Sr isotopes is likely due to the
1130 relative distribution between the fluid and rock phases, where $[Ca]_{basalt}/[Ca]_{seawater}$ is an order of
1131 magnitude higher than $[Sr]_{basalt}/[Sr]_{seawater}$ (Brown et al., 2020). Brown et al. (2020) presented
1132 simplified reactive transport models for Ca and Sr in mid-ocean ridge hydrothermal systems that
1133 suggest $^{87}Sr/^{86}Sr$ in hydrothermal fluids can vary as a function of paleoseawater composition [as
1134 predicted in Antonelli et al. (2017)], but $\delta^{44}Ca$ values in hydrothermal fluids are likely to be the
1135 same as MORB (or at the most ~0.1‰ displaced toward seawater) in the geologic past. In
1136 contrast, it is possible that serpentinite-hosted hydrothermal systems are shifted from local rock
1137 compositions (*e.g.* Amini et al., 2008; Scheuermann et al., 2018) and could lead to distinct
1138 hydrothermal $\delta^{44}Ca$ signatures.

1139 As opposed to oceanic hydrothermal systems, studies of continental hydrothermal systems show
1140 relatively large variations in fluid $\delta^{44}Ca$ up to 1.5‰ (Brown et al., 2013; Wiegand et al., 2015).
1141 The primary observation is that $\delta^{44}Ca$ of the hydrothermal fluids increases as the fluid Ca
1142 concentration decreases, broadly consistent with isotope fractionation during secondary mineral
1143 precipitation (Brown et al., 2013; Wiegand et al., 2015). In the case of Long Valley caldera, the
1144 $\delta^{44}Ca$ shifts are primarily attributed to secondary carbonate mineral precipitation, which is a
1145 larger magnitude effect than Ca supply by primary mineral dissolution. The magnitude of $\delta^{44}Ca$
1146 fractionation (α) for the Long Valley system was inferred using an isotope distillation model,
1147 which yielded α=0.99965, similar to observations of calcite-fluid pairs: 0.99945-0.99970 (Brown
1148 et al., 2013). While the inferred fractionations are smaller than low temperature processes such

as marine carbonate precipitation, the fractionations are greater than would be predicted by temperature-dependent equilibrium models extended from low temperature minerals (Brown et al., 2013).

Hydrothermal minerals offer an additional opportunity to assess the mechanisms and magnitude of Ca isotope fractionation in high temperature fluids. Figure 20 shows a compilation of $\Delta^{44}Ca$ for synthetic and natural hydrothermal minerals as a function of fluid temperature. In some cases the fluid and minerals were directly measured (Brown et al., 2013; Syverson et al., 2018), for others the fluid composition and temperature have been calculated based on $^{87}Sr/^{86}Sr$ and isenthalpic mixing between seawater and vent fluids (Amini et al., 2008; Griffith et al., 2008b). For epidotes, a reactive transport model was used to estimate the fluid composition (Brown et al., 2020).

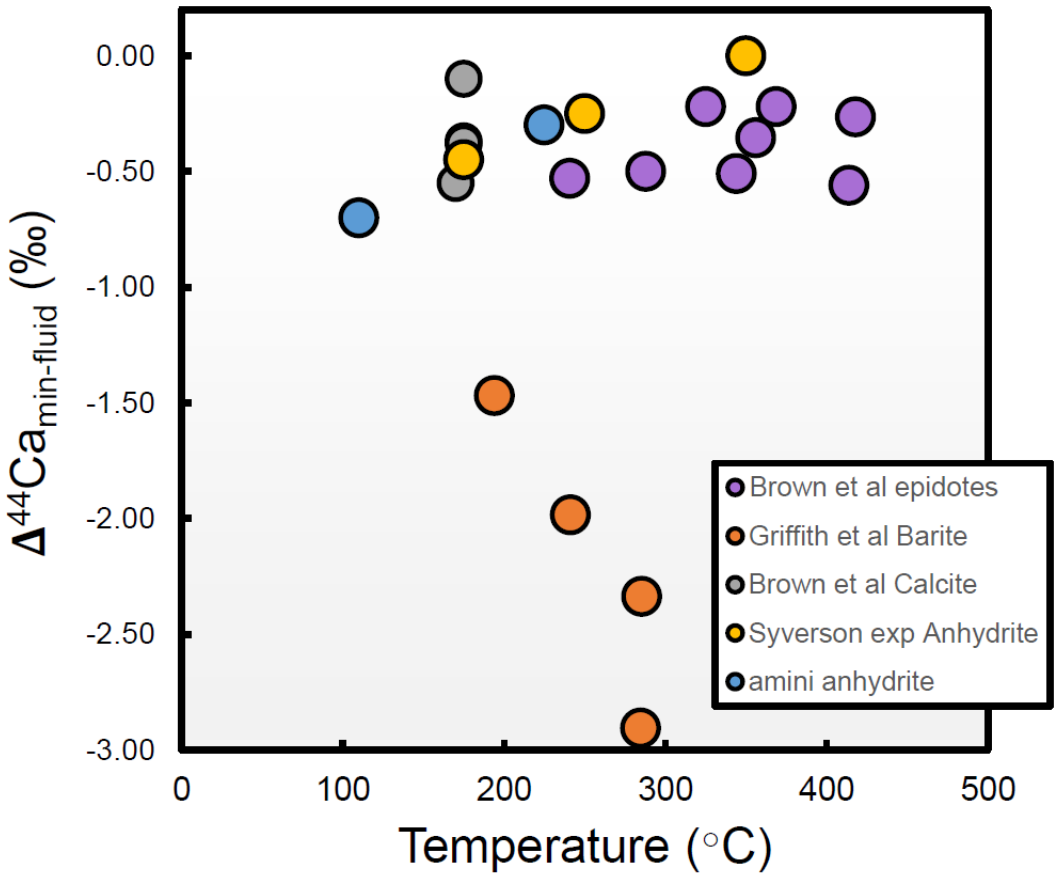

Fig. 20. Compilation of Ca isotope fractionation between hydrothermal fluids and hydrothermal minerals with increasing temperatures (n = 20). The different colors correspond to epidote (purple), barite (orange), calcite (grey), experimental anhydrite (yellow), and natural anhydrite (light blue). Data are from (Amini et al., 2008; Brown et al., 2020, 2013; Griffith et al., 2008b; Syverson et al., 2018).

The first and most significant observation is that $\Delta^{44}Ca_{mineral\text{-}fluid} \leq 0$, with only one sample at unity. Additionally, there is no obvious trend in $\Delta^{44}Ca$ with temperature for the dataset as a whole, however, the anhydrites show decreasing fractionation with increasing temperature, while the $\Delta^{44}Ca$ of barites are positively correlated with temperature (Fig. 20).

Amini et al. (2008) used the temperature dependence of $\Delta^{44}Ca$ for anhydrite to predict an average isotopic fractionation of $\Delta^{44}Ca_{fluid\text{-}anhydrite}$ of -0.54‰, but the temperature relationship is less

1171 robust if the experimental data of Syverson *et al.* (2018) are included (Fig. 20). In contrast,
1172 Brown et al. (2020, 2013) found no $\Delta^{44}Ca$ temperature dependence for hydrothermal calcite or
1173 epidote. Thus, the extent to which there is a temperature dependence to $\Delta^{44}Ca$ for hydrothermal
1174 minerals remains an open question. One possible reconciliation of the data is that the relationship
1175 between temperature and $\Delta^{44}Ca$ is actually related to rapid changes in mineral saturation with
1176 fluid temperature changes. In this case, changes in temperature might correlate with mineral
1177 saturation (greater oversaturation is generally linked to faster precipitation rates) and by
1178 extension $\Delta^{44}Ca$. This suggests that $\Delta^{44}Ca$ in hydrothermal minerals is primarily a kinetic
1179 effect—similar to the previously discussed examples for igneous and metamorphic mineral
1180 assemblages.

1181 Significant $\Delta^{44}Ca$ between hydrothermal fluids and secondary minerals offer an opportunity to
1182 quantify subsurface processes in mid-ocean ridges, economic geothermal fields, and possibly in
1183 mineralizing fluids, however, additional research is required to better understand the underlying
1184 fractionation mechanisms and their implications for fluid-rock systems. Future work should
1185 include experiments at varying water-rock ratios, fluid chemistry, and temperatures, in order to
1186 enable more quantitative interpretations of modern and fossil hydrothermal systems.

1187 **7. Employing radiogenic and stable Ca isotopes as high-temperature source-tracers**

1188 The application of Ca isotopes as a petrogenetic tracer is different but complementary to other
1189 more commonly used trace element isotope systems (*e.g.* Sr, Pb, Hf, and Pb). The K-Ca
1190 radioactive system (half-life of ~1.25 Ga), however, behaves differently because this parent-
1191 daughter system involves elements that make up stoichiometric constituents of major minerals,
1192 and therefore the concentrations of K and Ca, and the K/Ca ratio in rocks, are directly related to
1193 mineralogy (*e.g.* Marshall and DePaolo, 1989). Radiogenic Ca isotope excesses are commonly

reported using epsilon notation, after correcting for natural and instrumental mass-fractionation (using an exponential law and $^{42}Ca/^{44}Ca = 0.31221$):

$$\varepsilon_{Ca} = 10{,}000 \left[\frac{\left({}^{40}Ca/_{44}Ca \right)_{sample}}{\left({}^{40}Ca/_{44}Ca \right)_{BSE}} - 1 \right] \quad \text{(Eq. 5)}$$

Where $(^{40}Ca/^{44}Ca)_{BSE}$ is generally assumed to be 47.162, though recent work suggests that a value of 47.156 (about 1 epsilon unit lower), may be more accurate (Antonelli et al., 2019a, 2018; Mills et al., 2018). The comparatively large mass differences among Ca isotopes cause physiochemical processes to produce relatively large mass-dependent variations in nature, even at relatively high temperature. Although such studies are not routine, as methods become more efficient and measurements become more reproducible, both radiogenic and stable Ca isotope signatures will play important roles in tracking the petrological evolution of planetary to outcrop-scale processes in igneous and metamorphic rocks.

7.1. Carbonate recycling in the mantle

Over 50 years of sample measurements have shown that the mantle remains chemically and isotopically heterogeneous despite the fact that mantle convection has been active for most of Earth's history. Oceanic basalt studies employing radioactive isotope systems (*e.g.*, Sr, Nd, and Pb) have been used to identify compositionally distinct mantle reservoirs that reflect recent mixtures of different source components as well as the time integrated compositional history of ancient mantle reservoirs (*e.g.* Hawkesworth and Van Calsteren, 1984). Likewise, there are a number of geochemical and isotopic systems that have been used to suggest that recycled marine sediments are important in the petrogenesis of ocean island basalts (*e.g.* Blichert-Toft, 1999;

1215 Castillo et al., 2018; Dasgupta et al., 2004; Frey et al., 1994; Huang et al., 2009; Huang and Frey,
1216 2005; Lassiter and Hauri, 1998; Plank and Langmuir, 1998). The interconnection between
1217 recycled materials at subduction zones and more ancient mantle reservoirs remains elusive,
1218 however, and debates continue as to whether recycling at subduction zones is related to the
1219 isotopic heterogeneity in oceanic basalts.

1220 Ca isotopes potentially provide a powerful tool to test ideas about the various potential source(s)
1221 of mantle heterogeneity, in particular for recycling of Ca-rich marine sedimentary materials,
1222 because both radiogenic and stable Ca isotope variations yield complementary information.
1223 Significant stable mass-dependent Ca isotope variability is not generally expected to originate at
1224 mantle solidus temperatures under which oceanic basalts have been generated (>1200-1500°C,
1225 *e.g.* Putirka, 2005; Zhang et al., 2018). However, subduction and recycling of sediments,
1226 especially marine carbonates, could introduce distinctive Ca isotopic variations within the mantle
1227 because marine carbonates have high Ca concentrations with potentially light δ^{44}Ca, up to ~2‰
1228 lower than BSE (De La Rocha, 2000; DePaolo, 2004; Fantle and DePaolo, 2005; Farkaš et al.,
1229 2007; Griffith et al., 2008a; Heuser et al., 2005; Kasemann et al., 2005; Watkins et al., 2017; Zhu
1230 and Macdougall, 1998).

1231 To date, resolvable radiogenic Ca signatures have not been observed in oceanic basalts (Huang et
1232 al., 2011; Marshall and DePaolo, 1989; Simon et al., 2009). This might not be surprising given
1233 the work of Caro et al. (2010) who despite finding well-defined excesses of ^{40}Ca in some river
1234 waters draining into the ocean, report that no discernable effects of ^{40}K decay (within their
1235 reported analytical precision of ~0.4 epsilon units, 2σ) were seen in a number of marine
1236 carbonate samples ranging in age from Archean to recent. This led the authors to conclude that
1237 hydrothermal Ca has dominated the oceanic budget over all of Earth history. This conclusion is

at odds, however, with estimates of modern riverine *vs.* hydrothermal Ca fluxes (*e.g.* DePaolo, 2004) and with ε_{Ca} differences observed between modern seawater/carbonates and hydrothermal fluids/mafic igneous rocks (Antonelli et al., 2019a, 2018).

Stable mass-dependent Ca isotope signatures that correlate with other geochemical parameters (Sr/Nb and $^{87}Sr/^{86}Sr$, shown in Fig. 21) have been interpreted to represent recycling of ancient Ca bearing surface materials in Hawaiian lavas (*e.g.* Huang et al., 2011). Although the interpretation of the trends presented by Huang et al. (2011) is currently under debate due to the low $\delta^{44}Ca$ and $^{87}Sr/^{86}Sr$ values required for the carbonates, it has been reported that that the global ocean (and thus marine carbonates) may have gradually evolved through time towards higher $\delta^{44}Ca$ values (*e.g.* Farkaš et al., 2007).

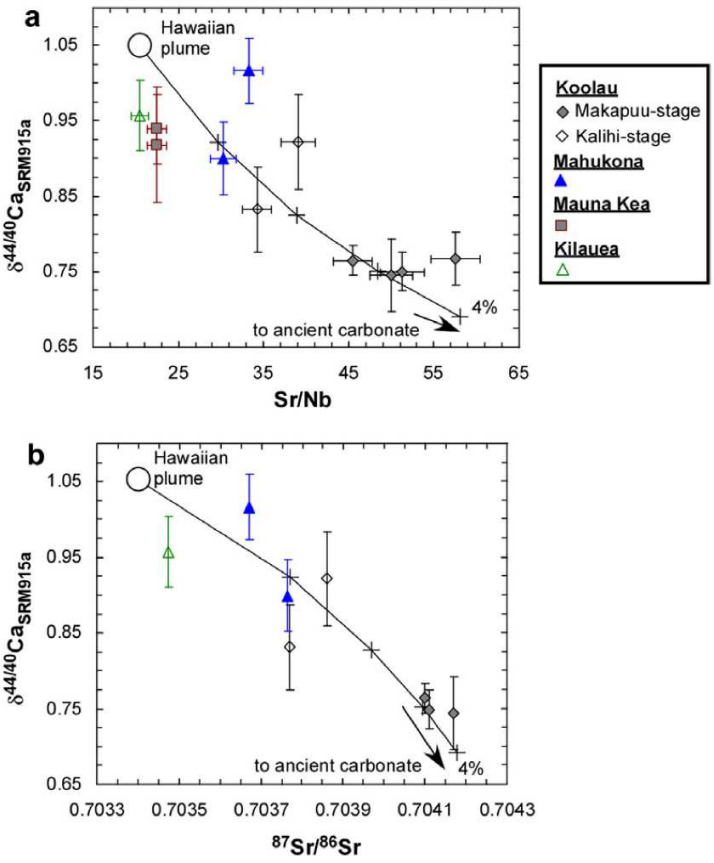

1249 **Fig. 21a,b.** Stable Ca isotope variations versus traditional proxies for carbonate incorporation in Hawaiian shield
1250 lavas after Huang et al. (2011). **(a)** δ^{44}Ca *vs*. Sr/Nb, **(b)** δ^{44}Ca *vs*. $^{87}Sr/^{86}Sr$. In this figure, Ca isotope ratios are
1251 reported relative to SRM915a (-0.95‰, relative to BSE), and the carbonate end-member component is assumed to
1252 have 800 ppm [Sr], 0 ppm [Nb], $^{87}Sr/^{86}Sr$ = 0.7034, [CaO] = 56 wt%, and $\delta^{44}Ca_{SRM915a}$ = 0.2‰ (-0.75‰ relative to
1253 BSE).

1254 However, the importance of both of these studies has been challenged more recently, in part,
1255 because marine carbonates deposited over the last ~2.5 Ga have average δ^{44}Ca that exhibit little
1256 change through time, with values similar to BSE (Blättler and Higgins, 2017). Likewise, it has
1257 been recently shown that carbonate metasomatism in the mantle has no discernable δ^{44}Ca effects
1258 (Ionov et al., 2019). More work like that of Huang et al. (2011), therefore, is needed to validate
1259 the influence of sediment recycling on the isotopic source compositions of igneous rocks. One
1260 possible reconciliation of these models and data could be that the marine carbonate records no
1261 longer accurately record their ancient (isotopically light) signatures because they have been reset
1262 more recently by exchange with bulk silicate mantle Ca reservoirs.

1263 **7.2. Crustal Contamination in Magmatic Systems**

1264 The Ca isotope ratio determinations of Russell et al. (1978) provide the basis for all current
1265 measurements. Established on sample measurements where radiogenic ^{40}Ca excesses are
1266 negligible, these values are used to represent the normal terrestrial composition at ca. 0.01%
1267 resolution. For radiogenic enrichment studies, Ca isotope variations are commonly reported as
1268 ε_{Ca} (Equation 5). Radioactive decay of ^{40}K within the continental crust can produce a Ca isotopic
1269 signature where ^{40}Ca excesses $\geq$ 0.5 epsilon units are distinguishable from mantle-like Ca isotope
1270 compositions, as shown in Mills et al. (2018). First employed in modern literature for igneous
1271 rocks by Marshall and DePaolo (1989, 1982), the K-Ca radiogenic isotope system has not been

applied to many petrogenetic studies primarily because of the difficulty in decoupling the radiogenic enrichments of ^{40}Ca from stable ^{40}Ca that makes up ~97% of terrestrial calcium.

Oceanic basalts largely have compositions and isotopic signatures that indicate derivation from partial melting of mantle sources. At levels that were near the analytical capabilities available at the time, however, Marshall and DePaolo (1989) showed the first evidence for crustal (^{40}Ca-enriched) calcium in some oceanic island arc magmas. The source components for more evolved magmas erupted through, or emplaced within, continental crust also remain debated. The petrogenic origin(s) of evolved magmas in the continental crust can be complicated because the relative importance of various petrogenetic processes, including magma mixing, fractional crystallization, and assimilation-fractional crystallization (*i.e.,* AFC), controlling magma differentiation can vary (DePaolo, 1981).

As with studies of crustal recycling discussed above, trace element radiogenic isotope systems have long been used to assess the petrogenesis of felsic magmas. Despite all that has been learned from trace element radiogenic studies, unresolved geologic problems remain. In fact, one of the most important and long-standing challenges is the ability to distinguish the contributions of mantle-derived sources in felsic magmas that are generated from preexisting continental crust [see Mills et al. (2018) and reference therein]. Although old continental crust and asthenospheric mantle sources can be readily distinguished with ε_{Nd} values, these authors showed that by combining radiogenic Nd and Ca isotope ratios, significant progress can be made. This is because whereas non-radiogenic Nd can be indicative of either old continental crust or lithospheric mantle, Ca isotopes can potentially distinguish between crustal (elevated ε_{Ca}) and lithospheric mantle (near zero ε_{Ca}) sources (Fig. 22).

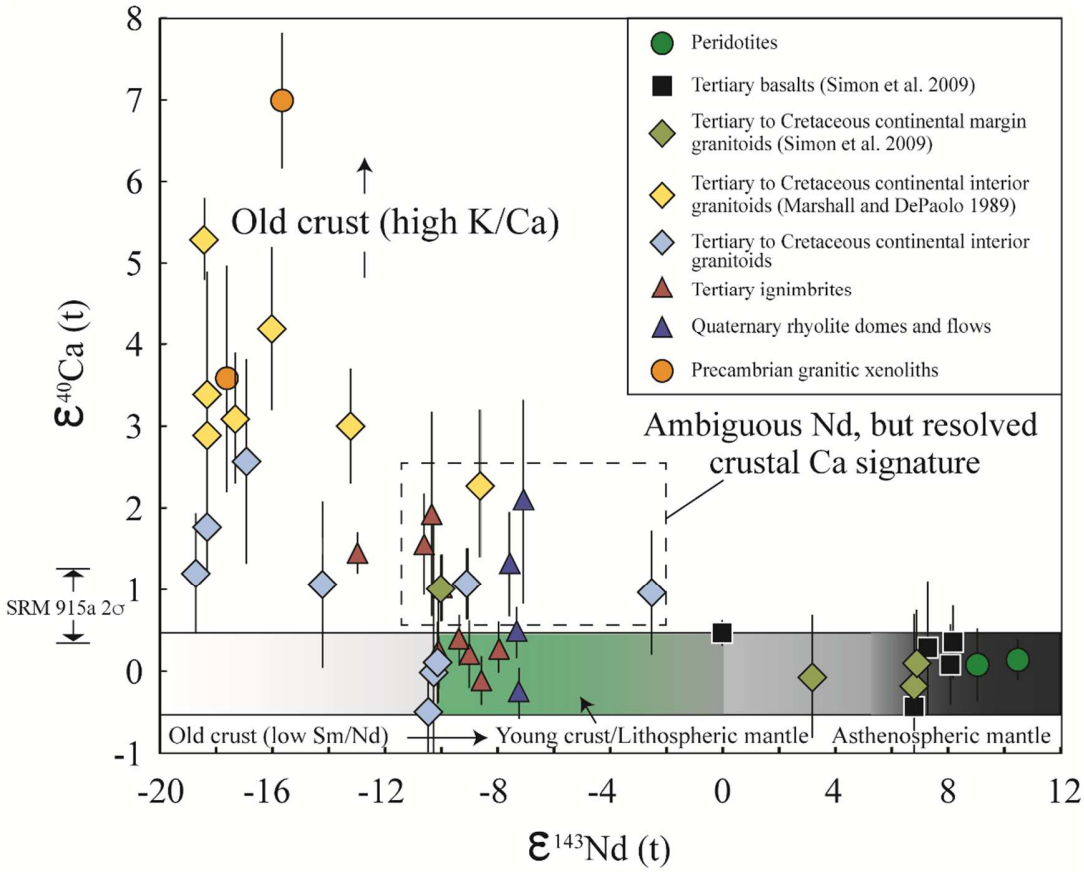

1294

1295 **Fig. 22.** Plot of age-corrected $\varepsilon^{143}Nd$ *vs.* $\varepsilon^{40}Ca$ showing the potential use of radiogenic Ca for discriminating
1296 between different mantle sources. The Data are from Mills et al. (2018) unless otherwise indicated in the legend.
1297 Epsilon values for Ca were calculated using the average $^{40}Ca/^{44}Ca$ value measured for peridotite and data from
1298 Simon et al. (2009) for oceanic basalts, which was used to define bulk silicate Earth. The SRM 915a value (shown
1299 on left axis) is ~1 ε-unit higher than bulk silicate Earth. Epsilon values for Nd were calculated using $^{143}Nd/^{144}Nd$
1300 (CHUR, 0 Ma) = 0.512638 and $^{147}Sm/^{144}Nd$ (CHUR, 0 Ma) = 0.1967.

1301 **7.3. Radiogenic Ca and K-loss in metamorphic systems**

1302 The loss of incompatible trace elements (*e.g.* U, Rb) during melting/dehydration of granulite-
1303 facies rocks is well documented (*e.g.* Rudnick et al., 1985; Rudnick and Gao, 2014). The
1304 resultant transfer of heat-producing elements from the lower-crust to the middle- and upper-crust
1305 is an essential aspect of many models for the creation of stable continents (through the coupling

of continental crust and lithospheric mantle, 'cratonization'). Given that ^{40}K was the largest source of radioactive heat on the early Earth, loss of potassium from the lower crust is especially important for cratonization, however, other than by comparison with similar systems (*e.g.* Rb/Sr, Rudnick et al., 1985) and direct measurements [in rare cases when the unmetamorphosed protoliths are still available (*e.g.* Ewing et al., 2014; Stepanov et al., 2014)], there have been no direct proxies for K-loss from these systems.

To address this issue, a recent study used radiogenic ^{40}Ca measurements (ε_{Ca}) in order to directly constrain K-loss during high-temperature granulite-facies metamorphism of the lower crust (Antonelli et al., 2019a). Analyzing $^{40}Ca/^{44}Ca$ in garnet separates from granulite-facies rocks, the authors found large enrichments in ε_{Ca} (up to +42) correlating inversely with garnet grossular percentage and positively with whole-rock peraluminosity index ('A/CNK', defined as molar $Al_2O_3/CaO + Na_2O + K_2O$, Fig. 23a,b). The large radiogenic ^{40}Ca enrichments must have occurred through decay of ^{40}K in protolith rocks, prior to garnet formation, as garnet is very effective at excluding K during crystallization.

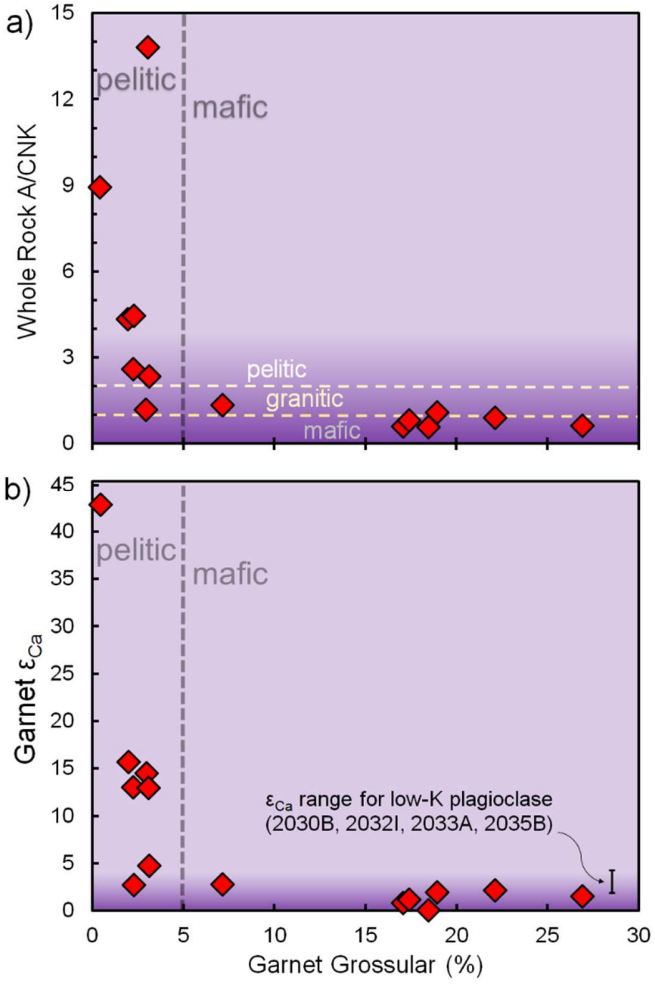

Fig. 23a,b. (a) Whole rock A/CNK, defined as molar $Al_2O_3/(CaO+Na_2O+K_2O)$ and **(b)** ε_{Ca} data for garnet separates from granulite-facies metamorphic rocks versus garnet grossular (%); after Antonelli et al. (2019a). Approximate compositional fields for various protoliths (based on A/CNK and garnet grossular) are demarcated with dashed lines. Garnet efficiently excludes K from its crystal structure, thus the measured ε_{Ca} values are the initial values at time of metamorphism. A bulk-silicate Earth $^{40}Ca/^{44}Ca$ value of 47.156 was used to calculate ε_{Ca}.

Using available protolith and metamorphic age estimates for the various localities, the authors placed constraints on the protolith K/Ca values necessary to generate initial ε_{Ca} recorded by garnet, assuming the oldest protolith ages from each locality in order to arrive at minimum protolith K/Ca estimates (as shown in Fig. 24). This figure also serves to demonstrate the relationship between estimated protolith K/Ca and uncertainties in associated protolith age

estimates, where an uncertainty of ±0.3 Ga gives K/Ca estimates consistent within a factor of ~2, even for ancient samples where radiogenic ingrowth of ^{40}Ca had the biggest effects.

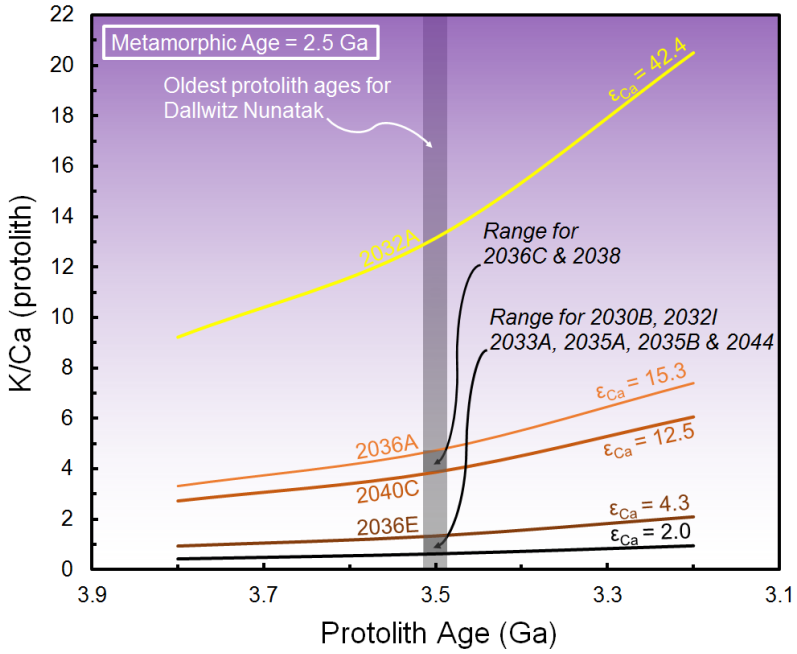

Fig. 24. Effect of protolith age uncertainty on estimated protolith K/Ca, after Antonelli et al. (2019a). The different lines represent garnet ε_{Ca} measurements from granulite-facies rocks from the Napier Complex, where the metamorphic age is ~2.5 Ga. Due to the very low compatibility of K in garnet, garnet is assumed to represent whole-rock ε_{Ca} at the time of metamorphism. Although protolith ages are not often constrained with great precision, this figure demonstrates the relatively minor effect that this has on estimated protolith K/Ca.

Comparing protolith estimates to K/Ca measured in the rocks today, minimum values for K loss (relative to Ca) during lower crustal metamorphism were constrained to ~67% to > 95% (Fig. 25a), confirming that K is effectively lost from the lower-crust during metamorphism. A non-modal batch melting model [*see SI text of Antonelli et al. (2019a) for details*] suggests that most samples represent 20-30% granitic melt-loss (Fig. 25b). These estimates are in good agreement with other estimates for melt-loss during granulite-facies metamorphism, (*e.g.* Yakymchuk and Brown, 2014), but further constraints on K and Ca partitioning during partial melting, along with

sample-specific protolith age estimates, would be greatly useful to further constrain K and melt loss in future studies.

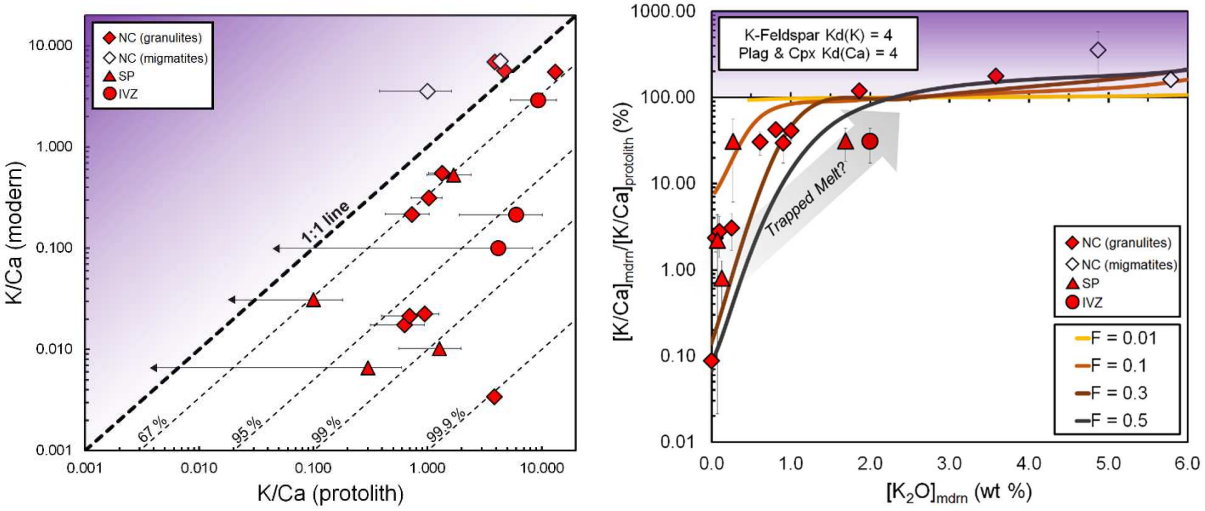

Fig. 25a,b. (a) K/Ca modern *vs.* K/Ca protolith estimates based on garnet ε_{Ca} and protolith/metamorphic ages, and **(b)** $(K/Ca)_{mdrn}/(K/Ca)_{protolith}$ *vs.* modern whole rock K_2O (wt%) with melt-loss estimates based on a non-modal batch melting model, after Antonelli et al. (2019a). Arrow shows the potential effects of incomplete melt loss.

8. Conclusions and future work

In this review, we have shown that stable Ca isotope fractionations at high-temperatures can equal and often exceed those that occur in low-temperature surface environments. To date, igneous and metamorphic whole-rock analyses have $\delta^{44}Ca$ ranges of ~2‰ and ~6‰, respectively, indicative of open-system processes such as fractional crystallization, partial-melt loss, metamorphism/metasomatism, and diffusive Ca transport. Despite this observation, non-metasomatized peridotites have little $\delta^{44}Ca$ variability and define a bulk-silicate Earth (BSE) value of +0.95‰ relative to standard SRM915a, while mid-ocean ridge basalts and average continental crust have slightly lower $\delta^{44}Ca$ (by ~0.1‰ and ~0.2‰, respectively). Basaltic standards analyzed by TIMS generally give values closer to BSE, but this may be due to a

1362 +0.1‰ difference in $\delta^{44}Ca$ compared to the same standards analyzed by ICP-MS (where ^{40}Ca is
1363 not directly measured). This suggests that there may be slight excess ^{40}Ca in SRM915a ($\varepsilon_{Ca} = +1$
1364 relative to basaltic igneous rocks), and that BSE has lower $^{40}Ca/^{44}Ca$ [~47.156 *vs.* ~47.162
1365 (Antonelli et al., 2019a)], but further exploration is required.

1366 Although there have been no experimental constraints for equilibrium fractionation factors
1367 between minerals, *ab-initio* simulations have provided great insight into equilibrium Ca isotope
1368 fractionation at high temperatures. General agreement is reached between the various studies in
1369 spite of their different theoretical approaches. Likewise, the existing measurements of
1370 equilibrium slopes in triple Ca isotope space ($^{48}Ca/^{44}Ca$ *vs.* $^{42}Ca/^{44}Ca$) for samples that agree
1371 with *ab-initio* estimates, suggest that they are approximately correct. Thus, there is potential for
1372 using inter-mineral $\Delta^{44}Ca$ measurements for future geothermometry, especially in non-
1373 metasomatized plutonic rocks where minerals tend to have compositions closer to predicted
1374 equilibrium. For the moment, however, relatively common observations of inter-mineral
1375 disequilibrium preclude the use of Ca isotopes for geothermometry, and additional constraints
1376 (*e.g.* independent temperature estimates combined with *ab-initio* predictions, and/or $\Delta^{48}Ca$'
1377 measurements) are necessary in order to further understand the geologic environments in which
1378 isotopic equilibrium can be expected.

1379 The large $\Delta^{44}Ca$ fractionations observed between adjacent whole rocks (which can exceed 3‰)
1380 and between coexisting minerals (which can exceed 2‰) have slopes in triple Ca isotope space
1381 that agree with the predicted kinetic mass-fractionation law (based on Graham's law), suggesting
1382 that they are the result of Ca diffusion. Although modeling disequilibrium isotope fractionation
1383 can be more complicated than modeling equilibrium fractionation, Ca isotope diffusion models
1384 have been applied to natural samples and yield important information on (i) the timescales of

1385 mantle metasomatism, (ii) Ca transport mechanisms during lower crustal metamorphism, (iii)
1386 metamorphic mineral paragenesis, (iv) crystal growth rates in volcanic and sub-volcanic rocks,
1387 and (v) mineral precipitation rates in hydrothermal systems.

1388 Radiogenic ^{40}Ca variations (ε_{Ca}) are especially useful for source-tracing studies, as they are not
1389 complicated by the numerous stable isotope effects mentioned above. In rocks with known
1390 protolith and metamorphic ages, ε_{Ca} measurements can be used to estimate initial K/Ca values
1391 and constrain K-loss (and potentially K-gains) during metamorphism. Studies have also shown
1392 that ε_{Ca} can be used as a proxy for crustal contamination in mantle-derived continental magmas
1393 and (in combination with ε_{Nd}) to differentiate between lithospheric and asthenospheric mantle
1394 sources.

1395 The ε_{Ca} differences between (modern) carbonates and mantle, however, are not large enough to
1396 trace potential contributions from carbonate subduction in igneous samples. Although there is
1397 potential for using stable Ca isotopes for this purpose (due to low $\delta^{44}Ca$ values in rapidly-
1398 precipitated carbonates), this idea has recently been challenged by studies concluding that, on
1399 average, carbonates have the same $\delta^{44}Ca$ as BSE over the last several billion years, and that
1400 carbonatite metasomatism has no measurable effects in mantle samples. Thus, further studies are
1401 necessary in order to better constrain the situations in which $\delta^{44}Ca$ can be used as a tracer of
1402 carbonate subduction.

1403 In order to further advance our understanding of Ca isotope fractionations during high-
1404 temperature processes, future studies of natural samples should pay special attention to: (i)
1405 kinetic *vs.* equilibrium signatures (*e.g.* by using $\Delta^{48}Ca$' measurements or independent
1406 temperature constraints combined with *ab-initio* estimates), (ii) spatial constraints and field
1407 relationships suggestive of initial chemical/temperature gradients or open-system processes, and

(iii) detailed petrographic observations (including textural and paragenetic relationships). A greater number of experimental constraints, including inter-mineral equilibration (to verify fractionation factors), crystallization, melting, hydrothermal mineral precipitation, and diffusion-couple experiments would also be greatly beneficial. Finally, technical advancements such as (i) improved sampling (*e.g.* micro-drilling across mineral-zones or separation of specific crystal populations) and small sample analysis methods (*e.g.* TIMS analyses using next generation high-resistance amplifiers) and (ii) the development of in-situ Ca isotope analysis techniques (*e.g.* by SIMS or LA-MC-ICP-MS), would greatly enhance our understanding of the various processes leading to Ca isotope equilibrium and disequilibrium in high-temperature samples. Next generation CC-MC-ICP-MS instruments with low energy collision-cell technology should also allow ^{40}Ca, ^{42}Ca, ^{44}Ca, and ^{48}Ca to be measured without isobaric interferences from Ar-based polyatomic species (Simon, 2019; Zhao and Simon, 2019), which will be especially useful for determining Ca isotope variations (including ε_{Ca}, δ^{44}Ca, and Δ^{48}Ca') in future studies.

9. Acknowledgments

M.A.A. would like to thank E.M. Nordquist and S.T. Brown for their help with data compilation. We also thank S. Huang and two anonymous reviewers for their beneficial comments and suggestions. This contribution was partially supported by an ETH Zurich post-doctoral fellowship (19-2 FEL-33) to M.A.A. and by NASA grants (11-COS11-0066, 16-EW16_2-0163, and the NASA Planetary Science Division) to J.I.S.

References

Amini, M., Eisenhauer, A., Böhm, F., Fietzke, J., Bach, W., Garbe-Schönberg, D., Rosner, M., Bock, B., Lackschewitz, K.S., Hauff, F., 2008. Calcium isotope (δ44/40Ca) fractionation along hydrothermal pathways, Logatchev field (Mid-Atlantic Ridge, 14 45 N). Geochim. Cosmochim. Acta 72, 4107–4122. https://doi.org/10.1016/j.gca.2008.05.055

Amini, M., Eisenhauer, A., Böhm, F., Holmden, C., Kreissig, K., Hauff, F., Jochum, K.P., 2009. Calcium isotopes (d44/40Ca) in MPI-DING reference glasses, USGS rock powders and various rocks: Evidence for Ca isotope fractionation in terrestrial silicates. Geostand. Geoanalytical Res. 33, 231–247. https://doi.org/10.1111/j.1751-908X.2009.00903.x

Amsellem, E., Moynier, F., Pringle, E.A., Bouvier, A., Chen, H., Day, J.M.D.D., 2017. Testing the chondrule-rich accretion model for planetary embryos using calcium isotopes. Earth Planet. Sci. Lett. 469, 75–83. https://doi.org/10.1016/j.epsl.2017.04.022

Amsellem, E., Moynier, F., Puchtel, I.S., 2019. Evolution of the Ca isotopic composition of the mantle. Geochim. Cosmochim. Acta 258, 195–206. https://doi.org/10.1016/j.gca.2019.05.026

Antonelli, M.A., Depaolo, D.J., Brown, S.T., Pester, N.J., 2018. Radiogenic 40Ca in Seawater, in: Goldschmidt Conference 2018, Boston, MA.

Antonelli, M.A., DePaolo, D.J., Chacko, T., Grew, E.S., Rubatto, D., 2019a. Radiogenic Ca isotopes confirm post-formation K depletion of lower crust. Geochemical Perspect. Lett. 9, 43–48. https://doi.org/10.7185/geochemlet.1904

Antonelli, M.A., Mittal, T., McCarthy, A., Tripoli, B., Watkins, J.M., DePaolo, D.J., 2019b. Ca isotopes record rapid crystal growth in volcanic and subvolcanic systems. Proc. Natl. Acad. Sci. 201908921. https://doi.org/10.1073/pnas.1908921116

Antonelli, M.A., Pester, N.J., Brown, S.T., DePaolo, D.J., 2017. Effect of paleoseawater composition on hydrothermal exchange in midocean ridges. Proc. Natl. Acad. Sci. 114, 201709145. https://doi.org/10.1073/pnas.1709145114

Antonelli, M.A., Schiller, M., Schauble, E.A., Mittal, T., DePaolo, D.J., Chacko, T., Grew, E.S., Tripoli, B., 2019c. Kinetic and equilibrium Ca isotope effects in high-T rocks and minerals. Earth Planet. Sci. Lett. 517, 71–82. https://doi.org/10.1016/j.epsl.2019.04.013

Arzilli, F., Mancini, L., Voltolini, M., Cicconi, M.R., Mohammadi, S., Giuli, G., Mainprice, D., Paris, E., Barou, F., Carroll, M.R., 2015. Near-liquidus growth of feldspar spherulites in trachytic melts: 3D morphologies and implications in crystallization mechanisms. Lithos 216–217, 93–105. https://doi.org/10.1016/j.lithos.2014.12.003

Baker, D.R., 1989. Tracer versus trace element diffusion: Diffusional decoupling of Sr concentration from Sr isotope composition. Geochim. Cosmochim. Acta 53, 3015–3023. https://doi.org/10.1016/0016-7037(89)90177-4

Banerjee, A., Chakrabarti, R., 2019. A geochemical and Nd, Sr and stable Ca isotopic study of carbonatites and associated silicate rocks from the ~65 Ma old Ambadongar carbonatite complex and the Phenai Mata igneous complex, Gujarat, India. LITHOS 326–327. https://doi.org/10.1016/j.lithos.2019.01.007

Banerjee, A., Chakrabarti, R., 2018. Large Ca stable isotopic (δ44/40Ca) variation in a hand-specimen sized spheroidally weathered diabase due to selective weathering of clinopyroxene and plagioclase. Chem. Geol. 483, 295–303. https://doi.org/10.1016/j.chemgeo.2018.02.031

Bessey, C., 2018. Calcium Isotope Fractionation in Coexisting Minerals. BSc Thesis, University of Waterloo.

1471 Bigeleisen, J., Mayer, M.G., 1947. Calculation of Equilibrium Constants for Isotopic Exchange
1472 Reactions. J. Chem. Phys. 15, 261–267. https://doi.org/10.1063/1.1746492

1473 Blättler, C.L., Higgins, J.A., 2017. Testing Urey's carbonate–silicate cycle using the calcium isotopic
1474 composition of sedimentary carbonates. Earth Planet. Sci. Lett. 479, 241–251.
1475 https://doi.org/10.1016/j.epsl.2017.09.033

1476 Blichert-Toft, J., 1999. Hf Isotope Evidence for Pelagic Sediments in the Source of Hawaiian Basalts.
1477 Science (80-.). 285, 879–882. https://doi.org/10.1126/science.285.5429.879

1478 Brey, G.P., Kohler, T., 1990. Geothermobarometry in 4-phase lherzolites .2. New thermobarometers, and
1479 practical assessment of existing thermobarometers. J. Petrol. 31, 1353–1378.

1480 Brown, S.T., Kennedy, B.M., DePaolo, D.J., Hurwitz, S., Evans, W.C., 2013. Ca, Sr, O and D isotope
1481 approach to defining the chemical evolution of hydrothermal fluids: Example from Long Valley,
1482 CA, USA. Geochim. Cosmochim. Acta 122, 209–225.

1483 Brown, S.T., Turchyn, A. V., Bickle, M.J., Davis, A.C., Alt, J.C., Bédard, J.H., Skulski, T., Bedard, J.H.,
1484 Skulski, T., DePaolo, D.J., 2020. High-temperature kinetic isotope fractionation of calcium in
1485 epidosites from modern and ancient seafloor hydrothermal systems. Earth Planet. Sci. Lett. 535.
1486 https://doi.org/10.1016/j.epsl.2020.116101

1487 Brugger, C.R., Hammer, J.E., 2010. Crystal size distribution analysis of plagioclase in experimentally
1488 decompressed hydrous rhyodacite magma. Earth Planet. Sci. Lett. 300, 246–254.
1489 https://doi.org/10.1016/j.epsl.2010.09.046

1490 Caro, G., Papanastassiou, D. a., Wasserburg, G.J., 2010. 40K-40Ca isotopic constraints on the oceanic
1491 calcium cycle. Earth Planet. Sci. Lett. 296, 124–132. https://doi.org/10.1016/j.epsl.2010.05.001

1492 Castillo, P.R., MacIsaac, C., Perry, S., Veizer, J., 2018. Marine Carbonates in the Mantle Source of
1493 Oceanic Basalts: Pb Isotopic Constraints. Sci. Rep. 8, 14932. https://doi.org/10.1038/s41598-018-
1494 33178-4

1495 Chacko, T., Cole, D.R., Horita, J., 2001. Equilibrium Oxygen, Hydrogen and Carbon Isotope
1496 Fractionation Factors Applicable to Geologic Systems. Rev. Mineral. Geochemistry 43, 1–81.
1497 https://doi.org/10.2138/gsrmg.43.1.1

1498 Chakrabarti, R., Acharya, S.S., Mondal, S., 2018. Large stable Ca isotopic (δ44/40 Ca) variation in open
1499 ocean samples from the Bay of Bengal, in: Goldschmidt 2018.

1500 Chen, C., Ciazela, J., Li, W., Dai, W., Wang, Z., Foley, S.F., Li, M., Hu, Z., Liu, Y., 2019a. Calcium
1501 isotopic compositions of oceanic crust at various spreading rates. Geochim. Cosmochim. Acta.
1502 https://doi.org/10.1016/j.gca.2019.07.008

1503 Chen, C., Dai, W., Wang, Z., Liu, Y., Li, M., Becker, H., Foley, S.F., 2019b. Calcium isotope
1504 fractionation during magmatic processes in the upper mantle. Geochim. Cosmochim. Acta 249,
1505 121–137. https://doi.org/10.1016/j.gca.2019.01.031

1506 Chen, C., Liu, Y., Feng, L., Foley, S.F., Zhou, L., Ducea, M.N., Hu, Z., 2018. Calcium isotope evidence
1507 for subduction-enriched lithospheric mantle under the northern North China Craton. Geochim.
1508 Cosmochim. Acta 238, 55–67. https://doi.org/10.1016/j.gca.2018.06.038

1509 Clayton, R.N., 1959. Oxygen Isotope Fractionation in the System Calcium Carbonate-Water. J. Chem.
1510 Phys. 30, 1246–1250. https://doi.org/10.1063/1.1730165

1511 Colla, C.A., Wimpenny, J., Yin, Q.Z., Rustad, J.R., Casey, W.H., 2013. Calcium-isotope fractionation
1512 between solution and solids with six, seven or eight oxygens bound to Ca(II). Geochim.
1513 Cosmochim. Acta 121, 363–373. https://doi.org/10.1016/j.gca.2013.07.041

1514 Cooper, K.M., 2019. Time scales and temperatures of crystal storage in magma reservoirs: implications
1515 for magma reservoir dynamics. Philos. Trans. R. Soc. A Math. Phys. Eng. Sci. 377, 20180009.
1516 https://doi.org/10.1098/rsta.2018.0009

1517 Cooper, K.M., Kent, A.J.R., 2014. Rapid remobilization of magmatic crystals kept in cold storage. Nature
1518 506, 480–483. https://doi.org/10.1038/nature12991

1519 Coplen, T.B., 2011. Guidelines and recommended terms for expression of stable-isotope-ratio and gas-
1520 ratio measurement results. Rapid Commun. Mass Spectrom. 25, 2538–2560.
1521 https://doi.org/10.1002/rcm.5129

1522 Dai, W., Wang, Z., Liu, Y., Chen, C., Zong, K., Zhou, L., Zhang, G., Li, M., Moynier, F., Hu, Z., 2020.
1523 Calcium isotope compositions of mantle pyroxenites. Geochim. Cosmochim. Acta 270, 144–159.
1524 https://doi.org/10.1016/j.gca.2019.11.024

1525 Dasgupta, R., Hirschmann, M.M., Withers, A.C., 2004. Deep global cycling of carbon constrained by the
1526 solidus of anhydrous, carbonated eclogite under upper mantle conditions. Earth Planet. Sci. Lett.
1527 227, 73–85. https://doi.org/10.1016/j.epsl.2004.08.004

1528 Dauphas, N., Roskosz, M., Alp, E.E., Golden, D.C., Sio, C.K., Tissot, F.L.H., Hu, M.Y., Zhao, J., Gao,
1529 L., Morris, R. V., 2012. A general moment NRIXS approach to the determination of equilibrium Fe
1530 isotopic fractionation factors: Application to goethite and jarosite. Geochim. Cosmochim. Acta 94,
1531 254–275. https://doi.org/10.1016/j.gca.2012.06.013

1532 De La Rocha, C.L., 2000. Isotopic Evidence for Variations in the Marine Calcium Cycle Over the
1533 Cenozoic. Science (80-.). 289, 1176–1178. https://doi.org/10.1126/science.289.5482.1176

1534 DePaolo, D.J., 2011. Surface kinetic model for isotopic and trace element fractionation during
1535 precipitation of calcite from aqueous solutions. Geochim. Cosmochim. Acta 75, 1039–1056.
1536 https://doi.org/10.1016/j.gca.2010.11.020

1537 DePaolo, D.J., 2004. Calcium Isotopic Variations Produced by Biological, Kinetic, Radiogenic and
1538 Nucleosynthetic Processes. Rev. Mineral. Geochemistry 55, 255–288.
1539 https://doi.org/10.2138/gsrmg.55.1.255

1540 DePaolo, D.J., 1981. Trace element and isotopic effects of combined wallrock assimilation and fractional
1541 crystallization. Earth Planet. Sci. Lett. 53, 189–202. https://doi.org/10.1016/0012-821X(81)90153-9

1542 DePaolo, D.J., Wasserburg, G.J., 1979. Sm-Nd age of the Stillwater complex and the mantle evolution
1543 curve for neodymium. Geochim. Cosmochim. Acta 43, 999–1008. https://doi.org/10.1016/0016-
1544 7037(79)90089-9

1545 Dohmen, R., Milke, R., 2010. Diffusion in Polycrystalline Materials: Grain Boundaries, Mathematical
1546 Models, and Experimental Data. Rev. Mineral. Geochemistry 72, 921–970.
1547 https://doi.org/10.2138/rmg.2010.72.21

1548 Dominguez, G., Wilkins, G., Thiemens, M.H., 2011. The Soret effect and isotopic fractionation in high-
1549 temperature silicate melts. Nature 473, 70–73. https://doi.org/10.1038/nature09911

1550 Ewing, T.A., Rubatto, D., Hermann, J., 2014. Hafnium isotopes and Zr/Hf of rutile and zircon from lower
1551 crustal metapelites (Ivrea-Verbano Zone, Italy): Implications for chemical differentiation of the
1552 crust. Earth Planet. Sci. Lett. 389, 106–118. https://doi.org/10.1016/j.epsl.2013.12.029

1553 Fantle, M.S., DePaolo, D.J., 2005. Variations in the marine Ca cycle over the past 20 million years. Earth
1554 Planet. Sci. Lett. 237, 102–117. https://doi.org/10.1016/j.epsl.2005.06.024

1555 Fantle, M.S., Tipper, E.T., 2014. Calcium isotopes in the global biogeochemical Ca cycle: Implications
1556 for development of a Ca isotope proxy. Earth-Science Rev. 129, 148–177.
1557 https://doi.org/10.1016/j.earscirev.2013.10.004

1558 Farkaš, J., Buhl, D., Blenkinsop, J., Veizer, J., 2007. Evolution of the oceanic calcium cycle during the
1559 late Mesozoic: Evidence from δ44/40Ca of marine skeletal carbonates. Earth Planet. Sci. Lett. 253,
1560 96–111. https://doi.org/10.1016/j.epsl.2006.10.015

1561 Farver, J.R., Yund, R.A., 1995. Grain-Boundary Diffusion of Oxygen, Potassium and Calcium in Natural
1562 and Hot-Pressed Feldspar Aggregates. Contrib. to Mineral. Petrol. 118, 340–355.
1563 https://doi.org/10.1007/s004100050019

1564 Feng, C., Qin, T., Huang, S., Wu, Z., Huang, F., 2014. First-principles investigations of equilibrium
1565 calcium isotope fractionation between clinopyroxene and Ca-doped orthopyroxene. Geochim.
1566 Cosmochim. Acta 143, 132–142. https://doi.org/10.1016/j.gca.2014.06.002

1567 Feng, L., Zhou, L., Yang, L., DePaolo, D.J., Tong, S.-Y., Liu, Y.-S., Owens, T.L., Gao, S., 2016. Calcium
1568 Isotopic Compositions of Sixteen USGS Reference Materials. Geostand. Geoanalytical Res. 41, 93–
1569 106. https://doi.org/10.1111/ggr.12131

1570 Feng, L., Zhou, L., Yang, L., Zhang, W., Wang, Q., Shuoyun, T., Hu, Z., 2018. A rapid and simple
1571 single-stage method for Ca separation from geological and biological samples for isotopic analysis
1572 by MC-ICP-MS. J. Anal. At. Spectrom. 33, 413–421. https://doi.org/10.1039/c7ja00370f

1573 Frey, F.., Garcia, M.., Roden, M.., 1994. Geochemical characteristics of Koolau Volcano: Implications of
1574 intershield geochemical differences among Hawaiian volcanoes. Geochim. Cosmochim. Acta 58,
1575 1441–1462. https://doi.org/10.1016/0016-7037(94)90548-7

1576 Giletti, B.J., 1994. Isotopic Equilibrium/Disequilibrium and Diffusion Kinetics in Feldspars, in: Parsons,
1577 I. (Ed.), Feldspars and Their Reactions. Springer Netherlands, Dordrecht, pp. 351–382.
1578 https://doi.org/10.1007/978-94-011-1106-5_9

1579 Griffith, E.M., Paytan, A., Caldeira, K., Bullen, T.D., Thomas, E., 2008a. A Dynamic Marine Calcium
1580 Cycle During the Past 28 Million Years. Science (80-.). 322, 1671–1674.
1581 https://doi.org/10.1126/science.1163614

1582 Griffith, E.M., Schauble, E.A., Bullen, T.D., Paytan, A., 2008b. Characterization of calcium isotopes in
1583 natural and synthetic barite. Geochim. Cosmochim. Acta 72, 5641–5658.
1584 https://doi.org/10.1016/j.gca.2008.08.010

1585 Hawkesworth, C.J., Van Calsteren, P.W.C., 1984. Radiogenic Isotopes – Some Geological Applications.
1586 pp. 375–421. https://doi.org/10.1016/B978-0-444-42148-7.50016-2

1587 He, Y., Wang, Y., Zhu, C., Huang, S., Li, S., 2017. Mass-Independent and Mass-Dependent Ca Isotopic
1588 Compositions of Thirteen Geological Reference Materials Measured by Thermal Ionisation Mass
1589 Spectrometry. Geostand. Geoanalytical Res. 41, 283–302. https://doi.org/10.1111/ggr.12153

1590 Heuser, A., Eisenhauer, A., Böhm, F., Wallmann, K., Gussone, N., Pearson, P.N., Nägler, T.F., Dullo,
1591 W.-C., 2005. Calcium isotope (δ 44/40 Ca) variations of Neogene planktonic foraminifera.
1592 Paleoceanography 20, n/a-n/a. https://doi.org/10.1029/2004PA001048

1593 Holmden, C., Bélanger, N., 2010. Ca isotope cycling in a forested ecosystem. Geochim. Cosmochim.
1594 Acta 74, 995–1015. https://doi.org/10.1016/j.gca.2009.10.020

1595 Holycross, M.E., Watson, E.B., Richter, F.M., Villeneuve, J., 2018. Diffusive fractionation of Li isotopes
1596 in wet, silicic melts. Geochemical Perspect. Lett. 39–42. https://doi.org/10.7185/geochemlet.1807

1597 Huang, F., Chakraborty, P., Lundstrom, C.C.C., Holmden, C.E., Glessner, J.J.G.J.G., Kieffer, S.W.,
1598 Lesher, C.E.E., 2010. Isotope fractionation in silicate melts by thermal diffusion. Nature 464, 396–
1599 400. https://doi.org/10.1038/nature08840

1600 Huang, F., Zhou, C., Wang, W., Kang, J., Wu, Z., 2019. First-principles calculations of equilibrium Ca
1601 isotope fractionation : Implications for oldhamite formation and evolution of lunar magma ocean.

Earth Planet. Sci. Lett. 510, 153–160. https://doi.org/10.1016/j.epsl.2018.12.034

Huang, S., Abouchami, W., Blichert-Toft, J., Clague, D.A., Cousens, B.L., Frey, F.A., Humayun, M., 2009. Ancient carbonate sedimentary signature in the Hawaiian plume: Evidence from Mahukona volcano, Hawaii. Geochemistry, Geophys. Geosystems 10, n/a-n/a. https://doi.org/10.1029/2009GC002418

Huang, S., Farkaš, J., Jacobsen, S.B., 2011. Stable calcium isotopic compositions of Hawaiian shield lavas: Evidence for recycling of ancient marine carbonates into the mantle. Geochim. Cosmochim. Acta 75, 4987–4997. https://doi.org/10.1016/j.gca.2011.06.010

Huang, S., Farkaš, J., Jacobsen, S.B., 2010. Calcium isotopic fractionation between clinopyroxene and orthopyroxene from mantle peridotites. Earth Planet. Sci. Lett. 292, 337–344. https://doi.org/10.1016/j.epsl.2010.01.042

Huang, S., Frey, F.A., 2005. Recycled oceanic crust in the Hawaiian Plume: evidence from temporal geochemical variations within the Koolau Shield. Contrib. to Mineral. Petrol. 149, 556–575. https://doi.org/10.1007/s00410-005-0664-9

Ionov, D.A., Qi, Y.-H., Kang, J.-T., Golovin, A. V., Oleinikov, O.B., Zheng, W., Anbar, A.D., Zhang, Z.-F., Huang, F., 2019. Calcium isotopic signatures of carbonatite and silicate metasomatism, melt percolation and crustal recycling in the lithospheric mantle. Geochim. Cosmochim. Acta 248, 1–13. https://doi.org/10.1016/j.gca.2018.12.023

Jacobson, A.D., Grace Andrews, M., Lehn, G.O., Holmden, C., 2015. Silicate versus carbonate weathering in Iceland: New insights from Ca isotopes. Earth Planet. Sci. Lett. 416, 132–142. https://doi.org/10.1016/j.epsl.2015.01.030

Jochum, K.P., Stoll, B., Herwig, K., Willbold, M., Hofmiann, A.W., Amini, M., Aarburg, S., Abouchami, W., Hellebrand, E., Mocek, B., Raczek, I., Stracke, A., Alard, O., Bouman, C., Becker, S., Dücking, M., Brätz, H., Klemd, R., De Bruin, D., Canil, D., Cornell, D., De Hoog, C.J., Dalpé, C., Danyushevshy, L., Eisenhauer, A., Gao, Y., Snow, J.E., Groschopf, N., Günther, D., Latkoczy, C., Guillong, M., Hauri, E.H., Höfer, H.E., Lahaye, Y., Horz, K., Jacob, D.E., Kasemann, S.A., Kent, A.J.R., Ludwig, T., Zack, T., Mason, P.R.D., Meixner, A., Rosner, M., Misawa, K., Nash, B.P., Pfänder, J., Premo, W.R., Sun, W.D., Tiepolo, M., Vannucci, R., Vennemann, T., Wayne, D., Woodhead, J.D., 2006. MPI-DING reference glasses for in situ microanalysis: New reference values for element concentrations and isotope ratios. Geochemistry, Geophys. Geosystems 7. https://doi.org/10.1029/2005GC001060

John, T., Gussone, N., Podladchikov, Y.Y., Bebout, G.E., Dohmen, R., Halama, R., Klemd, R., Magna, T., Seitz, H.M., 2012. Volcanic arcs fed by rapid pulsed fluid flow through subducting slabs. Nat. Geosci. 5, 489–492. https://doi.org/10.1038/ngeo1482

Kaercher, P., Militzer, B., Wenk, H.-R., 2014. Ab initio Calculations of Elastic Constants of Plagioclase feldespars. Am. Mineral. 99, 2344–2352. https://doi.org/10.2138/am-2014-4796

Kang, J.-T.T., Ionov, D.A., Zhu, H.-L.L., Liu, F., Zhang, Z.-F.F., Liu, Z., Huang, F., 2019. Calcium isotope sources and fractionation during melt-rock interaction in the lithospheric mantle: Evidence from pyroxenites, wehrlites, and eclogites. Chem. Geol. 524, 272–282. https://doi.org/10.1016/j.chemgeo.2019.06.010

Kang, J.T., Ionov, D.A., Liu, F., Zhang, C.L., Golovin, A. V., Qin, L.P., Zhang, Z.F., Huang, F., 2017. Calcium isotopic fractionation in mantle peridotites by melting and metasomatism and Ca isotope composition of the Bulk Silicate Earth. Earth Planet. Sci. Lett. 474, 128–137. https://doi.org/10.1016/j.epsl.2017.05.035

Kang, J.T., Zhu, H.L., Liu, Y.F., Liu, F., Wu, F., Hao, Y.T., Zhi, X.C., Zhang, Z.F., Huang, F., 2016.

Calcium isotopic composition of mantle xenoliths and minerals from Eastern China. Geochim. Cosmochim. Acta 174, 335–344. https://doi.org/10.1016/j.gca.2015.11.039

Kasemann, S.A., Hawkesworth, C.J., Prave, A.R., Fallick, A.E., Pearson, P.N., 2005. Boron and calcium isotope composition in Neoproterozoic carbonate rocks from Namibia: evidence for extreme environmental change. Earth Planet. Sci. Lett. 231, 73–86. https://doi.org/10.1016/j.epsl.2004.12.006

Keller, L.M., Wirth, R., Rhede, D., Kunze, K., Abart, R., 2008. Asymmetrically zoned reaction rims: Assessment of grain boundary diffusivities and growth rates related to natural diffusion-controlled mineral reactions. J. Metamorph. Geol. 26, 99–120. https://doi.org/10.1111/j.1525-1314.2007.00747.x

Kueter, N., Lilley, M.D., Schmidt, M.W., Bernasconi, S.M., 2019. Experimental carbonatite/graphite carbon isotope fractionation and carbonate/graphite geothermometry. Geochim. Cosmochim. Acta 253, 290–306. https://doi.org/10.1016/j.gca.2019.03.020

Laan, S. Van Der, Zhang, Y., Kennedy, A.K., Wyllie, P.J., 1994. Comparison of element and isotope diffusion of K and Ca in multicomponent silicate melts. Earth Planet. Sci. Lett. 123, 155–166.

Lassiter, J.C., Hauri, E.H., 1998. Osmium-isotope variations in Hawaiian lavas: evidence for recycled oceanic lithosphere in the Hawaiian plume. Earth Planet. Sci. Lett. 164, 483–496. https://doi.org/10.1016/S0012-821X(98)00240-4

Lehn, G.O., Jacobson, A.D., 2015. Optimization of a 48Ca–43Ca double-spike MC-TIMS method for measuring Ca isotope ratios (δ44/40Ca and δ44/42Ca): limitations from filament reservoir mixing. J. Anal. At. Spectrom. 30, 1571–1581. https://doi.org/10.1039/C4JA00412D

Lesher, C.E., 1994. Kinetics of Sr and Nd exchange in silicate liquids: theory, experiments, and applications to uphill diffusion, isotopic equilibration, and irreversible mixing of magmas. J. Geophys. Res. 99, 9585–9604. https://doi.org/10.1029/94JB00469

Lesher, C.E., 1990. Decoupling of chemical and isotopic exchange during magma mixing. Nature. https://doi.org/10.1038/344235a0

Liu, F., Li, X., Wang, G., Liu, Y., Zhu, H., Kang, J., Huang, F., Sun, W., Xia, X., Zhang, Z., 2017a. Marine Carbonate Component in the Mantle Beneath the Southeastern Tibetan Plateau: Evidence From Magnesium and Calcium Isotopes. J. Geophys. Res. Solid Earth 122, 9729–9744. https://doi.org/10.1002/2017JB014206

Liu, F., Zhu, H.L., Li, X., Wang, G.Q., Zhang, Z.F., 2017b. Calcium Isotopic Fractionation and Compositions of Geochemical Reference Materials. Geostand. Geoanalytical Res. 41, 675–688. https://doi.org/10.1111/ggr.12172

Lowenstein, T.K., Kendall, B., Anbar, a. D., 2013. The Geologic History of Seawater, 2nd ed, Treatise on Geochemistry: Second Edition. Elsevier Ltd. https://doi.org/10.1016/B978-0-08-095975-7.00621-5

Lu, F., Anderson, A.T., Davis, A.M., 1995. Diffusional Gradients at the Crystal / Melt Interface and Their Effect on the Compositions of Melt Inclusions. J. Geol. 103, 591–597.

Lu, W.-N., He, Y., Wang, Y., Ke, S., 2019. Behavior of calcium isotopes during continental subduction recorded in meta-basaltic rocks. Geochim. Cosmochim. Acta. https://doi.org/10.1016/j.gca.2019.09.027

Magna, T., Gussone, N., Mezger, K., 2015. The calcium isotope systematics of Mars. Earth Planet. Sci. Lett. 430, 86–94. https://doi.org/10.1016/j.epsl.2015.08.016

Marshall, B.D., DePaolo, D.J., 1989. Calcium isotopes in igneous rocks and the origin of granite.

1691 Geochim. Cosmochim. Acta 53, 917–922. https://doi.org/10.1016/0016-7037(89)90036-7

1692 Marshall, B.D., DePaolo, D.J., 1982. Precise age determinations and petrogenetic studies using the KCa
1693 method. Geochim. Cosmochim. Acta 46, 2537–2545. https://doi.org/10.1016/0016-7037(82)90376-
1694 3

1695 Matsuhisa, Y., Goldsmith, J.R., Clayton, R.N., 1978. Mechanisms of hydrothermal crystallization of
1696 quartz at 250°C and 15 kbar. Geochim. Cosmochim. Acta 42, 173–182.
1697 https://doi.org/10.1016/0016-7037(78)90130-8

1698 Matthews, A., 1976. Magnetite formation by the reduction of hematite with iron under hydrothermal
1699 conditions. Am. Mineral. 61, 927–932.

1700 McCarthy, A., Müntener, O., 2016. Comb layering monitors decompressing and fractionating hydrous
1701 mafic magmas in subvolcanic plumbing systems (Fisher Lake, Sierra Nevada, USA). J. Geophys.
1702 Res. Solid Earth 121, 8595–8621. https://doi.org/10.1002/2016JB013489

1703 McCoy-West, A.J., Fitton, J.G., Pons, M.L., Inglis, E.C., Williams, H.M., 2018. The Fe and Zn isotope
1704 composition of deep mantle source regions: Insights from Baffin Island picrites. Geochim.
1705 Cosmochim. Acta 238, 542–562. https://doi.org/10.1016/j.gca.2018.07.021

1706 Mills, R.D., Simon, J.I., DePaolo, D.J., 2018. Calcium and neodymium radiogenic isotopes of igneous
1707 rocks: Tracing crustal contributions in felsic magmas related to super-eruptions and continental
1708 rifting. Earth Planet. Sci. Lett. 495, 242–250. https://doi.org/10.1016/j.epsl.2018.05.017

1709 O'Neil, J.R., Taylor, H.P., 1969. Oxygen isotope equilibrium between muscovite and water. J. Geophys.
1710 Res. 74, 6012–6022. https://doi.org/10.1029/JB074i025p06012

1711 O'Neil, J.R., Taylor, H.P., 1967. The oxygen isotope and cation exchange chemistry of feldspars. Am.
1712 Mineral. 52, 1414–1437.

1713 Olsen, M.B., Schiller, M., Krot, A.N., Bizzarro, M., 2013. Magnesium isotope evidence for single stage
1714 formation of CB chondrules by colliding planetesimals. Astrophys. J. 776, L1.
1715 https://doi.org/10.1088/2041-8205/776/1/L1

1716 Peterson, B.T., 2013. Rates and Mechanisms of Magmatic Processes: Isotopic and Geochronological
1717 Evidence. University of California, Berkeley.

1718 Plank, T., Langmuir, C.H., 1998. The chemical composition of subducting sediment and its consequences
1719 for the crust and mantle. Chem. Geol. 145, 325–394. https://doi.org/10.1016/S0009-2541(97)00150-
1720 2

1721 Putirka, K.D., 2005. Mantle potential temperatures at Hawaii, Iceland, and the mid-ocean ridge system, as
1722 inferred from olivine phenocrysts: Evidence for thermally driven mantle plumes. Geochemistry,
1723 Geophys. Geosystems 6, n/a-n/a. https://doi.org/10.1029/2005GC000915

1724 Rappoport, D., Crawford, N.R.M., Furche, F., Burke, K., 2011. Approximate Density Functionals: Which
1725 Should I Choose? Encycl. Inorg. Bioinorg. Chem. https://doi.org/10.1002/9781119951438.eibc0380

1726 Richter, F.M., Davis, A.M., DePaolo, D.J., Watson, E.B., 2003. Isotope fractionation by chemical
1727 diffusion between molten basalt and rhyolite. Geochim. Cosmochim. Acta 67, 3905–3923.
1728 https://doi.org/10.1016/S0016-7037(03)00174-1

1729 Richter, F.M., Liang, Y., Davis, A.M., 1999. Isotope fractionation by diffusion in molten oxides.
1730 Geochim. Cosmochim. Acta 63, 2853–2861. https://doi.org/10.1016/S0016-7037(99)00164-7

1731 Richter, F.M., Watson, E.B., Mendybaev, R., Dauphas, N., Georg, B., Watkins, J., Valley, J., 2009.
1732 Isotopic fractionation of the major elements of molten basalt by chemical and thermal diffusion.
1733 Geochim. Cosmochim. Acta 73, 4250–4263. https://doi.org/10.1016/j.gca.2009.04.011

1734 Rudnick, R.L., Gao, S., 2014. Composition of the Continental Crust, in: Treatise on Geochemistry.
1735 Elsevier Ltd., pp. 1–64. https://doi.org/http://dx.doi.org/10.1016/B0-08-043751-6/03016-4

1736 Rudnick, R.L., McLennan, S.M., Taylor, S.R., 1985. Large ion lithophile elements in rocks from high-
1737 pressure granulite facies terrains. Geochim. Cosmochim. Acta 49, 1645–1655.
1738 https://doi.org/10.1016/0016-7037(85)90268-6

1739 Russell, W.A., Papanastassiou, D.A., Tombrello, T.A., 1978. Ca isotope fractionation on the Earth and
1740 other solar system materials. Geochim. Cosmochim. Acta 42, 1075–1090.
1741 https://doi.org/10.1016/0016-7037(78)90105-9

1742 Ryu, J.S., Jacobson, A.D., Holmden, C., Lundstrom, C., Zhang, Z., 2011. The major ion, d44/40Ca,
1743 d44/42Ca, and d26/24Mg geochemistry of granite weathering at pH=1 and T=25 C: Power-law
1744 processes and the relative reactivity of minerals. Geochim. Cosmochim. Acta 75, 6004–6026.
1745 https://doi.org/10.1016/j.gca.2011.07.025

1746 Salisbury, M.J., Bohrson, W.A., Clynne, M.A., Ramos, F.C., Hoskin, P., 2008. Multiple plagioclase
1747 crystal populations identified by crystal size distribution and in situ chemical data: Implications for
1748 timescales of magma chamber processes associated with the 1915 eruption of Lassen Peak, CA. J.
1749 Petrol. 49, 1755–1780. https://doi.org/10.1093/petrology/egn045

1750 Scheuermann, P.P., Syverson, D.D., Higgins, J.A., Pester, N.J., Seyfried, W.E., 2018. Calcium isotope
1751 systematics at hydrothermal conditions: Mid-ocean ridge vent fluids and experiments in the CaSO4-
1752 NaCl-H2O system. Geochim. Cosmochim. Acta 226, 18–35.
1753 https://doi.org/10.1016/j.gca.2018.01.028

1754 Schiller, M., Paton, C., Bizzarro, M., 2012. Calcium isotope measurement by combined HR-MC-ICPMS
1755 and TIMS. J. Anal. At. Spectrom. 27, 38–49. https://doi.org/10.1039/C1JA10272A

1756 Schmitt, A.D., Chabaux, F., Stille, P., 2003. The calcium riverine and hydrothermal isotopic fluxes and
1757 the oceanic calcium mass balance. Earth Planet. Sci. Lett. 213, 503–518.
1758 https://doi.org/10.1016/S0012-821X(03)00341-8

1759 Shahar, A., Young, E.D., Manning, C.E., 2008. Equilibrium high-temperature Fe isotope fractionation
1760 between fayalite and magnetite: An experimental calibration. Earth Planet. Sci. Lett. 268, 330–338.
1761 https://doi.org/10.1016/j.epsl.2008.01.026

1762 Shea, T., Hammer, J.E., 2013. Kinetics of cooling- and decompression-induced crystallization in hydrous
1763 mafic-intermediate magmas. J. Volcanol. Geotherm. Res. 260, 127–145.
1764 https://doi.org/10.1016/j.jvolgeores.2013.04.018

1765 Simon, J.I., 2019. Potential of MC-ICP-CC-MS in cosmochemistry and geochronology J, in: Goldschmidt
1766 2019.

1767 Simon, J.I., 2017. Utilizing Stable Isotopes and Isotopic Anomalies to Study Early Solar System
1768 Formation Processes, in: Accretion: Building New Worlds Conference 2017. Houston, p. 2pp.
1769 https://doi.org/10.12681/er.9602

1770 Simon, J.I., DePaolo, D.J., 2010. Stable calcium isotopic composition of meteorites and rocky planets.
1771 Earth Planet. Sci. Lett. 289, 457–466. https://doi.org/10.1016/j.epsl.2009.11.035

1772 Simon, J.I., DePaolo, D.J., Moynier, F., 2009. Calcium Isotope Composition of Meteorites, Earth, and
1773 Mars. Astrophys. J. 702, 707–715. https://doi.org/10.1088/0004-637X/702/1/707

1774 Simon, J.I., Jordan, M.K., Tappa, M.J., Schauble, E.A., Kohl, I.E., Young, E.D., 2017. Calcium and
1775 titanium isotope fractionation in refractory inclusions : Tracers of condensation and inheritance in
1776 the early solar protoplanetary disk. Earth Planet. Sci. Lett. 472, 277–288.
1777 https://doi.org/10.1016/j.epsl.2017.05.002

Skulan, J., DePaolo, D.J., Owens, T.L., 1997. Biological control of calcium isotopic abundances in the global calcium cycle. Geochim. Cosmochim. Acta 61, 2505–2510. https://doi.org/10.1016/S0016-7037(97)00047-1

Song, Y., Li, Y., Wang, W., Wu, Z., 2019. First-principles investigation of the concentration effect on equilibrium fractionation of Ca isotopes in forsterite. Acta Geochim. https://doi.org/10.1007/s11631-019-00346-w

Staudigel, H., 2003. Hydrothermal alteration processes in the oceanic crust. Treatise on geochemistry 511–535.

Stepanov, A.S., Hermann, J., Korsakov, A. V., Rubatto, D., 2014. Geochemistry of ultrahigh-pressure anatexis: Fractionation of elements in the Kokchetav gneisses during melting at diamond-facies conditions. Contrib. to Mineral. Petrol. 167, 1–25. https://doi.org/10.1007/s00410-014-1002-x

Syverson, D.D., Scheuermann, P., Higgins, J.A., Pester, N.J., Seyfried, W.E., 2018. Experimental partitioning of Ca isotopes and Sr into anhydrite: Consequences for the cycling of Ca and Sr in subseafloor mid-ocean ridge hydrothermal systems. Geochim. Cosmochim. Acta. https://doi.org/10.1016/j.gca.2018.03.018

Turchyn, A. V., Alt, J.C., Brown, S.T., DePaolo, D.J., Coggon, R.M., Chi, G., Bédard, J.H., Skulski, T., 2013. Reconstructing the oxygen isotope composition of late Cambrian and Cretaceous hydrothermal vent fluid. Geochim. Cosmochim. Acta 123, 440–458. https://doi.org/10.1016/j.gca.2013.08.015

Turchyn, A. V., DePaolo, D.J., 2019. Seawater Chemistry Through Phanerozoic Time. Annu. Rev. Earth Planet. Sci. 47, 197–224. https://doi.org/10.1146/annurev-earth-082517-010305

Urey, H.C., 1947. The thermodynamic properties of isotopic substances. J. Chem. Soc. 562. https://doi.org/10.1039/jr9470000562

Valdes, M.C., Debaille, V., Berger, J., Armytage, R.M.G., 2019. The effects of high-temperature fractional crystallization on calcium isotopic composition. Chem. Geol. #pagerange#. https://doi.org/10.1016/J.CHEMGEO.2019.01.012

Valdes, M.C., Moreira, M., Foriel, J., Moynier, F., 2014. The nature of Earth's building blocks as revealed by calcium isotopes. Earth Planet. Sci. Lett. 394, 135–145. https://doi.org/10.1016/j.epsl.2014.02.052

Vielzeuf, D., Baronnet, A., Perchuk, A.L., Laporte, D., Baker, M.B., 2007. Calcium diffusivity in alumino-silicate garnets: An experimental and ATEM study. Contrib. to Mineral. Petrol. 154, 153–170. https://doi.org/10.1007/s00410-007-0184-x

von Damm, K.L., 2000. Chemistry of hydrothermal vent fluids from 9{\textdegree}{\textendash}10{\textdegree}N, East Pacific Rise: {\textquotedblleft}Time zero,{\textquotedblright} the immediate posteruptive period. J. Geophys. Res. Solid Earth 105, 11203–11222.

Wang, W., Qin, T., Zhou, C., Huang, S., Wu, Z., Huang, F., 2017a. Concentration effect on equilibrium fractionation of Mg-Ca isotopes in carbonate minerals: Insights from first-principles calculations. Geochim. Cosmochim. Acta 208, 185–197. https://doi.org/10.1016/j.gca.2017.03.023

Wang, W., Zhou, C., Qin, T., Kang, J.T., Huang, S., Wu, Z., Huang, F., 2017b. Effect of Ca content on equilibrium Ca isotope fractionation between orthopyroxene and clinopyroxene. Geochim. Cosmochim. Acta 219, 44–56. https://doi.org/10.1016/j.gca.2017.09.022

Wang, Y., He, Y., Wu, H., Zhu, C., Huang, S., Huang, J., 2019. Calcium isotope fractionation during crustal melting and magma differentiation: Granitoid and mineral-pair perspectives. Geochim.

Cosmochim. Acta 259, 37–52. https://doi.org/10.1016/j.gca.2019.05.030

Watkins, J.M., DePaolo, D.J., Huber, C., Ryerson, F.J., 2009. Liquid composition-dependence of calcium isotope fractionation during diffusion in molten silicates. Geochim. Cosmochim. Acta 73, 7341–7359. https://doi.org/10.1016/j.gca.2009.09.004

Watkins, J.M., DePaolo, D.J., Ryerson, F.J., Peterson, B.T., 2011. Influence of liquid structure on diffusive isotope separation in molten silicates and aqueous solutions. Geochim. Cosmochim. Acta 75, 3103–3118. https://doi.org/10.1016/j.gca.2011.03.002

Watkins, J.M., DePaolo, D.J., Watson, E.B., 2017. Kinetic Fractionation of Non-Traditional Stable Isotopes by Diffusion and Crystal Growth Reactions. Rev. Mineral. Geochemistry 82, 85–125. https://doi.org/10.2138/rmg.2017.82.4

Watkins, J.M., Liang, Y., Richter, F., Ryerson, F.J., DePaolo, D.J., 2014. Diffusion of multi-isotopic chemical species in molten silicates. Geochim. Cosmochim. Acta 139, 313–326. https://doi.org/10.1016/j.gca.2014.04.039

Watson, E.B., Müller, T., 2009. Non-equilibrium isotopic and elemental fractionation during diffusion-controlled crystal growth under static and dynamic conditions. Chem. Geol. 267, 111–124. https://doi.org/10.1016/j.chemgeo.2008.10.036

Widanagamage, I.H., Schauble, E.A., Scher, H.D., Griffith, E.M., 2014. Stable strontium isotope fractionation in synthetic barite. Geochim. Cosmochim. Acta 147, 58–75. https://doi.org/10.1016/j.gca.2014.10.004

Wiegand, B. a, Brehme, M., Kamah, Y., Sauter, M., 2015. Distribution of Sr and Ca Isotopes in Fluids of Lahendong Geothermal Field, in: World Geothermal Congress 2015. pp. 1–6.

Wombacher, F., Eisenhauer, A., Heuser, A., Weyer, S., 2009. Separation of Mg, Ca and Fe from geological reference materials for stable isotope ratio analyses by MC-ICP-MS and double-spike TIMS. J. Anal. At. Spectrom. 24, 627. https://doi.org/10.1039/b820154d

Yakymchuk, C., Brown, M., 2014. Consequences of open-system melting in tectonics. J. Geol. Soc. London. 171, 21–40. https://doi.org/10.1144/jgs2013-039

Yokoyama, T., Misawa, K., Okano, O., Shih, C.Y., Nyquist, L.E., Simon, J.I., Tappa, M.J., Yoneda, S., 2017. Extreme early solar system chemical fractionation recorded by alkali-rich clasts contained in ordinary chondrite breccias. Earth Planet. Sci. Lett. 458, 233–240. https://doi.org/10.1016/j.epsl.2016.10.037

Young, E.D., Galy, A., 2004. The Isotope Geochemistry and Cosmochemistry of Magnesium. Rev. Mineral. Geochemistry 55, 197–230. https://doi.org/10.2138/gsrmg.55.1.197

Young, E.D., Galy, A., Nagahara, H., 2002. Kinetic and equilibrium mass-dependant isotope fractionation laws in nature and their geochemical and cosmochemical significance. Geochim. Cosmochim. Acta 66, 1095–1104. https://doi.org/10.1016/S0016-7037(01)00832-8

Zhang, H., Wang, Y., He, Y., Teng, F.-Z., Jacobsen, S.B., Helz, R.T., Marsh, B.D., Huang, S., 2018. No measurable calcium isotopic fractionation during crystallization of Kilauea Iki lava lake. Geochemistry, Geophys. Geosystems. https://doi.org/10.1029/2018GC007506

Zhao, X., Zhang, Z., Huang, S., Liu, Y., Li, X., Zhang, H., 2017. Coupled extremely light Ca and Fe isotopes in peridotites. Geochim. Cosmochim. Acta 208, 368–380. https://doi.org/10.1016/j.gca.2017.03.024

Zhao, Y., Simon, J.I., 2019. Calcium isotope determination with the Nu Sapphire Dual-Path MC-ICP-MS. Goldschmidt 2019 2019.

Zhu, H., Du, L., Li, X., Zhang, Z., Sun, W., 2020. Calcium isotopic fractionation during plate subduction: Constraints from back-arc basin basalts. Geochim. Cosmochim. Acta 270, 379–393. https://doi.org/10.1016/j.gca.2019.12.004

Zhu, H., Liu, F., Li, X., Wang, G., Zhang, Z., Sun, W., 2018. Calcium Isotopic Compositions of Normal Mid-Ocean Ridge Basalts From the Southern Juan de Fuca Ridge. J. Geophys. Res. Solid Earth 123, 1303–1313. https://doi.org/10.1002/2017JB014699

Zhu, P., Macdougall, D.J., 1998. Calcium isotopes in the marine environment and the oceanic calcium cycle. Geochim. Cosmochim. Acta 62, 1691–1698. https://doi.org/10.1016/S0016-7037(98)00110-0